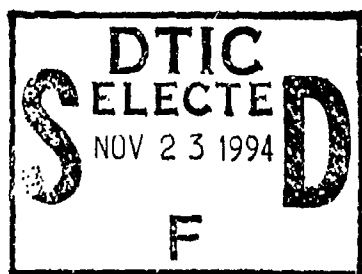AD-A286 446

Resolving Velocity Profiles with the Multi-Scale Profiler

by D.P. Winkel, M.C. Gregg, B.M. Bell, and T. B. Sanford
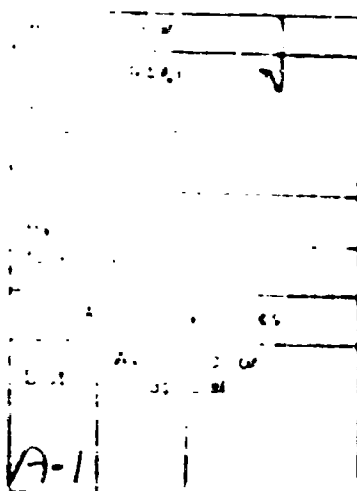
DTIC
S ELECTE D
NOV 2 3 1994
F

Technical Report
APL-UW TR 9414
October 1994

94-35936

Resolving Velocity Profiles with the Multi-Scale Profiler

by D.P. Winkel, M.C. Gregg. B.M. Bell, and T. B. Sanford

Applied Physics Laboratory   University of Washington
1013 NE 40th Street   Seattle Washington 98105-6698

Acknowledgments

ABSTRACT

The Multi-Scale Profiler (MSP), a freely falling dropsonde, has been used over the last 12 years to resolve oceanic shear variance at vertical scales from a few hundred meters down to nearly a centimeter. Because MSP yielded the first complete oceanic shear spectra, it is important to document the methods by which they were produced. Large scales are measured by an electromagnetic current meter (ECM), microscales by airfoil probes, and intermediate scales by an acoustic current meter (ACM). The ACM detects velocity relative to the instrument, so the platform motion must be known to determine the water velocity. Primarily, the ACM measurements are affected by tilt oscillations and by the gross (point-mass) motion of the vehicle; the former is inferred from accelerometer data, and the latter is constructed from a model of the vehicle's response to ocean shear. Horizontal forcing on the array of drag brushes and turning blades at the tail complicates the response by causing MSP to react strongly to fluctuations with scales near the instrument's length of 1.3 m. We examine the effects of this response on spectra of the ACM measurements, noting particularly a deep notch near 0.2 cpm (cycles per meter). To account for such spectral features, the model of Hayes et al. for the TOPS dropsonde was modified so that it correctly parameterized our large tail force. We discuss the dynamics, data processing, and model formulation relevant to production of oceanic velocity profiles from the ACM data, and present analytic transfer functions — derived from Fourier transforms of the model equations — which guide selection of optimal values for the model parameters. Velocity profiles and shear spectra resulting from the motion-corrected ACM data compare well with ECM results at large scales. Owing to MSP's high sampling frequencies, the ACM data provide a direct check on the veracity of the airfoil probe data at scales of 0.1–1 m. The overall strength of our results, as well as the weaknesses and uncertainties, is summarized.

Contents

List of Figures

List of Tables

I.   INTRODUCTION

Observations during the past decade demonstrated the ability of the Multi-Scale Profiler (MSP) to resolve velocity and temperature profiles in the upper 1 km of the ocean. The need for MSP became apparent after analysis of the Fine and Microstructure Experiment (FAME) of 1975, in which different profilers resolved various portions of the vertical wavenumber spectra (Gregg and Sanford, 1980, Gargett et al., 1981). Although much was learned during FAME, measuring viscous dissipation rates, ϵ, with one vehicle, fine-scale shear with another, and diffusive dissipation rates, χ, with yet another proved insufficient for relating shear to turbulence. In response, we began designing MSP in 1980; we first used it in the open ocean in 1983 and have taken it on five subsequent cruises (Table 1). Observations from CSALT, PATCHEX, and Tropic Heat 2 yielded the first fully resolved vertical spectra taken by a single instrument (Gregg et al., 1991, 1993), and profiles in the Florida Strait took the combined measurements close to bottom topography (Winkel et al., 1992). Here we report MSP characteristics and data processing affecting our published results. In addition, because the need for fully resolved spectra will continue past the life of MSP, we document key features of the design.

To measure velocity at scales from 1 km to nearly 10 mm, MSP combines three previously developed techniques: electromagnetic (Sanford et al., 1978), acoustic travel time (Evans et al., 1978; Hayes et al., 1984), and hydrodynamic lift on small airfoils (Osborn, 1974). By sensing voltages induced as sea water flows through the earth's magnetic field, the electromagnetic current meter (ECM) yields velocity profiles largely unaffected by the response of MSP to ocean currents. However, these profiles are not absolute in that they include unknown, depth-independent offsets. Proper treatment of the ECM measurements requires that MSP rotate, and ECM results are reliable only at scales greater than the distance for one such rotation. The Neil Brown acoustic current meter (ACM), owing to its stability and low noise, can resolve scales close to the 0.2-m path length between its transducers. Because the ACM detects motion relative to the vehicle, minimal platform motion is desirable. Unfortunately, the design of MSP makes it highly responsive to fluctuations with scales close to or greater than its 4.3-m length. In converting the relative measurements to ocean velocities, correcting for the vehicle response requires a model. The airfoil or shear probes sense velocity fluctuations relative to MSP. Their data are transformed into shear spectra to estimate viscous dissipation rates. Also, they extend MSP's resolution down to 10 mm; smaller scales are smoothed by the probe tips.

To avoid vehicle dynamics associated with a rapid spin, we use rotation lengths of 15 40 m, much larger than the scales directly generating most turbulence in the thermocline. Given the ECM's limitation, we must rely on the ACM and the associated

Table 1. MSP cruises with nominal fall and rotation rates, Ω_{rot} and W_0, from the main thermocline (below 2-3 MPa). In 1990, the smaller-diameter tail array replaced the larger array, leading to faster fall rates.

Cruise Name	Date	Location	Rotation Rate, Ω_{rot} (Hz)	Fall Rate, W_0 (m s^{-1})
PAC83	May 1983	35°N, 131°W	Tested several configurations	
CSALT	Nov 1985	12°N, 56.5°W	0.011, 0.018	0.27
PATCHEX	Oct 1986	34°N, 127°W 42°N, 126°W	0.017	0.25
Tropic Heat 2	Apr 1987	0°N, 140°W 1, 2, 6, & 11.5°N	0.007 0.002, 0.007	0.27
Florida Straits	Jun 1990	27°N, 79.1 ; 0.9°W	0.013	0.32
COARE 3	Feb 1993	1.7°S, 0, 3°N, 156°E	0.009	0.30

vehicle response model to resolve the scales bridging internal waves and turbulence. Results from the model compare favorably with those from the ECM at scales larger than the rotation length. The smallest scales detected acoustically, 0.1-1 m, require little correction and provide a check on the airfoil signals, which can be contaminated in this band by low-frequency noise and temperature sensitivity. At scales larger than a meter, airfoil data are unreliable owing to increasing vehicle motion and uncertain and varying probe response.

This report focuses on the ACM and our methods for converting its data into ocean velocity profiles. The ACM results are important in that they can resolve shear variance produced by internal waves and turbulence. To interpret the relative ACM measurements, we model the motion of the vehicle as it responds to oceanic shear. The tail array of drag brushes and turning blades causes MSP to respond more severely than other, similar profilers such as TOPS and HRP. Modification of previous response models of Hayes et al. (1984) and Schmitt et al. (1988) to include a proper specification of the large tail force was a major advance in the MSP analysis.

In Section II, we describe the design and operation of MSP, discuss its behavior as a platform, and anticipate effects on the ACM measurements. In Section III we examine the sensors and their data, emphasizing the transformation of ECM and ACM measurements into earth coordinates. In Section IV, after considering vehicle kinematics and dynamics, we present our technique for converting the ACM measurements into ocean velocity profiles—correction for tilt and for attenuation of signals longer than MSP due to its gross motion as a point mass. We explain how we use analytic transfer functions to find optimal values for the model parameters. In Section V, we scrutinize ocean velocity profiles and shear spectra from the ACM and ECM (and airfoil probes) and discuss the strengths and weaknesses of the results. In the final section, we summarize the important aspects of MSP behavior that affect its ability to resolve oceanic shear variance over a wide band of scales. Five appendices supplement this report. Appendix A provides greater detail about the sensors and processing of their data. Appendix B deals with the treatment of airfoil probe data and compares airfoil and ACM spectra. Appendix C discusses the vertical, horizontal, and tilt dynamics of the vehicle. Appendix D details the numerical scheme employed for the response model integration. Appendix E derives the model transfer functions and uses them to demonstrate that tilt dominates the accelerometer data.

II. VEHICLE

A. Vehicle Design and Operations

Much of the design of MSP is aimed at providing a suitable platform for its sensors. As an untethered and freely falling vehicle, it largely avoids high-frequency vibrations and oscillations that could confound measurement of turbulent velocity fluctuations. It descends slowly and steadily for adequate resolution of temperature microstructure, and it spins about its axis for reliable measurement of ambient electric fields.

Most of the length, mass, and volume of MSP comes from its main pressure case, which houses the batteries, microcomputer, memory, electronics, and vehicle-orientation sensors—accelerometers to monitor vehicle tilt and vibration and a magne-tometer to monitor rotational orientation (Figure 1). A gap of a few inches separates the white outer skin from the pressure case. Syntactic foam near the tail fills much of this space, and seawater floods the rest upon deployment. The outer skin streamlines the instrument and forms a nonconducting cylinder between the electrodes of the ECM. To descend while acquiring data and then to ascend for recovery, MSP uses releasable ballast weights, without which its displacement renders it positively buoy-ant (Table 2). Attached to the tail are drag brushes to slow the fall and adjustable turning blades to set the rotation rate.

The leading end (nose) of MSP is home to several sensors and the two ballast tubes (Figure 2). A guard cage protects the sensors. The ACM is the first to sample at a given depth, as its transducers are positioned below the end of the cage to eliminate spurious reflections. Next comes a cluster of fine- and microstructure sensors (Table 3), positioned to sample fluid unperturbed by the ACM or cage. Above the sensors a spherical plastic cap rounds the blunt face of the instrument.

Each deployment begins with the operator recharging the batteries and setting several drop parameters. External cables are disconnected, and MSP is put into the water. Temporary floats (beach balls) hold the instrument at the surface while the ship moves away to avoid contamination of the ECM measurements. After a few minutes MSP releases the beach balls and starts to fall. During descent, data are recorded in 20 Mbytes of solid state memory; this storage is volatile in that data are lost if the batteries lose their charge (typically aft · 5 hours). When the microcomputer determines that either the pressure or time limit has been reached, the ballast is released to end the drop. Corrosible links and fracture pins back up the primary mechanisms, and in shallow waters an acoustic detector aborts the drop before striking the bottom. While ascending, MSP transmits an acoustic telemetry signal containing its slant range and depth (similar to the procedure described by Sanford et al., 1978) so that the ship can approach the rising instrument. At the
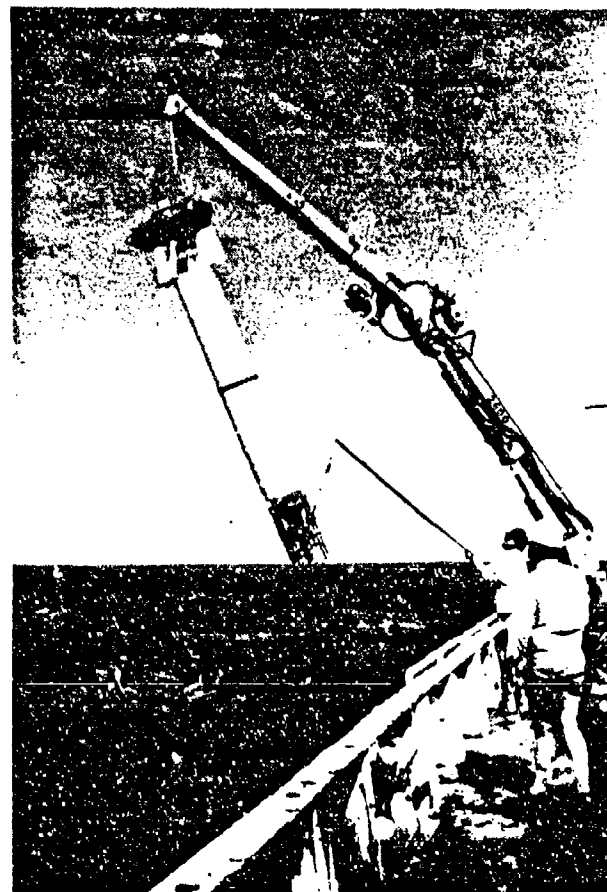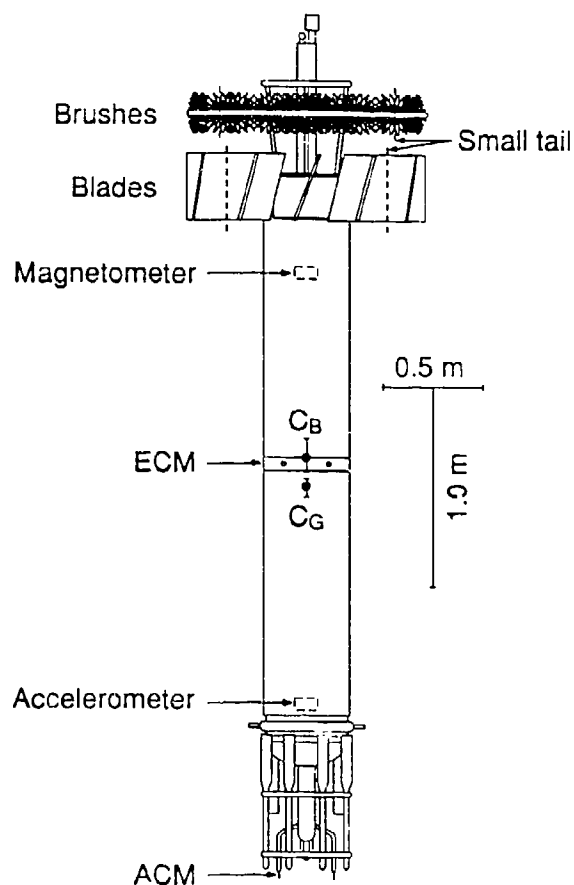
Figure 1. Diagram of Multi-Scale Profiler and photograph of post-drop recovery. Length scale is for the diagram at left. Blades and brushes are drawn for the large-tail configuration; dashed lines indicate width of the small tail. Positions of centers of buoyancy and mass, C_B and C_G, are approximate, owing to uncertainties and to variations in ballast mass and density of trapped water. The pressure sensor, hidden among the turning blades, is attached atop the main pressure case. Photo at right shows recovery after a Florida Straits drop with the small tail.

Table 2. Vehicle parameters. Rightmost column indicates notation used in the main text. Moments are for transverse rotations relative to the ECM (between C_G and C_B). Values in parentheses are for the small-tail array, if different than for the large array.

Total length	4.3	m	
Radius, main tube	0.21	m	(r_N)
Radius, tail array	0.57 (0.42)	m	(r_T)
Pressure tube, length	2.6	m	
Pressure tube, radius	0.16	m	
Vehicle displacement	0.27	m³	(Γ_s)
Vehicle mass, with ballast	280	kg	(M_s)
Ballast mass	10	kg	
Trapped water volume	0.10	m³	
Total mass, including trapped water	382	kg	(M)
Center of mass, from ACM	1.90	m	(C_G)
Center of buoyancy, from ACM	2.05	m	(C_B)
Moment of inertia, effective	830 (730)	kg m²	(I_E)
Damping coefficient, effective	980 (610)	kg m² s⁻¹	(R_E)
Righting moment, effective	580 (550)	N m	(K_E)
Maximum pressure	12.0	MPa	
Effective added mass displacement	0.40	m³	(Γ_e)
Water density, nominal	1025	kg m⁻³	(ρ)

surface, the radio and flashing light at the tail (and the bright orange drag brushes) help visual sighting. A small boat (e.g., Zodiac) is launched to gather MSP and drag it safely to its pickup point beside the ship (Figure 1). Once aboard, the instrument is hooked up to download its data, and preparations are begun for the next drop. Total turnaround time for a 10-MPa (1000-m) drop is around 3 hours.

B.   Vehicle Motion

Table 1 lists nominal fall and rotation rates for the five major MSP cruises. Although faster rotation would enhance ECM performance, the associated dynamics could complicate the ACM and airfoil measurements. Intercruise variations in fall and spin rate generally reflect alterations in the disposable ballast and blade angles. We switched to the small tail configuration in 1990, which weakened lateral forcing to improve the ACM measurements but also reduced vertical drag thereby increasing the fall rate.
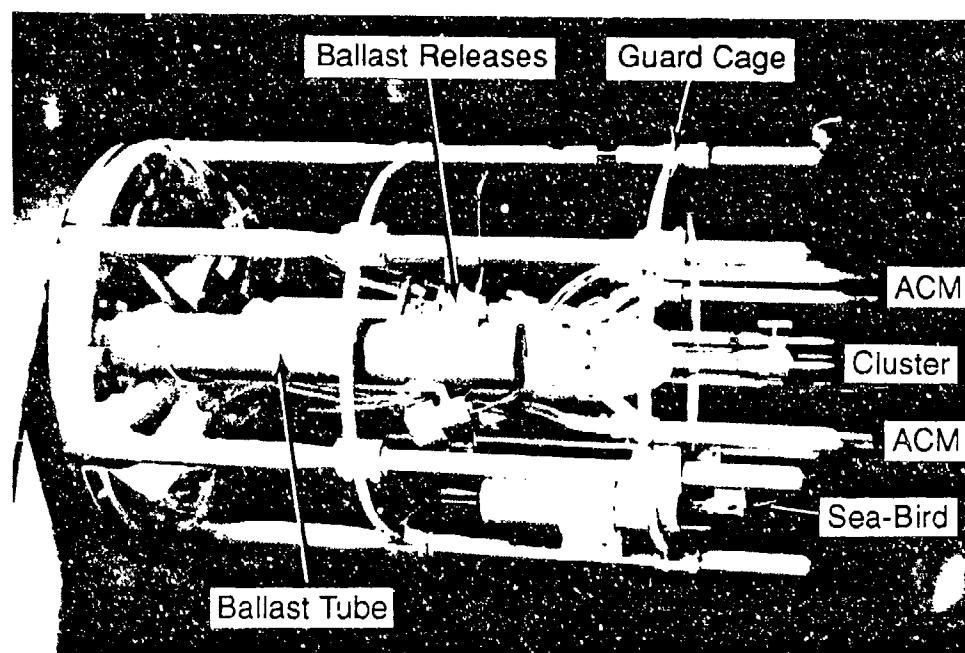
Figure 2. Photograph of MSP nose section with sensors. From top to bottom, sensors in the central cluster are: Neil Brown conductivity, airfoil probe 1, FP07 temperature (finestructure), airfoil probe 2, and FP07 temperature (gradient). For clarity, cables and pump hose are disconnected from the Sea-Bird sensors. Second ballast tube is obscured but is diametrically opposed to the first. Guard rings (center and right) are separated by 0.25 m.

The MSP falls slowly, 0.25–0.35 m s^{-1}, to minimize attenuation by the glass bead thermistor of dissipation-scale temperature fluctuations. We attain a fairly uniform descent by ballasting for around 3.5-kg negative buoyancy, a value that is large compared with variations in buoyancy that occur during a drop as increasing water density competes with shrinking of MSP via cooling and compression. Owing to the broadened axial cross section due to the ring of polyethylene brushes at the tail, the vertical quadratic drag balances the negative buoyancy at acceptably low fall rates. The brushes also homogenize the wake and stifle vibrations that might arise through eddy shedding. Fall rate profiles (Figure 3) show some consistency with the simple buoyancy-drag balance: in the first 10–20 m, MSP accelerates toward a terminal velocity; as its buoyancy increases in the sharpest part of the pycnocline, MSP slows rapidly (with an extreme $dW/dt = -0.001$ m s^{-2} in drop 0211 at 1 MPa):

Table 3. Sensor specifications.

Sensor	Sample Rate (Hz)	Type of Digitization [a]	No. of Axes	Range	Resolution	Noise, rms [b]
Magnetometer	25	12b	3	± 60000 nT	30	10
				degrees, rotation or tilt:[c]	0.05	0.07
Accelerometers	25	16b	2	± 16.4 m s^{-2}	5.0×10^{-4}	2.6×10^{-4}
				degrees tilt:	0.003	0.0015
ECM [d]	25	ftc	2	± 150 m s^{-1}	1.0×10^{-3}	2.0×10^{-3}
ACM	62.5	16b	2	± 0.83 m s^{-1}	2.5×10^{-5}	4.2×10^{-4}
Airfoil Probes [e]	125	16b	2	± 49 s^{-1}	1.5×10^{-3}	(App B)
Pressure	25	ftc		0–21 MPa	3.9×10^{-4}	1.8×10^{-4}
Temp., Sea-Bird	25	ftc		-1–31 °C	1.6×10^{-4}	2.3×10^{-4}
Cond., Sea-Bird	25	ftc		1–6 S m^{-1}	3.2×10^{-5}	2.8×10^{-5}
Temp., FP07	125	16b		0–35 °C	8.0×10^{-4}	4.0×10^{-4}
Cond., Neil Brown	125	16b		3–6.2 S m^{-1}	5.0×10^{-5}	2.5×10^{-5}
Temp. Grad., FP07 [f]	250	16b		± 18 °C m^{-1}	5.4×10^{-4}	—

[a] 12b = 12-bit A/D, ± 10 V input; 16b = 16-bit A/D, ± 8.192 V input; ftc = frequency-time counter, two 16-bit words output (frequency range of input signal depends on sensor: ECM, 5–10 kHz; pressure, 34–40 kHz; Sea-Bird, 6–11 kHz).

[b] Noise in raw data, for a single component (axis), computed by integrating the spectral noise floor out to the Nyquist frequency.

[c] Computed with nominal values of 30,000–50,000 nT for components of the earth's magnetic field.

[d] ECM velocities vary inversely with B_Z, the vertical component of the geomagnetic field; listed values are for $B_Z = 40,000$ nT.

[e] The two axes of the airfoil probes are usually aligned in parallel for redundancy; range and resolution, valid for 1–20 cpm and 0.30 m s^{-1}, increase with higher wavenumber or slower fall rate; dissipation rates, ϵ, computed from airfoil probe spectra have a noise level of $(3-10) \times 10^{-11}$ W kg^{-1}.

[f] Range and resolution, valid for 1–7 cpm, increase with higher wavenumber (some temperature variation, also); dissipation rates, χ, computed from gradient spectra, have a noise level of $(10^{-12} - 10^{-14})$ °C^2 s^{-1}.
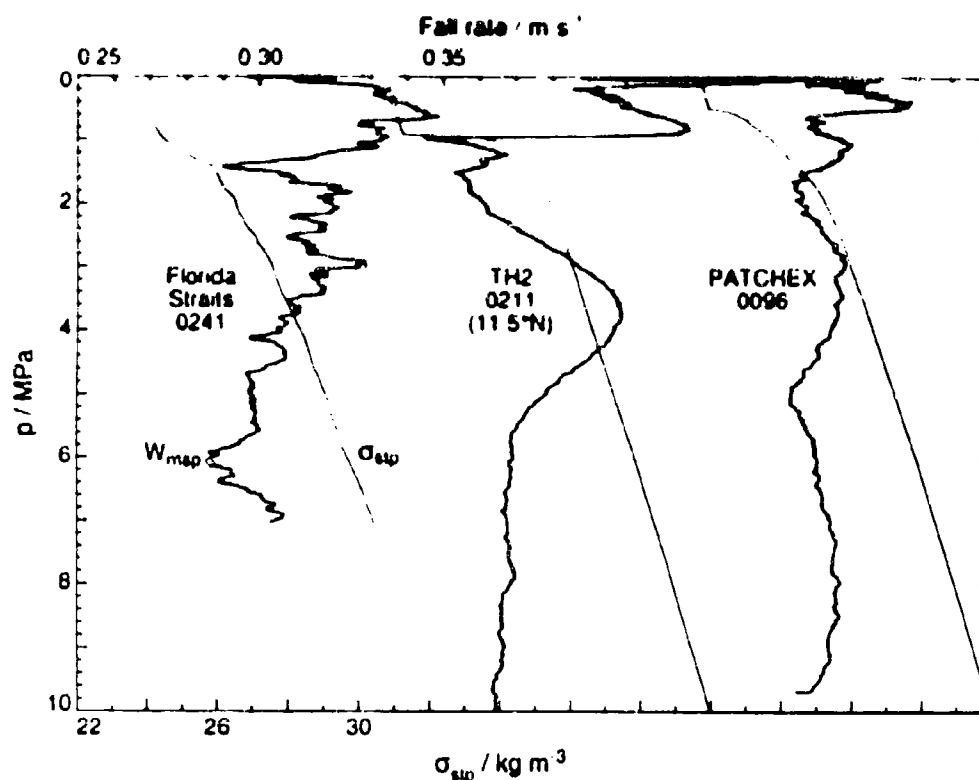
Figure 3. Profiles of fall rates (heavy lines) and *in situ* density (light lines) for drops during three MSP cruises. Subsequent W_{msp} are offset by 0.1 m s^{-1}, σ_{stp} by 8 kg m^{-3}. Below the top of the pycnocline, $W_{msp} = (0.31 \pm 0.02)$ m s^{-1} for 0241, (0.275 ± 0.02) for 0211, and (0.25 ± 0.01) for 0096.

however, the fall rate shows no clear tendency thereafter. Large-scale fluctuations of 0.01–0.03 m s^{-1} are likely due to vertical motions of the water, such as internal waves, carrying MSP along with little effect on the relative flow (Desaubies and Gregg, 1978). Despite uncertainties in net buoyancy and relative flow, we estimate a vertical drag coefficient of 1.0 ± 0.15 based on comparison of fall and rise rates just before and after ballast release.

Currents passing across MSP induce quadratic drag and linear pressure forces which accelerate the vehicle horizontally. Dominating the response are the pressure forces, which occur at the nose and tail, where the vehicle radius widens. The nature of MSP's response to velocity fluctuations depends on their vertical scale. Owing to the nose force and, to a lesser extent, lateral drag on the main tube, MSP fully tracks the large-scale flow, although its inertia causes it to lag behind somewhat. The tail force quickens MSP's response such that it can partially follow fluctuations at

near vehicle scales (thereby complicating interpretation of the ACM measurements). This distinguishes MSP from less responsive profilers such as TOPS (Hayes et al., 1984) and HRP (Schmitt et al., 1988), which have no comparable tail structure.

In its tilt behavior, MSP acts like a forced, damped pendulum. Separation between the centers of buoyancy and mass (including the trapped water; estimated in Table 2) provides most of the righting moment, and drag along the main tube resists oscillations. As MSP falls, further contributions arise from forces at the tail: vertical drag adds to the righting moment, and oscillation-induced pressure forces produce strong damping. The nose and tail forces from the lateral flow generate a forced response, which overwhelms free oscillation. From incidents in which MSP was impulsively forced (by shark hits?), we observe a natural period at 8-11 s being damped out within two oscillations, consistent with the moments estimated in Table 2.

The effect of MSP's horizontal response on the ACM depends on the scale of the fluctuation being measured. To focus on the gross vehicle motion, we disregard rotation and tilt. At depth z (positive-downward), the ACM measures the relative motion

$$v_{acm}(z) = v_{wat}(z) - v_{msp}(z)$$

between the water and vehicle. Casting the time lag of MSP as a distance lag, D, from a velocity fluctuation to the ACM position, we express the vehicle motion in response to a given wavelength, λ, as

$$v_{msp}(z) = \gamma(\lambda) v_{wat}(z - D) ,$$

where γ is the response factor: $\gamma = 1$ for full response at large scales and 0 for no response at small scales (since inertia prevents MSP from reacting to rapid fluctuations). The ACM measurement becomes

$$v_{acm}(z) = v_{wat}(z) - \gamma v_{wat}(z - D) ,$$

which reduces to $v_{acm}(z) = v_{wat}(z) - v_{wat}(z - D)$ for large scales (such as constant shear flows) and to $v_{acm}(z) = v_{wat}(z)$ for small scales. The strong tail force causes MSP to respond ($\gamma > 0$) at scales near its own length and reinforces the nose force to establish a lag of about one instrument length. In contrast, TOPS and HRP respond little ($\gamma \approx 0$) at scales smaller than 10 m and have lags closer to two instrument lengths. Figure 4 illustrates important tendencies in the ACM measurements for various scales of water motion, $v_{wat}(z) \sim \sin(2\pi/\lambda)z$. At $\lambda \gg D$ the measurement approaches $v_{acm} \approx D\, dv_{wat}/dz$, the constant shear limit. The ACM moves against currents of $\lambda = 2D$ and with those of $\lambda = D$, measuring velocities respectively amplified by $(1+\gamma)$ and diminished by $(1-\gamma)$. These effects complicate our measured ACM spectra, yet hardly perturb spectra from the less responsive TOPS and HRP.
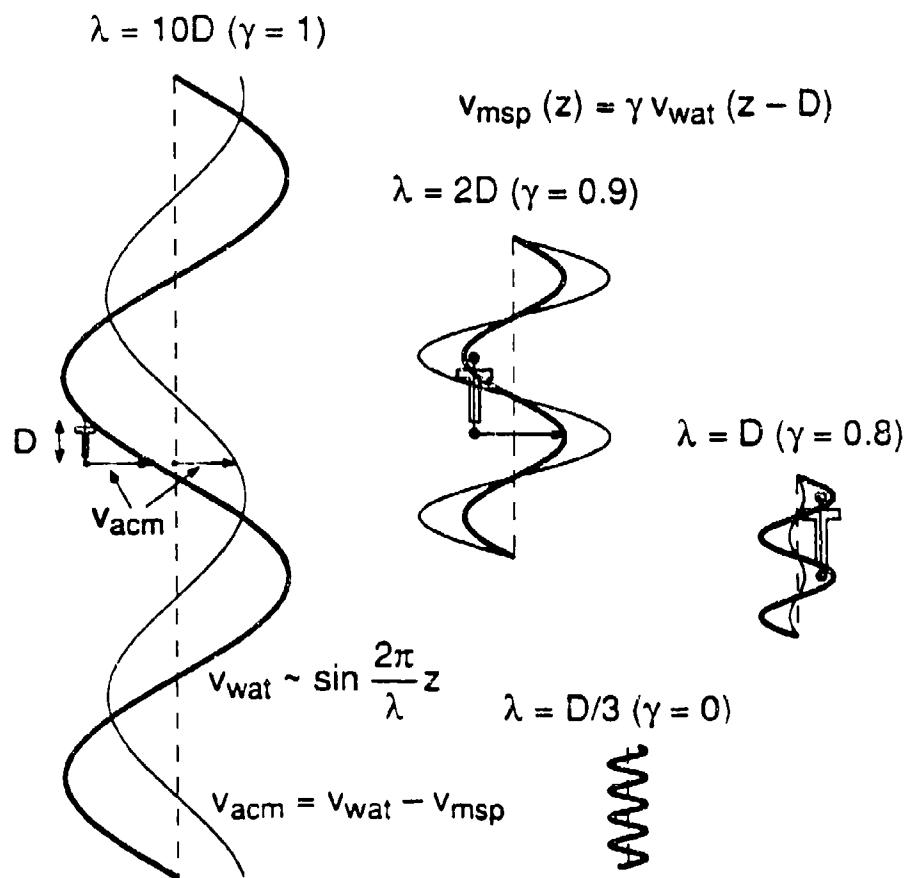
Figure 4. Effects of MSP point-mass response on ACM measurements due to water motions of various wavelengths, λ. Heavy curves are water velocity, $v_{wat} \sim \sin kz$, where $k = 2\pi/\lambda$ and z is depth, positive-downward. Light curves are ACM measured velocity, $v_{acm} = v_{wat} - v_{msp}$. For the vehicle velocity, v_{msp}, the response factor, γ, lessens with scale (see text); for this illustration, the response lag distance of $D \approx 5$ m slightly exceeds MSP's length. At large scales, $v_{acm} \to D\, dv_{wat}/dz$. At $\lambda = 2D$, $v_{acm} = (1+\gamma)v_{wat}$; at $\lambda = D$, $v_{acm} = (1-\gamma)v_{wat}$ (inflated γ's are used here to clearly illustrate responses). When $\gamma = 0$ at small scales, the ACM measures the water directly, $v_{acm} = v_{wat}$. Not considered here are contributions to ACM data by vehicle oscillation.

Also, tilt orientation and oscillation affect ACM measurements in a manner that intensifies our spectral complications.

Before considering further the vehicle dynamics and associated ACM effects, we investigate the array of sensors and the measurements that they obtain.

III. MEASUREMENTS

Table 3 contains specifications for the MSP sensors. Range and resolution depend on the digitization method, as signals are passed to either an A/D converter or a frequency-time counter. Conversion from voltage or frequency to scientific units employs calibrations based on the static response of the sensor and its associated electronics. Noise levels are estimated from spectra of data over quiet regions of the water column; the spectral noise floor is integrated out to the Nyquist frequency (Appendix A). Vertical resolution is limited by noise and also by the dynamic response associated with sensor size or response time. For those devices that measure along multiple directions, Table 3 pertains to a single component; an individual data channel corresponds to each sensitive axis. Axes are defined relative to an orthogonal reference frame, ijk, fixed to MSP. In Appendix A, we discuss the mapping of data from sensor frames onto the common ijk frame and subsequently to the earth's xyz frame.

For each drop, smoothed pressure data are used to build an index file that indicates, for a specified pressure and data channel, the elapsed time at which a measurement was taken. Guided by the index, raw data are low-pass filtered and then subsampled onto evenly spaced pressure grids (Table 4). Reference grid pressures are also used to estimate fall rates and to compute hydrographic quantities.

A. CTD

Two pairs of conductivity-temperature sensors provide redundant measurements and enable intercomparison of performance and response. The Sea-Bird pair has better stability, while the faster response of the other pair, a Neil Brown conductivity cell and a Thermometrics Fastip FP07 thermistor, provides finer vertical resolution. As of 1990, ducting between the Sea-Bird sensors ensures that fluid pumped through the conductivity cell is first sampled by the thermistor. We calibrate the Neil Brown conductivity cell and Thermometrics Fastip FP07 thermistor against the standard of the Sea-Bird pair, using either in $situ$ drop data or measurements in a controlled bath in our laboratory.

Results from the CTD data include profiles of temperature, salinity, density, and buoyancy frequency and vertical wavenumber spectra of temperature and displacement (or strain).

B. Microstructure

Turbulent fluctuations in temperature are sensed by a second FP07 thermistor. Its signals are passed through a differentiating circuit to emphasize the smaller scales and a 60-Hz four-pole Chebyschev filter to suppress high-frequency noise. As we form

Table 4. Data processing specifications for filtering and subsampling. Grid spacing is for standard processing; in seawater, a pressure interval of 10 kPa = 0.01 MPa closely corresponds to a depth interval of 1 m. For the filter, when "BW" is appended, the full length of the low-pass Bartlett window is indicated; for the microstructure data, parentheses enclose the sizes of spectral processing windows and segments (w,s) (see Appendix B).

Sensors	Grid	Filter	Comments
	CTD		
Pressure[a]	0.96 s	1.92-s BW	Interpolated onto 10-kPa grid
Sea-Bird	1 kPa	2-kPa BW	Ducted
	5 kPa	20-kPa BW	Not ducted
Neil Brown and FP07	1 kPa	1-kPa BW	
	Microstructure Spectra		
Temperature (χ)	20 kPa	(24,6) kPa	Robust
	5 kPa	(5,5) kPa	Periodogram
Airfoil probes (ϵ)	20 kPa	(24,6) kPa	Robust
	5 kPa	(5,5) kPa	Periodogram
	Velocity		
ECM[b]	5 kPa	10-kPa BW	
ACM[c]	1 kPa	2-kPa BW	

[a]Smoothed pressure data are subsampled onto a temporal grid, from which elasped drop times are interpolated every 10 kPa to form the pressure reference index.

[b]After being oriented via magnetometer and accelerometer data, drift-filtered ECM measurements are converted to velocity using the geomagnetic field, $\mathbf{B} = B_H \hat{\mathbf{y}} + B_Z \hat{\mathbf{z}}$.

[c]After being oriented via magnetometer data, ACM relative measurements are converted to ocean velocity by using accelerometer data and the point-mass response model to remove platform motion.

power spectra from these data, we account for the static calibration and dynamic response of the probes (Gregg and Meagher, 1980) along with the effects of the electronics. The spectra are used for comparing microstructure with finestructure and to estimate χ.

The pair of airfoil probes detects fluctuations in horizontal velocity (Osborn and Crawford, 1980). For redundancy, we align both probes in the same direction. As

the water pushes on the probe tip, the deflection of an enclosed piezobimorph beam generates a voltage, which is then modified by a differentiator and a 30-Hz four-pole Chebyschev filter. The probe tip smooths out fluctuations of scale smaller than 2 cm (Ninnis, 1984). We divide raw data spectra by the combined transfer function of the probe and electronics to produce microscale shear spectra, which we then integrate to estimate ϵ (Appendix B). By patching ensemble-averaged spectra onto those from the ACM, we broaden the bandwidth to 100 cpm and cross check spectral levels in the overlapping band. Airfoil spectra are unreliable at wavenumbers below 1 cpm, owing to vehicle motion and a poorly understood, probe-dependent response involving temperature sensitivity.

C. Vehicle Orientation

A Develco fluxgate magnetometer monitors the rotational position and motion of the vehicle. The horizontal data allow transformation of ECM, ACM, and accelerometer measurements from the instrument frame to geomagnetic coordinates. The data reflect not only the geomagnetic field, **B**, but also the magnetic signature of the instrument and effects of uncertain sensor alignment, bias, and sensitivity. With the value of **B** at a drop location approximated by a spherical harmonic model, the nongeomagnetic contributions can be estimated and removed from the data (Appendix A).

Sundstrand Q-flex linear servo-accelerometers are aligned along three orthogonal axes, but only the two horizontal components are used. Their primary function is to monitor vehicle tilt, which is the dominant signal (Appendix E). Spectra hit a flat noise floor at 1 to 2 cpm; the lack of spectral spikes above this low-level floor indicates that there are no high-frequency vibrations strong enough to contaminate the airfoil data. Although accelerometer data can augment the magnetometer data for more precise determination of rotational orientation, the effect is inconsequential for small tilt angles. On the other hand, the variation in tilt demonstrates oscillation and wobbling of the platform, motions that significantly affect the ACM.

D. Velocity

The ECM detects voltages induced by ocean currents, a technique nearly insensitive to horizontal motion of the vehicle. Unfortunately, thermal gradients between the electrodes lead to large drifting offsets in the data. We isolate the oceanic signal by using a low-frequency spline to estimate the drift. However, the results are suspect (especially for subrotation scales) because the drift is often comparable to the signal amplitude over a rotation (Figure 5). With our two pairs of electrodes, we could generate velocities independently from each pair as done by Sanford et al. (1978), and then compare or average the results; vertical resolution is on the order of the rotation scale (K_{rot}^{-1}, where $K_{rot} = \Omega_{rot}/W$ is the rotation wavenumber in cycles per meter).
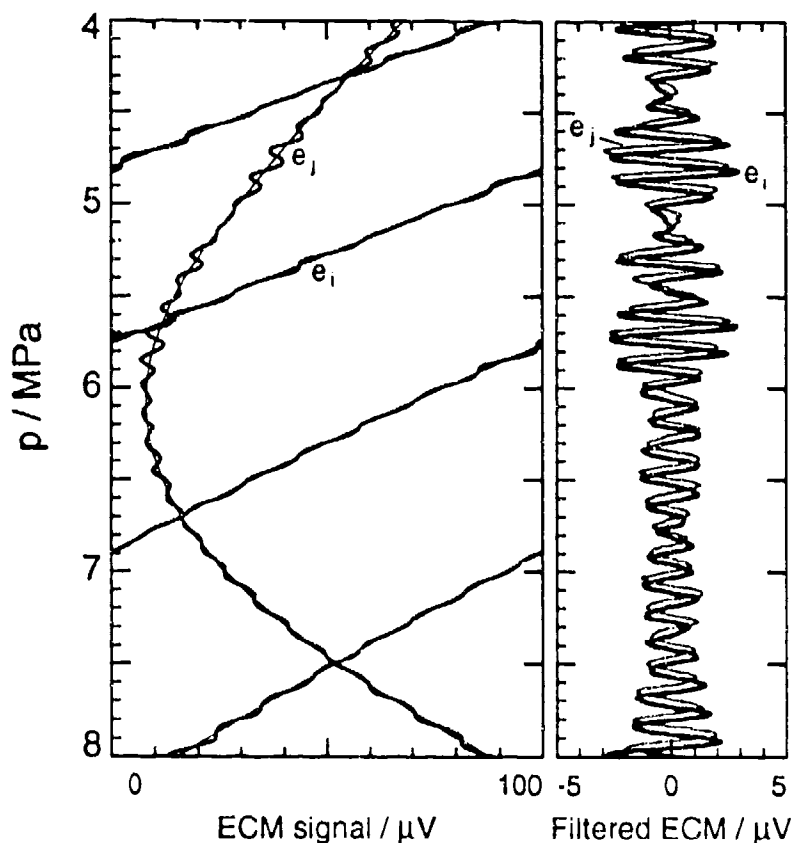
Figure 5. Data from i and j ECM axes. In the left panel, ECM measurements are offset (measured c_i and c_j are, respectively, 1100 and 180 μV at 6 MPa) and wrapped around (for the high-drifting i-axis). Differences between measurements (heavy) and estimated offsets (light) are the oceanic signals, which are shown in the right panel (c_i is heavy; c_j is light).

Instead, we compute the velocity at each grid point by interpreting the filtered data as orthogonal components of the electric field vector (Appendix A). This method potentially yields finer resolution, but the useful limit remains near the rotation scale owing to uncertainty in the removed drift. Since ECM sensitivity is proportional to B_Z, the vertical component of **B**, performance degrades near the magnetic equator with diminishing signal-to-noise ratio. In spite of their restrictions, ECM results are critical in gauging the low-wavenumber performance of the vehicle response model.

The Neil Brown Instrument Systems ACM measures the relative flow along the 0.2-m path between transducers. Two transducer pairs define orthogonal horizontal

axes. Their low noise level (Table 3) allows the ACM to resolve motions down to vertical scales less than a meter. Because of MSP's motion, the ACM detects a velocity different than that of the water (as reflected in Figure 4). As such, our ability to generate ocean velocities—particularly at scales greater than a few meters—is constrained by the success of the vehicle response model. At high wavenumbers, measurements are attenuated for motions whose horizontal scales approach the 0.2-m path length. Also, small-scale data are intermittently contaminated by narrow-banded oscillations of drifting frequency, which appear as a wandering spike in ACM spectra (Appendix A).

For both ECM and ACM processing, measurements must be transformed into geomagnetic coordinates. In preparation, velocity and navigation data must be corrected for bias and axis alignment (Appendix A). Once transformed, ECM data can be directly converted into ocean velocity profiles, but ACM data cannot since they remain affected by platform motion and tilt.

In Figure 6, we compare ECM and ACM profiles at this stage of processing for a portion of PATCHEX drop 0096. We will follow the development of this ACM record into an ocean velocity profile. Table 5 presents nomenclature relevant to these processed data and to subsequent processing in the vehicle response model. The oceanic velocity estimated from the ECM is denoted v_{em}, while that resulting from application of the response model to the ACM measurements, v_{acm}, is denoted v_{wat}.

For the profiles in Figure 6, maximum relative flows at the ACM and vehicle tilts are about 0.03 m s^{-1} and 0.3°. In data from other cruises, relative speeds reach over 0.05 m s^{-1} at sharp shear features and up to 0.10–0.20 m s^{-1} within zones of high large-scale shear (such as above the Equatorial Undercurrent). Tilt angles seldom exceed 1°, except when influenced by surface waves or strong shear.

Figure 7 displays power spectra of ECM, ACM, and accelerometer measurements from 28 PATCHEX drops (including 0096). These are ensemble averages of total spectra (east and north autospectra combined) from 1-MPa (100-m) segments spanning 4–8 MPa (further details in Appendix A). Gregg and Sanford (1988) report shear levels during PATCHEX comparable to those of the Garrett and Munk (GM76) internal wave model (Garrett and Munk, 1975; see also Gregg and Kunze, 1991). Indeed, the ECM spectrum is close to GM76 at wavenumbers lower than K_{rot}; spectral features near K_{rot} and $2 K_{rot}$ (and the divergence from GM76 at higher wavenumbers) reflect shortcomings of the ECM processing related mainly to the large signal drift. The ACM spectrum fluctuates about the ECM (and GM76) spectrum, displaying features suggested in Figure 4: it has excess variance at 0.1 cpm ($\lambda \approx 2 D$) and a deficit near 0.2 cpm ($\lambda \approx D$) which we refer to as the "0.2-cpm notch." When corrected for the variance removed when data were smoothed with the 2-kPa Bartlett window, the ACM spectrum is well above the noise floor. Past 3.5 cpm, aliasing contaminates
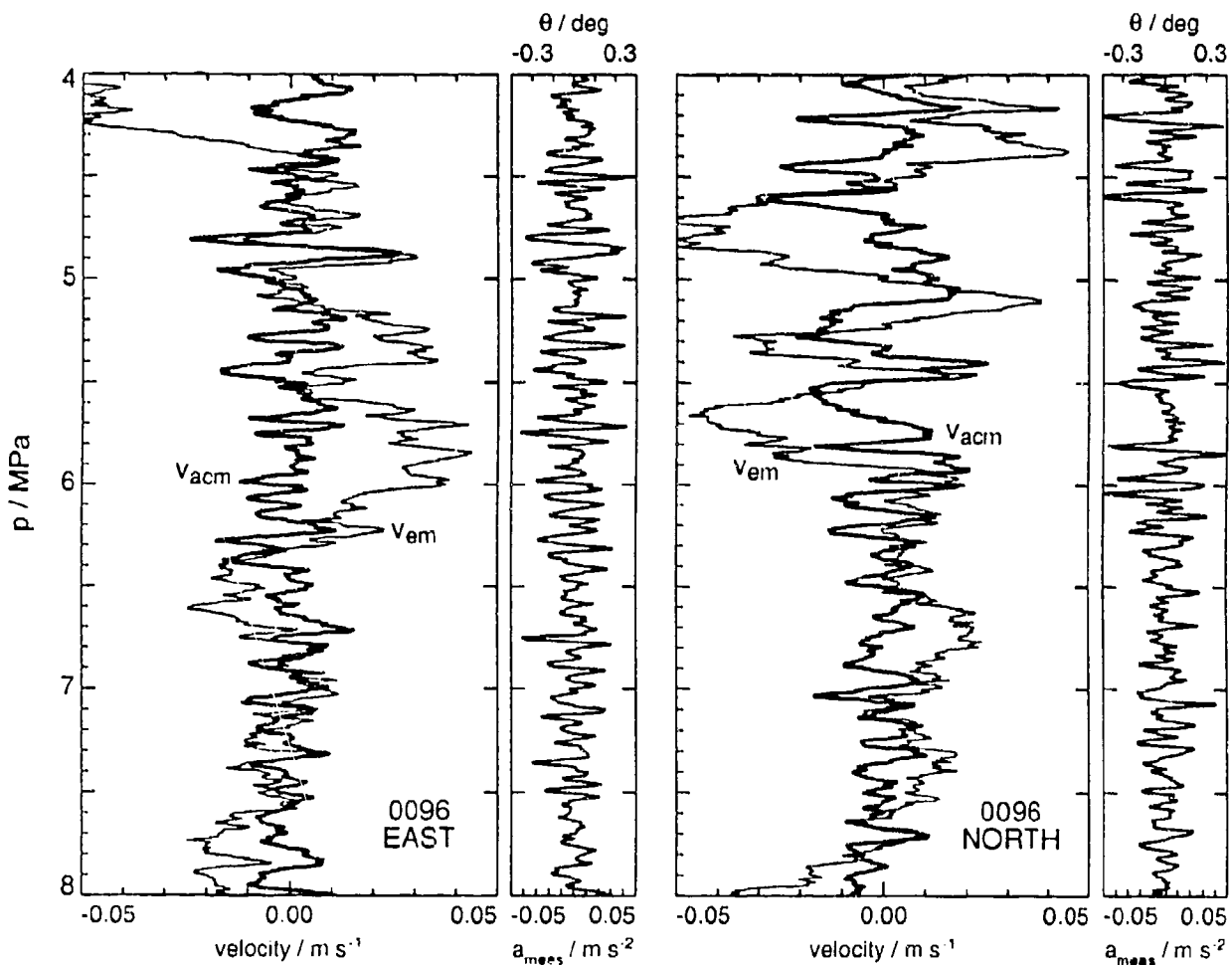
Figure 6. PATCHEX drop 0096, profiles of measurements after transformation to east (left) and north (right) components. ECM velocities (light lines) are demeaned for display; ACM velocities (heavy lines) are not. Tilt angles, θ, are computed from accelerometer data as $\theta = (a_{\text{meas}}/g)$, in radians. Note that 1 MPa = 100 m relates pressure to depth, approximately.

the spectrum (Appendix A). The broad peak of the accelerometer spectrum near 0.12 cpm reflects the forced tilt response as velocity fluctuations push the nose and tail in opposite directions.

To generate an oceanic spectrum from the ACM measurements, we must correct them for tilt and for MSP's gross motion as a point mass. We seek to convert the distorted measurement spectrum into the true oceanic spectrum. We require that the final spectrum be reasonably smooth and that it be close to ECM levels at low wavenumbers. With the PATCHEX dataset as a test case, the GM76 model spectrum

can also provide some guidance. To reduce the dynamic range and emphasize spectral features, subsequent displays are in the form of shear spectra, computed as $\Phi_s(k) = (2\pi k)^2 \Phi_v(k)$, with wavenumber k in cycles per meter.

With ACM and accelerometer measurements in geomagnetic coordinates, we assume that we have accounted for all rotational effects. We have evaluated spin-related dynamics, such as gyroscopic and Magnus effects, and found them negligible relative to those included in our response model. Therefore, we can consider motions and forces in the xz-plane independently of those in the yz-plane.

Table 5. Measured or derived variables in velocity processing. Functions of depth, z, are attributes of the water, independent of MSP. Those describing or involving vehicle motion are defined as functions of t, the elapsed time of the drop when the ACM is at depth $z(t)$. Fourier transforms, e.g., $\hat{v}_{\text{wat}}$, are defined in Appendix E.

Variable		Description	Spectrum	Transfer Function		
$v_{\text{wat}}(z)$	[m s^{-1}]	Water velocity	Φ_v^{wat}		1	
$v_{\text{msp}}(t)$	[m s^{-1}]	Vehicle velocity (as point mass)	Φ_v^{msp}	$A(k)$	$=$	$\hat{v}_{\text{msp}} / \hat{v}_{\text{wat}}$
$W_{\text{msp}}(t)$	[m s^{-1}]	Absolute fall rate				
$\theta(t)$	[radians]	Vehicle tilt	Φ_θ	$B(k)$	$=$	$\hat{\theta} / \hat{v}_{\text{wat}}$
$z(t)$	[m]	Depth at ACM				
$v_{\text{rel}}(t)$	[m s^{-1}]	Relative horiz. vel. (at ACM)	Φ_v^{rel}	$C_r(k)$	$=$	$\hat{v}_{\text{rel}} / \hat{v}_{\text{wat}}$
$v_{\text{acm}}(t)$	[m s^{-1}]	ACM measured velocity	Φ_v^{acm}	$C_m(k)$	$=$	$\hat{v}_{\text{acm}} / \hat{v}_{\text{wat}}$
$a_{\text{meas}}(t)$	[m s^{-2}]	Measured acceleration	Φ_a^{meas}	$D(k)$	$=$	$\hat{a}_{\text{meas}} / \hat{v}_{\text{wat}}$
$V_N(t)$	[m s^{-1}]	Relative velocity at nose				
$V_T(t)$	[m s^{-1}]	Relative velocity at tail				
$v_{\text{em}}(z)$	[m s^{-1}]	ECM water velocity	Φ_v^{em}			
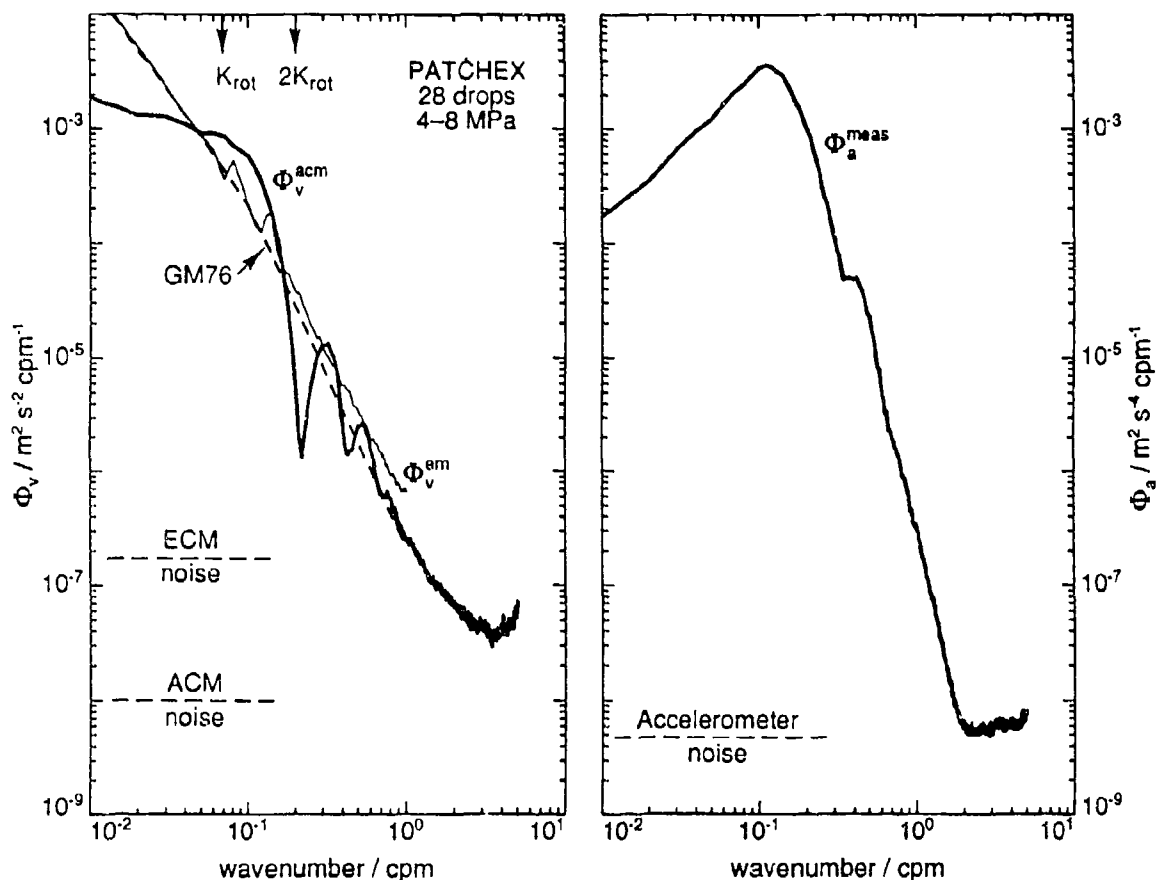
Figure 7. Vertical wavenumber spectra of measured data from 28 PATCHEX drops, 4–8 MPa (wavenumbers assume 0.01 MPa = 1 m). Spectra are for total (east+north) variance; indicated noise levels are also for combined components. Left: ECM velocity spectrum (light line) has spikes near K_{rot} and $2K_{rot}$, and closely follows the GM76 spectrum (dashed line) computed with $N = 0.00343$ s^{-1}; ACM spectrum (heavy line) has a deep notch near 0.2 cpm. Right: accelerometer spectrum peaks near 0.11 cpm. The variance removed by digital low-pass filtering of the data has been recovered in these spectra (see Appendix A).

IV. ACM RESPONSE MODEL

To produce oceanic velocity profiles from the ACM data, we must know how the instrument was moving. Our response model considers the motion as the sum of the vehicle's oscillation about its center of gravity and its gross movement as a point mass (at C_G).

The first step of processing removes tilt from the ACM data, producing the horizontal relative velocity that would have been measured had MSP remained perfectly upright. The contaminating signals include the component of the fall rate detected by the tilted ACM and the velocity of the ACM as tilt oscillations sweep it through the water. Two model parameters are introduced that allow the necessary corrections to be inferred from the accelerometer data.

The second processing step uses the corrected relative velocities to estimate horizontal forces on the vehicle. Integration of the induced accelerations yields MSP's horizontal velocity, which is then added to the relative velocity to form the oceanic velocity. The model utilizes one force near the nose and another near the tail; both vary linearly with the relative velocity. Each force is specified by three parameters: its factor of proportionality, its location, and the size of its smoothing window. The forces are computed at their respective locations but are then applied in combination at the vehicle's center of gravity.

A. Vehicle Kinematics

To consider motion confined to the xz-plane, let $\hat{x}$ and $\hat{z}$ be the horizontal and vertical unit vectors (Figure 8). The ocean velocity is defined as

$$\mathbf{v}_{wat}(z) = v_{wat}(z)\,\hat{x} + W_{wat}(z)\,\hat{z} \tag{1}$$

and is assumed not to vary during an MSP drop. The vehicle's center of gravity, P, has location

$$\mathbf{x}_{msp}(t) = x_p(t)\,\hat{x} + z_p(t)\,\hat{z} \tag{2}$$

and velocity

$$\mathbf{v}_{msp}(t) = \frac{d}{dt}\mathbf{x}_{msp}(t) = v_{msp}(t)\,\hat{x} + W_{msp}(t)\,\hat{z} \tag{3}$$

at time t. The fall rate, $W_{msp} = dz_p(t)/dt$, is positive downward.

When the vehicle's longitudinal axis (centerline) is rotated anticlockwise from vertical, the tilt angle, $\theta(t)$, is positive. An additional component of vehicle motion occurs as the tilt changes. In particular, the velocity of the ACM is

$$\mathbf{v}_{msp}(t) \;+\; L_v\,\frac{d\theta}{dt}\,\hat{n}\;, \tag{4}$$
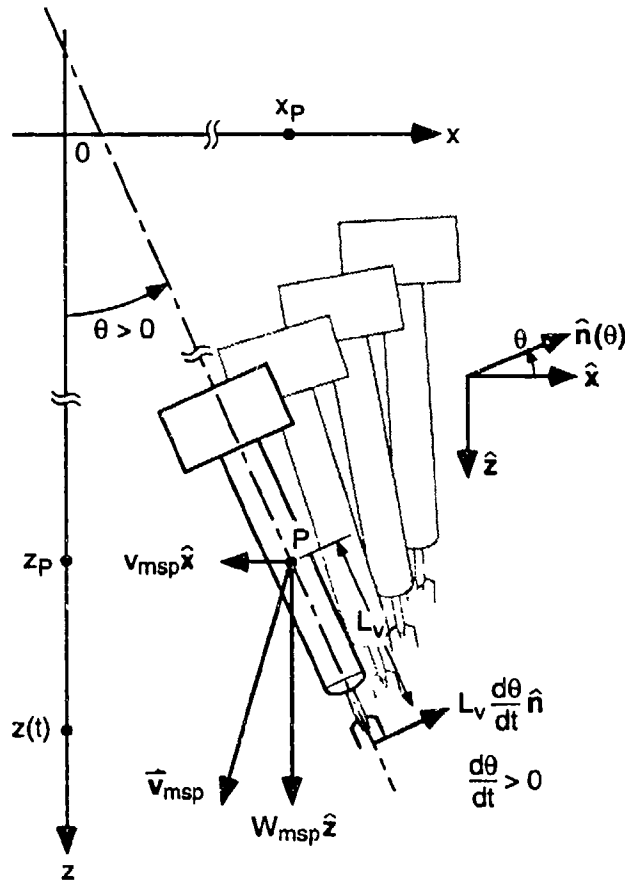
Figure 8. Definition sketch for MSP position and motion at time t, with ACM at depth $z(t)$. Tilt position, $\theta(t)$, and oscillation, $d\theta/dt$, are shown with positive sense. Unit vectors $\hat{\mathbf{x}}$, $\hat{\mathbf{z}}$, and $\hat{\mathbf{n}}(\theta)$ point in the positive horizontal, vertical, and transverse directions. Point-mass reference P, located at $\mathbf{x}_{msp}(t) = x_p(t)\,\hat{\mathbf{x}} + z_p(t)\,\hat{\mathbf{z}}$, moves with velocity $\mathbf{v}_{msp}(t) = v_{msp}(t)\,\hat{\mathbf{x}} + W_{msp}(t)\,\hat{\mathbf{z}}$. At distance $L_v > 0$ down from P, the ACM moves with an additional $L_v\, d\theta/dt\,\hat{\mathbf{n}}$ due to the oscillating tilt.

where L_v is the distance from the ACM to P and

$$\hat{\mathbf{n}}(\theta) = \cos\theta\,\hat{\mathbf{x}} - \sin\theta\,\hat{\mathbf{z}} \tag{5}$$

is the transverse unit vector.

The ACM detects the relative motion, along the direction of $\hat{\mathbf{n}}$, of the water at depth

$$z(t) = z_p(t) + L_v \cos\theta . \tag{6}$$

In addition to the horizontal component of the relative velocity,

$$v_{\text{rel}}(t) = v_{\text{wat}}(z(t)) - v_{\text{msp}}(t) \,, \tag{7}$$

the tilted ACM also senses part of the vertical component,

$$W_{\text{rel}}(t) = W_{\text{wat}}(z(t)) - W_{\text{msp}}(t) \,. \tag{8}$$

Along with the contribution from oscillations, and with the small-angle approximations $\sin \theta = \theta$ and $\cos \theta = 1$, the total ACM measurement is

$$v_{\text{acm}}(t) = \underbrace{v_{\text{rel}}(t)}_{\text{horiz}} - \underbrace{W_{\text{rel}}(t)\,\theta(t)}_{\text{tilt}} - \underbrace{L_v \frac{d}{dt}\theta(t)}_{\text{oscil}} \tag{9}$$

neglecting any flow distortion at the transducers. It is the first term, the relative horizontal flow, that we retain for the response model, and so we need to estimate the tilt and oscillation terms to remove them from the measured ACM data.

We infer vehicle tilt from the accelerometer data. With L_a as the distance from P to the sensor and gravitation acceleration $g = 9.8$ m s^{-2}, the combined signal is

$$a_{\text{meas}}(t) = \underbrace{g\,\theta - \frac{dW_{\text{msp}}}{dt}\theta}_{\text{tilt}} + \underbrace{\frac{dv_{\text{msp}}}{dt}}_{\text{horiz}} - \underbrace{(W_{\text{msp}} + v_{\text{msp}}\,\theta)\frac{d\theta}{dt}}_{\text{frame}} + \underbrace{L_a \frac{d^2\theta}{dt^2}}_{\text{centrip}} \tag{10}$$

assuming small angles. The first term is the vertical acceleration detected by a tilted sensor (note that $g \gg dW_{\text{msp}}/dt$). In Appendix E we show that it dominates the remaining terms in (10): the lateral acceleration of MSP, the acceleration perceived as the sensor's reference frame changes orientation with the oscillating tilt, and the centripetal acceleration of the sensor relative to P.

B. Vehicle Dynamics

The motion of the water past MSP leads to various forces that push the vehicle horizontally and vertically and cause it to tip. These forces are discussed while developing expressions for their balances in Appendix C. Here, to set up the response model, we summarize the horizontal balance.

As illustrated in Figure 9, the nose and tail forces,

$$F_N = \pi r_N^2 \rho V_N \,|W_{\text{rel}}| \quad \text{and} \quad F_T = \pi(r_T^2 - r_N^2)\rho V_T \,|W_{\text{rel}}| \,, \qquad [\text{N}] \tag{11}$$
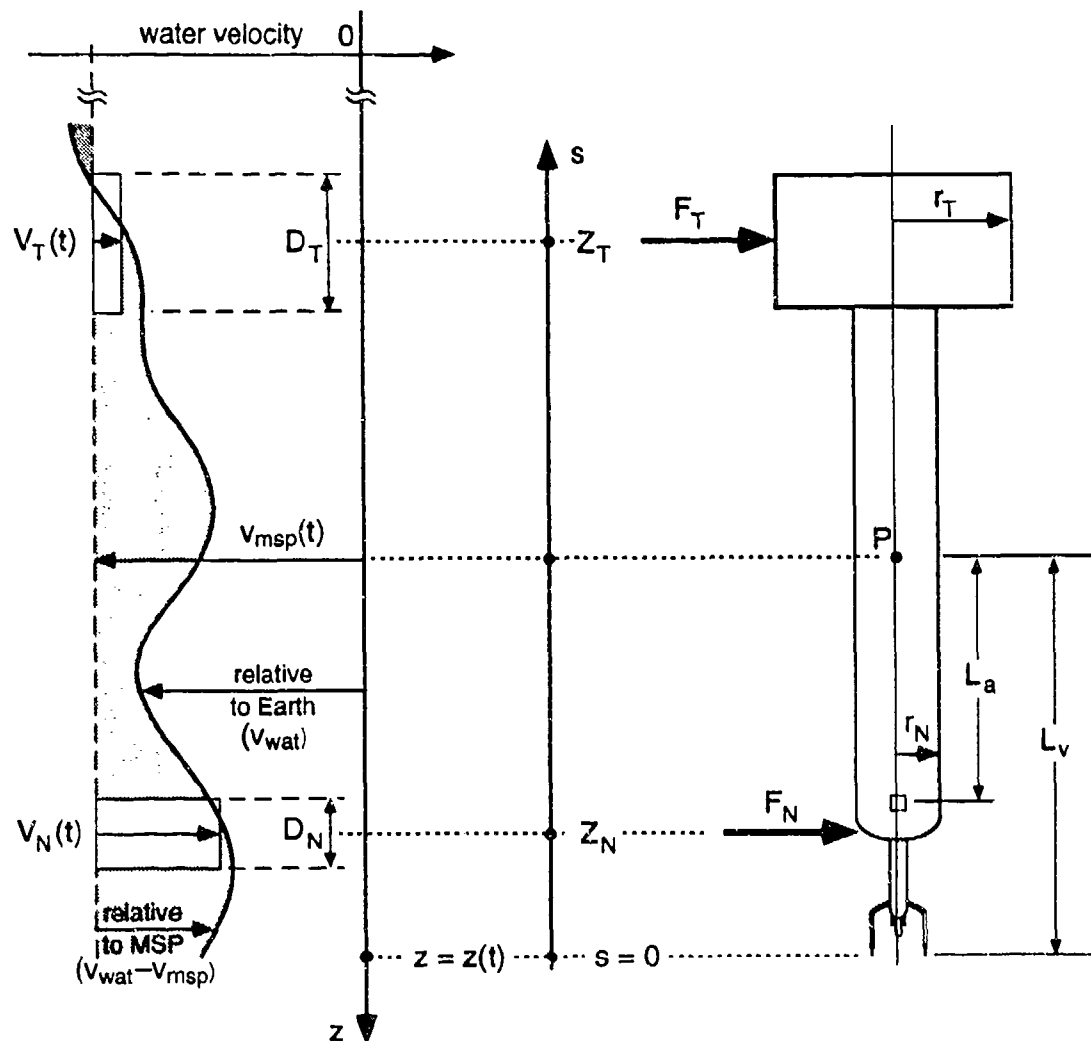
Figure 9. Definition diagram for vehicle dynamics and response model parameters. With MSP constrained to remain upright, the entire vehicle moves with horizontal velocity $v_{msp}(t)$. Origin of the upward-pointing s axis corresponds to reference depth $z = z(t)$ of the ACM. Variations along MSP of horizontal water velocity, $v_{wat}(z-s)$, determine those in relative velocity, $v_{wat}(z-s) - v_{msp}(t)$ (shaded). Defined specifically at the ACM ($s=0$) is the relative velocity $v_{rel}(t)$. Model force F_N or F_T is proportional to relative velocity $V_N(t)$ or $V_T(t)$, the average over a window of size D_N or D_T centered Z_N or Z_T above the ACM. Distances L_v and L_a separate the ACM and accelerometers from the reference P.

push MSP horizontally. The total vehicle mass, M, includes the water trapped within the outer skin, since it moves along with the solid structure. Furthermore, MSP transmits its acceleration to some volume, Γ_e, of the exterior, adjacent water; this retarding action is known as the added mass effect (see Carson and Simpson, 1978). Altogether, the balance of forces yields the horizontal acceleration equation

$$\frac{dv_{\text{msp}}}{dt} = (F_N + F_T)/(M + \rho \Gamma_e). \tag{12}$$

Parameterization and integration of (12) is the crux of the response model.

C. Model Formulation

The primary task of the model is to generate $v_{\text{msp}}(t)$, the instrument's horizontal velocity, which combined with the ACM measurements produces the water velocity. Because the observed tipping and wobbling are of low amplitude, they should not appreciably affect the gross horizontal motion of the vehicle. Therefore, we simplify the dynamics by assuming that MSP remains upright as it responds to the water flowing past. However, tilt and oscillation effects must be removed from the ACM data, $v_{\text{acm}}(t)$, to supply horizontal relative velocities to the model. These corrections come from the accelerometer data, $a_{\text{meas}}(t)$. The two horizontal velocity components (east and north) result from separate and independent runs of the model.

We refer to the position of MSP at time t by the depth $z = z(t)$ of the ACM, with z positive downward. Variables related to the instrument's motion or measurements— those defined as functions of t in Table 5—are henceforth expressed as functions of $z(t)$ or, equivalently, of z. For instance, $v_{\text{msp}}(z) \equiv v_{\text{msp}}(z(t)) \equiv v_{\text{msp}}(t)$ is the horizontal velocity of MSP when the ACM is at depth $z = z(t)$. Note that our data are digitized on 1-kPa pressure grids, nearly equivalent to 0.1-m depth grids.

To compute $v_{\text{rel}}(z)$ from the ACM data, we need to know the relative vertical flow and the vehicle tilt. Given that tilt is dominant in (10) and that $g \gg dW_{\text{msp}}/dt$, we set

$$\theta(z) = a_{\text{meas}}(z)/g \qquad [\text{radians}]. \tag{13}$$

We estimate the fall rate from the pressure record and neglect $W_{\text{wat}}(z)$ to set $W_{\text{rel}}(z) = -W_{\text{msp}}(z)$ from (8). Now, we rearrange (9) and compute

$$v_{\text{rel}}(z) = v_{\text{acm}}(z) - B_f W_{\text{msp}}(z)\, \theta(z) + L_v \frac{d\theta(z)}{dt} \qquad [\text{m s}^{-1}] \tag{14}$$

from the 0.1-m ACM data. Parameter B_f is introduced to allow investigation of the tilt (fall-rate bias) correction. Hayes et al. (1984) and Schmitt et al. (1988) ignore this term and thus implicitly have $B_f = 0$, whereas our development sets $B_f = 1$; we alter B_f between these extremes in tuning and in assessing its effect on the model. Removal of oscillation from the ACM measurements via (14) is vital to the ultimate success

of the vehicle response model. Fortunately, the final model results are insensitive to the 0.1–0.2 m uncertainty in L_v arising from our imprecise knowledge of the location of P.

Supplied with the horizontal relative velocity at the ACM, we need only $v_{\text{msp}}(z)$ to determine $v_{\text{wat}}(z)$ from (7). As shown in Figure 9, we attach the origin of the upward s-axis to $z = z(t)$, so that the relative velocity across MSP at distance s above the ACM is $v_{\text{wat}}(z - s) - v_{\text{msp}}(z)$, which for $s = 0$ is $v_{\text{rel}}(z)$. We define the time and depth of the drop's first measurement as $t = 0$ and $z(t) = z_0$. Our initial conditions are $v_{\text{wat}}(z < z_0) = 0$ and $v_{\text{msp}}(z_0) = 0$. Input $v_{\text{rel}}(z)$ and output records are on grids of $\Delta z = 0.1$ m.

Our neglect of W_{wat} implies $|W_{\text{rel}}(z)| = W_{\text{msp}}(z) = dz/dt$, which allows us to simplify the horizontal acceleration equation, (12), into

$$\frac{dv_{\text{msp}}(z)}{dz} = H_N \, V_N(z) + H_T \, V_T(z) \qquad [\text{s}^{-1}] \qquad (15)$$

with force parameters

$$H_N = \frac{\pi r_N^2}{(M/\rho + \Gamma_e)} \quad \text{and} \quad H_T = \frac{\pi(r_T^2 - r_N^2)}{(M/\rho + \Gamma_e)} \qquad [\text{m}^{-1}] \qquad (16)$$

and smoothed relative velocities

$$V_N(z) = \frac{1}{D_N} \int_{Z_N - 0.5 D_N}^{Z_N + 0.5 D_N} \left(v_{\text{wat}}(z - s) - v_{\text{msp}}(z) \right) ds \qquad [\text{m s}^{-1}]$$

$$\tag{17}$$

$$V_T(z) = \frac{1}{D_T} \int_{Z_T - 0.5 D_T}^{Z_T + 0.5 D_T} \left(v_{\text{wat}}(z - s) - v_{\text{msp}}(z) \right) ds \qquad [\text{m s}^{-1}].$$

Parameters Z_N and Z_T specify the separation between the ACM and the centers of application of F_N and F_T, respectively (Figure 9), and D_N and D_T are the lengths of the corresponding smoothing windows.

In Appendix D, we discuss the numerical method by which we update $v_{\text{msp}}(z)$ via (15) and (17) with previously computed (or initialized) values of $v_{\text{wat}}(z-s)$ and the last vehicle velocity, $v_{\text{msp}}(z - \Delta z)$. Given the relative velocity from the tilt-corrected ACM and the vehicle velocity from the model, we can finally compute the water velocity

$$v_{\text{wat}}(z) = v_{\text{msp}}(z) + v_{\text{rel}}(z). \qquad (18)$$

The initialization $v_{\text{wat}}(z < z_0) = 0$ establishes a depth-independent offset in the oceanic velocity profile, but it can be removed with knowledge of the absolute velocity at some depth (from a nearby mooring, for instance). The initial lack of information

also leads to a startup transient in (17), which vanishes after MSP has descended a few lengths. Also, this portion of a drop generally suffers from surface wave effects and fall-rate spinup.

D.   Parameter Values

As shown in Table 6, we have assigned nominal values to the eight model parameters. The nose and tail parameters Z_N, D_N, Z_T, and D_T are estimated where the vehicle's radius changes (as in Figure 9). We compute H_N and H_T by inserting known or estimated dimensions in (16). We get L_v by placing P near MSP's center of mass and set $B_f = 1$ consistent with our formulation in (9). Running the model with the nominal values leads to unsatisfactory spectral results, however, and so we must determine three values empirically: Z_T to match the 0.2-cpm notch, H_N to attain the low wavenumber shear established by the ECM, and D_T to dampen the vehicle response at high wavenumbers. We can attain further, more subtle improvements to the model results by fine tuning the remaining parameters.

To find optimal parameter values for a given MSP configuration, we could run the model using various sets of values and compare the spectra of the resulting profiles. A quicker and more powerful approach involves analytic transfer functions derived from Fourier transforms of model equations (in Appendix E). Those given in Table 5 are defined for the response of each quantity to the water velocity, v_{wat}. Transfer functions involving only the modeled point-mass response, $A(k)$, are excellent predictors of the corresponding results of the computational model. This is not true if the tilt response, $B(k)$, is involved, since it is derived from the modeled tilt (Appendix C), which differs significantly (especially for $k > 0.4$ cpm) from the observed tilt as inferred from (13).

Recall the two main steps of our model: First, generate v_{rel} by correcting v_{acm} for tilt and oscillation; second, use v_{rel} to simulate v_{msp}, and combine them to produce v_{wat}. Because the first step involves tilt, we must choose values for B_f and L_v by trial and error. The second step is independent of tilt, and so we tune the six potential force parameters using $C_r(k)$, the transfer function for the corrected relative velocity v_{rel}. Specifically, given Φ_s^{rel} from the relative velocity profiles, we compute $C_r(k)$ for a choice of parameter values and generate

$$\Phi_s^{wat} = \Phi_s^{rel}/|C_r(k)|^2$$

for a trial oceanic spectrum. The result closely represents the spectrum of v_{wat} profiles that would be generated from v_{rel} via (15), (17), and (18).

Figure 10 compares v_{acm} for drop 0096 with v_{rel}, as computed from (14) with nominal values of B_f and L_v (Table 6). The tilt and oscillation terms have amplitudes of 1 and 2 mm s^{-1}. Although small, these corrections are significant at scales near the instrument length. Figure 11 shows their effect on the measured PATCHEX

Table 6. Response model parameters. Nominal values are those expected from measured or estimated dimensions. Optimal values, with which the model is run, are determined with help from the transfer functions. Values in parentheses are for the small tail.

Parameter		Description	Nominal Value	Optimal Value Large Tail	Small Tail
Z_N	[m]	Distance to nose force	0.50	0.50	0.50
Z_T	[m]	Distance to tail force	3.40	3.98	4.00
D_N	[m]	Nose window size	0.60	0.80	0.80
D_T	[m]	Tail window size	0.80	1.40	1.60
H_N	[m^{-1}]	Nose force factor	0.18	0.28	0.32
H_T	[m^{-1}]	Tail force factor	1.14 (0.54)	1.16	0.52
L_v	[m]	Distance from ACM to P	1.9	1.8	2.0
B_f		Fall-rate bias factor	1.0	0.9	0.6
β_1	[s^{-1}]	Tilt damping	1.18 (0.84)	0.6	1.0
β_0	[s^{-2}]	Tilt restoring	0.70 (0.75)	1.1	1.4
Q_N	[m^{-1} s^{-1}]	Nose tilt factor	0.07 (0.09)	0.05	0.065
Q_T	[m^{-1} s^{-1}]	Tail tilt factor	0.55 (0.35)	0.95	0.95
L_a	[m]	Distance from accel. to P	1.2		

spectrum, Φ_s^{acm}. In the corrected spectrum, Φ_s^{rel}, the 0.2-cpm notch is broader and half as deep, amplitudes of the other peaks and valleys are diminished, and spectral levels at $k > 0.7$ cpm are lowered. Oscillation accounts for most of the difference, although tilt contributes at $k < 0.2$ cpm. These basic results occur for all MSP datasets.

To complete our transformation from measured to oceanic velocities, we must find values for the six parameters of the point-mass model. In Appendix E, we derive the expression

$$C_r(k) = 1 - \frac{H_N\, e^{-ikZ_N}}{H_N + H_T + ik}\, \text{sinc}\,(kD_N/2) - \frac{H_T\, e^{-ikZ_T}}{H_N + H_T + ik}\, \text{sinc}\,(kD_T/2) \qquad (19)$$

where k is the wavenumber in radians per meter and $\text{sinc}\,x \equiv x^{-1}\sin x$. Starting with the nominal values, we generate oceanic spectra from C_r and Φ_s^{rel} and iteratively tune the parameters until the result satisfies our stated requirements: a smooth spectrum,
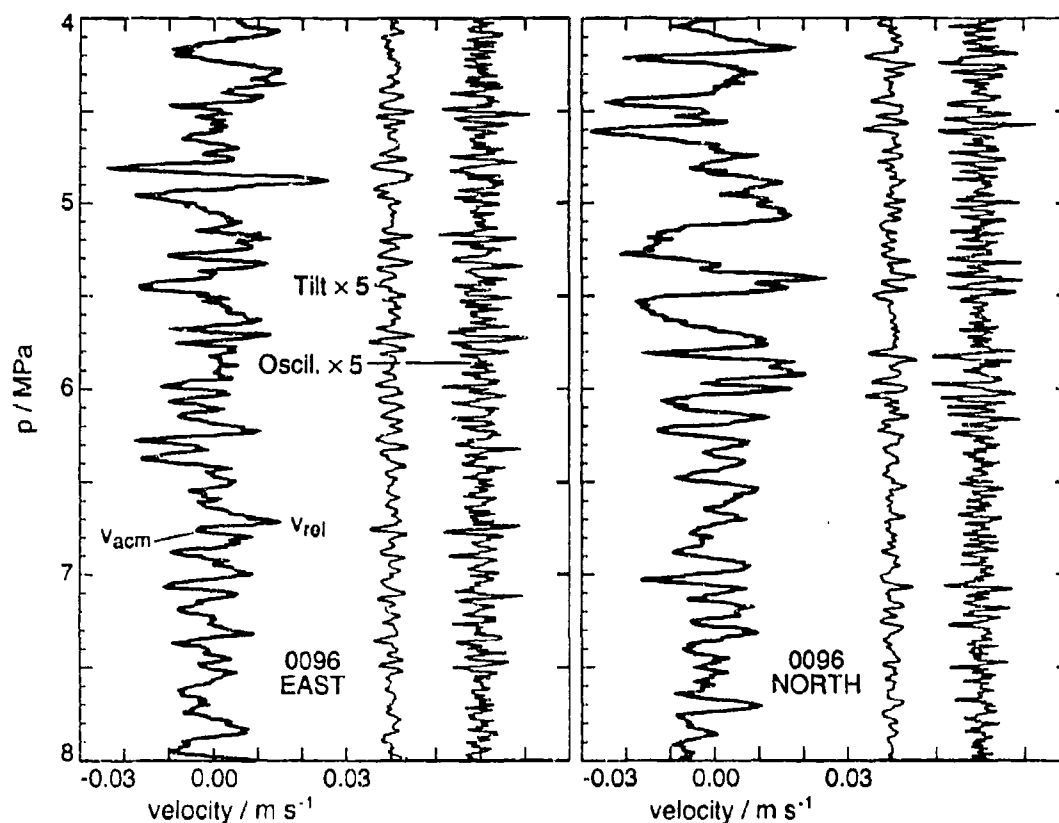
Figure 10. Components of ACM-measured velocity, PATCHEX drop 0096: v_{acm} (light line) is composed of v_{rel} (dark line), tilt $(B_f W_{msp}\theta)$, and oscillation $(-L_v d\theta/dt)$. For display, tilt and oscillation terms were multiplied by 5 and offset by 0.04 and 0.06 m s^{-1}. Aside from a few instances (e.g., near 6.75 MPa for the east components), v_{acm} and v_{rel} are indistinguishable.

devoid of obvious instrumental effects, which is close to ECM levels at low wavenumbers. In Figure 12 we present the optimally tuned versions of C_r for our two tail configurations, and in Table 6 we list the corresponding sets of parameter values. We truncate the display at $k = 1$ cpm, since $C_r(k) \approx 1$ at higher wavenumbers. Unless otherwise noted, the remaining discussion pertains to the configuration used through Tropic Heat 2 (large tail).

Figure 13 compares the C_r computed from (19) when using only the tail force ($H_N = 0$) with that computed when using only the nose force ($H_T = 0$). The dominance of the tail force is obvious, judging by the similarity of C_r to that of the full model. Its position Z_T fixes the wavenumbers of the notch and subsequent
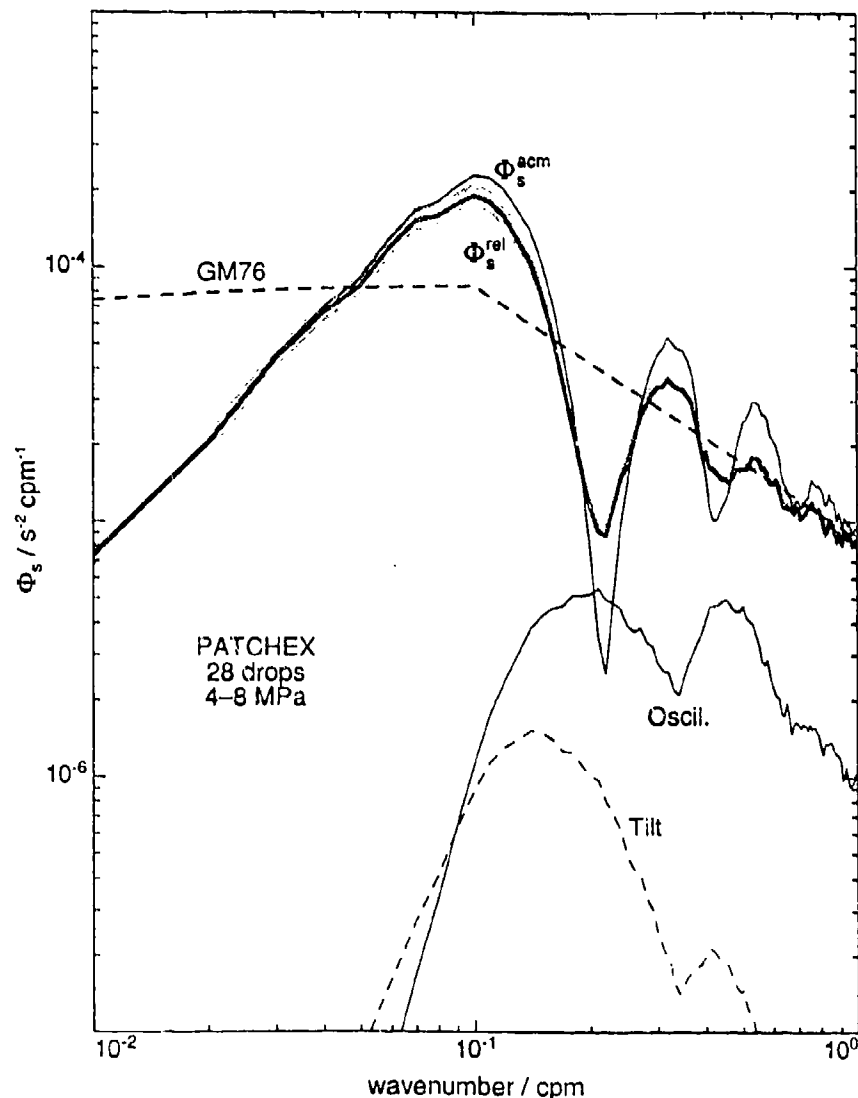
Figure 11. Shear spectra (at intermediate stage) of 28 PATCHEX drops, 4–8 MPa, computed as $\Phi_s = (2\pi k)^2 \Phi_v$. Spectra for measured ACM records are shown by the light line and tilt-corrected spectra by the heavy line (shaded at 95% confidence limits). Also shown are spectra of the tilt and oscillation corrections and of the GM76 model. Spectra are truncated at 1 cpm, beyond which vehicle motion has little effect.
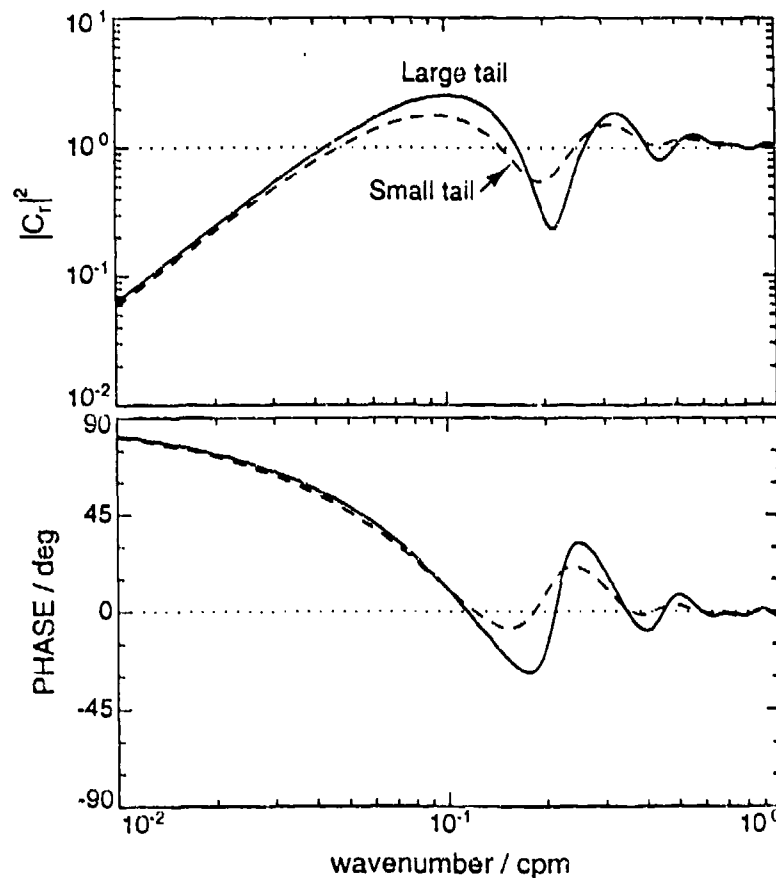
Figure 12. Transfer functions $C_r(k)$ from ocean velocity to relative horizontal velocity at ACM, as computed with the optimal parameter values in Table 6: Upper panel is squared amplitude; lower is phase. Between 0.1 and 0.3 cpm, the response for the large-tail array used up through Tropic Heat 2 (solid line) is more severe than that for the small-tail array used after Tropic Heat 2 (dashed line).

spectral features, and its strength H_T sets their amplitudes. Its window size D_T attenuates high-wavenumber features by reducing the response of the vehicle to water motions of small scale. In regard to the nose force, its strength H_N establishes the low-wavenumber response, its position Z_N plays a minor role, and its window size D_N has almost no effect.

Evaluation of sensitivities of the model to each of the eight parameters is a by-product of tuning. As long as realistic values are assigned to B_f and L_v, the success of the model is insensitive to their exact value. Without the oscillation correction implied by L_v, even the most carefully chosen values of Z_T and H_T yield Φ_s^{wal} that
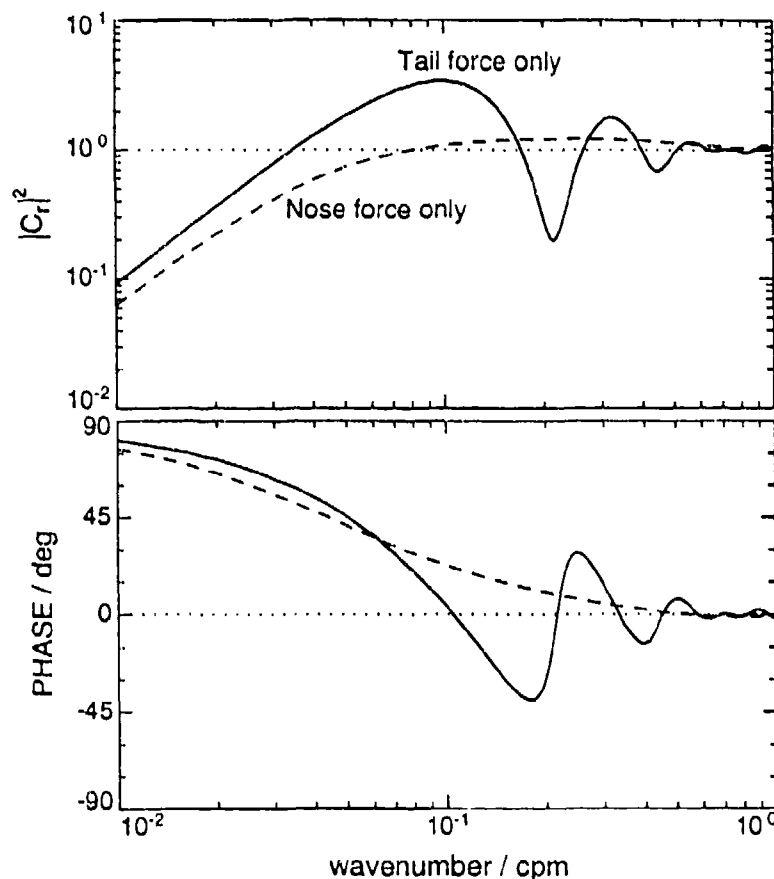
Figure 13. Transfer functions $C_r(k)$ for the large-tail array computed exclusively for the tail force (solid lines) by setting $H_N = 0$ and exclusively for the nose force (dashed lines) by setting $H_T = 0$. With only the tail force, $C_r(k)$ resembles the complete two-force version, aside from the difference in amplitude for $k < 0.1$ cpm. With only the nose force, $C_r(k)$ loses the shape of the complete version, although the amplitudes converge at $k < 0.04$ cpm.

are choppy at $k > 0.2$ cpm. Given the corrected Φ_s^{rel}, we can focus upon the six parameters in (19). The point-mass model is most sensitive to Z_T, coupled with H_T, since these parameters must account for the remaining 0.2-cpm notch. Because the notch is deep and narrow, its position must be closely matched by C_r for the resulting Φ_s^{wat} to be acceptably smooth. The nominal $Z_T = 3.5$ m fails the test, as do values more than 0.05 m away from the optimal value of 3.98 m (which places F_T up in the wake of the brushes). Sensitivity to the other parameters is more subtle, since variations in their values affect broad spectral levels rather than shapes. Two of them, D_T and H_N, differ noticeably from the nominal predictions. The enlarged tail

window is needed to squash the response beyond 0.4 cpm; the stronger nose force is needed to bring Φ_s^{wat} up toward the level of the ECM at low wavenumbers. Finally, the position of F_N slightly affects the notch depth.

Minor variations in the optimal values of the parameters, other than Z_T, do not significantly alter C_r (or C_m). In Appendix E, we fine tune L_v and B_f using the transfer function $H_m(k)$ from v_{acm} to a_{meas}. We compensate for any resulting effect on Φ_s^{rel} by tweaking H_T or Z_N.

We summarize the action of MSP as it filters the water motion, comparing its point-mass response and its tilt response. The large-scale motions carry the vehicle as a point mass, with the nose force dominating for $k < 0.04$ cpm. From 0.05 to 0.15 cpm, the primary effect comes from the tail force and its separation from the ACM. Tilt and oscillation start to contribute at $k > 0.1$ cpm; between 0.2 and 0.4 cpm, the effect of oscillation reinforces, and nearly equals, that of the tail force. Since the point-mass response is weak for $k > 0.4$ cpm, the oscillating tilt of the ACM dictates the difference between v_{acm} and v_{wat} at the smallest scales.

After Tropic Heat 2, we designed the smaller tail to lower H_T via (16). As predicted by (19) and reflected in Figure 12, the weaker tail force led to a broader and shallower notch in Φ_s^{rel}. Relative to that for the large tail, C_r for the small-tail configuration is less sensitive to variations in the tail parameters.

V. RESULTS

### A. Velocity Profiles and Shear Spectra

Ocean velocity profiles from the ACM response model nicely track the ECM results, aside from some large-scale divergence. Figure 14 demonstrates the model's success for PATCHEX drop 0096 and also for a Florida Straits drop containing considerable mean shear and strong fine-scale shear. As anticipated, the agreement between profiles degrades at scales smaller than the rotation length.

Spectral results are a critical test of the model's performance. After running the 28 PATCHEX drops through the model, we form the shear spectrum of the v_{wat} profiles for comparison with the ECM spectrum (Figure 15). At low wavenumbers, up to 0.04 cpm, the spectra are similar in level (both being close to GM76) and are highly coherent with near-zero phase. Around K_{rot} and $2K_{rot}$, coherence is minimal and spikes in Φ_s^{cm} reach twice the ACM levels. At higher wavenumbers, the spectra remain fairly coherent and close in phase despite the higher ECM levels attributed to rotation-related contamination. Coherence is lost at $k > 0.5$ cpm as noise dominates the ECM. The ACM spectrum is reasonably smooth between 0.1 and 1 cpm, aside from minor irregularities at 0.4–0.5 cpm. To emphasize the importance of the tilt effects, we include the spectrum of profiles created without correcting for tilt and oscillation, that is, by running the model with $B_f = L_v = 0$ and with Z_T and H_T chosen so that the tail force alone compensates for the deep notch in Φ_s^{acm}. Now, the spectrum is excessively choppy and uneven in the high-wavenumber band, with the coherence and phase relation to the ECM breaking down around 0.2 cpm.

Many features of the PATCHEX results also appear in the more energetic Florida Straits data, taken with the small-tail configuration. The ACM and ECM spectra are coherent with comparable levels at low wavenumbers; their coherence fades near K_{rot} and $2K_{rot}$, rises at higher wavenumbers, and vanishes as noise overtakes the ECM past 0.4 cpm (Figure 16). Unlike for the large tail, oscillation correction has little effect on coherence near 0.2 cpm, although it remains a vital step toward generating a smooth ACM spectrum.

We check for consistency in the ACM and airfoil levels in the band between 1 cpm, where airfoil spectra become reliable, and 2 to 20 cpm, where raw ACM data reach their noise floor. For the most direct comparison, we utilize data from the ACM axis that is more closely aligned with the airfoil probes. The spectra generally agree to within a factor of 1.5, although there is a tendency for airfoil levels to exceed ACM levels by a ratio that increases with greater microscale shear variance or higher temperature (Appendix B). When we superimpose airfoil spectra onto processed ACM spectra, Φ_s^{wat}, we anticipate some deviation since, in the latter, subsampling leads to aliasing at $k > 3.5$ cpm and correcting for oscillation reduces
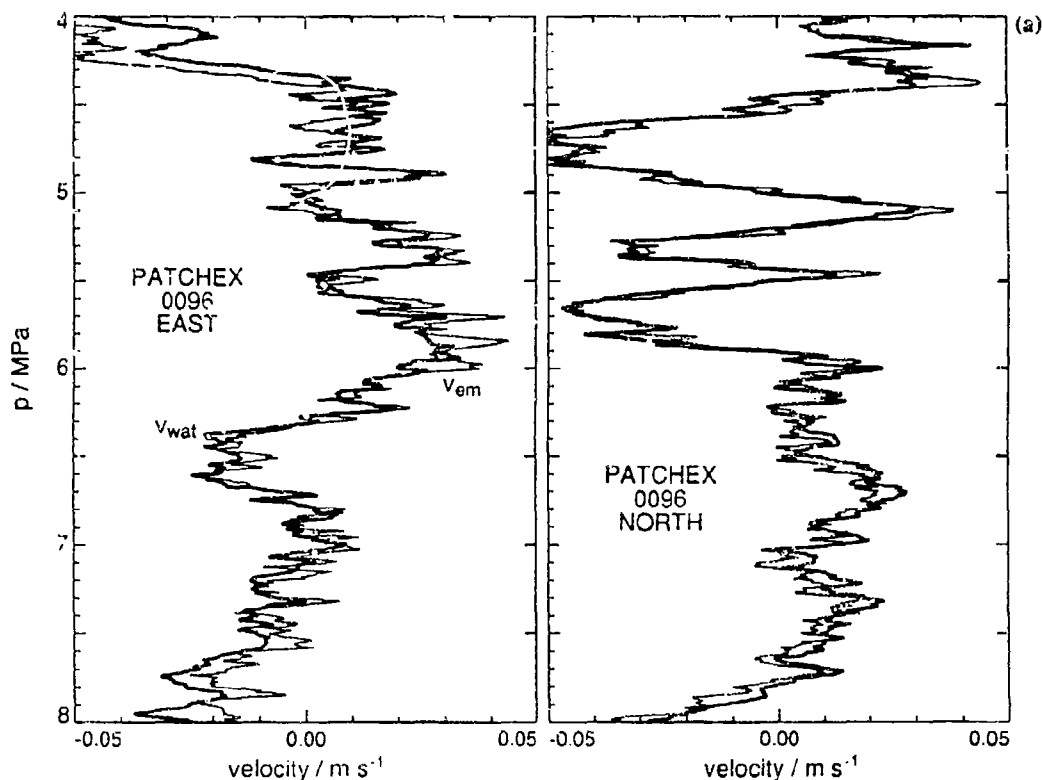
Figure 14. Water velocity profiles from ACM response model (heavy line) and ECM results (light line) for (a) PATCHEX drop 0096 and (b) Florida Straits drop 0241. All profiles are offset for comparison, with those in (b) forced to be near zero at 7 MPa. For the east component at superrotation scales, the ACM–ECM rms difference in (a) is 7 mm s^{-1}; in (b), it is 15 mm s^{-1} from 1 to 6.4 MPa and 7 mm s^{-1} between 3 and 6 MPa. For the north component, the difference in (a) is 4 mm s^{-1}; in (b), it is 19 mm s^{-1} from 1 to 6.4 MPa and 13 mm s^{-1} between 3 and 6 MPa. Note that the velocity scale in (a) is a tenth of that in (b).

levels at $k < 2$ cpm. Nonetheless, there is usually a crossing or close matching somewhere between 1 and 3.5 cpm (Figure 17).

B. Discussion

The results demonstrate our success in combining data from the ECM, ACM, and airfoil probes to resolve velocity and shear in the band from 0.01 to 100 cpm. The response model generates shear spectra that are consistent with the ECM spectra at low wavenumbers and with the airfoil probe spectra at high wavenumbers and reasonably accounts for features of measured ACM spectra in the intermediate band. However, there are uncertainties that require comment.
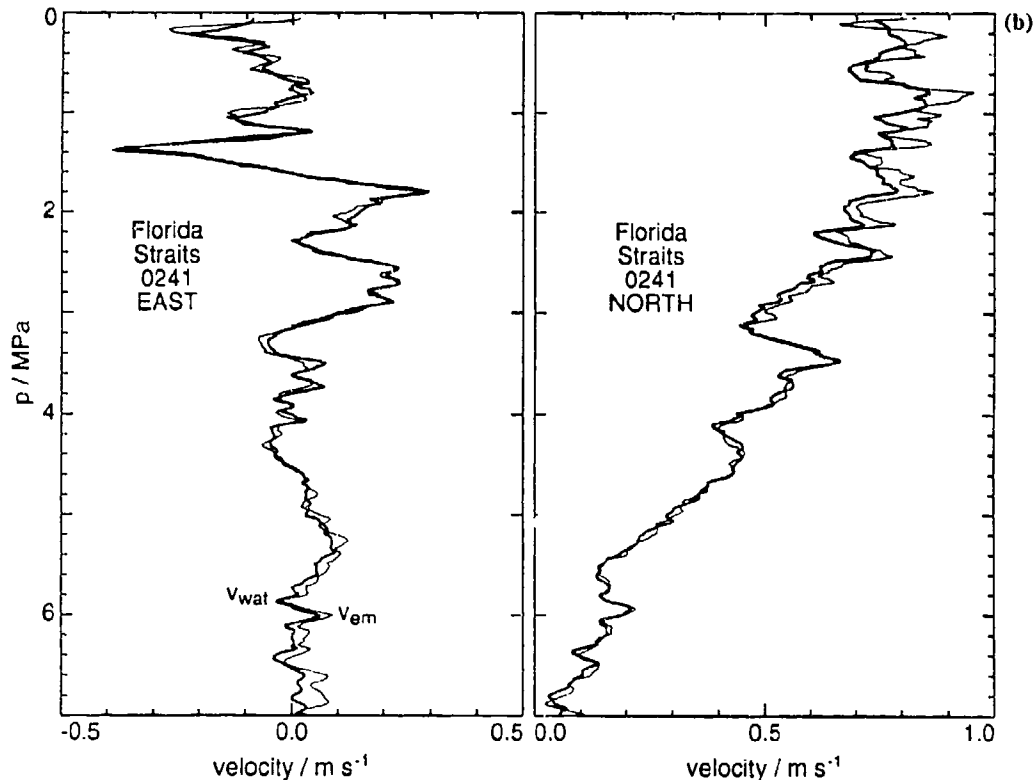
Figure 14, *cont.*

While the agreement of ACM and ECM results is satisfying, we cannot consider the ECM an absolute standard, and so seek further validation. Peters et al. (1991) compare ACM profiles from several MSP drops through the Equatorial Undercurrent (EUC) with simultaneous measurements by an RDI acoustic Doppler current profiler (ADCP) (the ECM was ineffective owing to slow MSP rotation and the proximity of the magnetic equator). Considering mean profiles beneath the EUC core, the shear is 10% higher in the ACM data than in the ADCP data (which was prone to systematic errors in this regime). In contrast, ACM levels for PATCHEX are about 10% lower than the ECM levels (Figure 15). We feel that our low-wavenumber tuning (via H_N) is a good compromise. With the additional concerns from our use of nominal ACM calibrations and neglect of lateral drag and vertical water motions, we estimate a combined uncertainty of 10%–15% in the large-scale ACM results.

At scales around the vehicle's length, there is no standard for objectively judging the ACM profiles. Between 0.1 and 1 cpm, we can only require that spectra are smooth in shape, that is, that the model has decently corrected the effects reflected in the measured spectra. The model meets this criterion fairly well. The similarity to GM76 spectra and coherence with the ECM spectra are also encouraging. Irregularities that sometimes appear near 0.2 and 0.4–0.5 cpm might imply a narrowband uncertainty
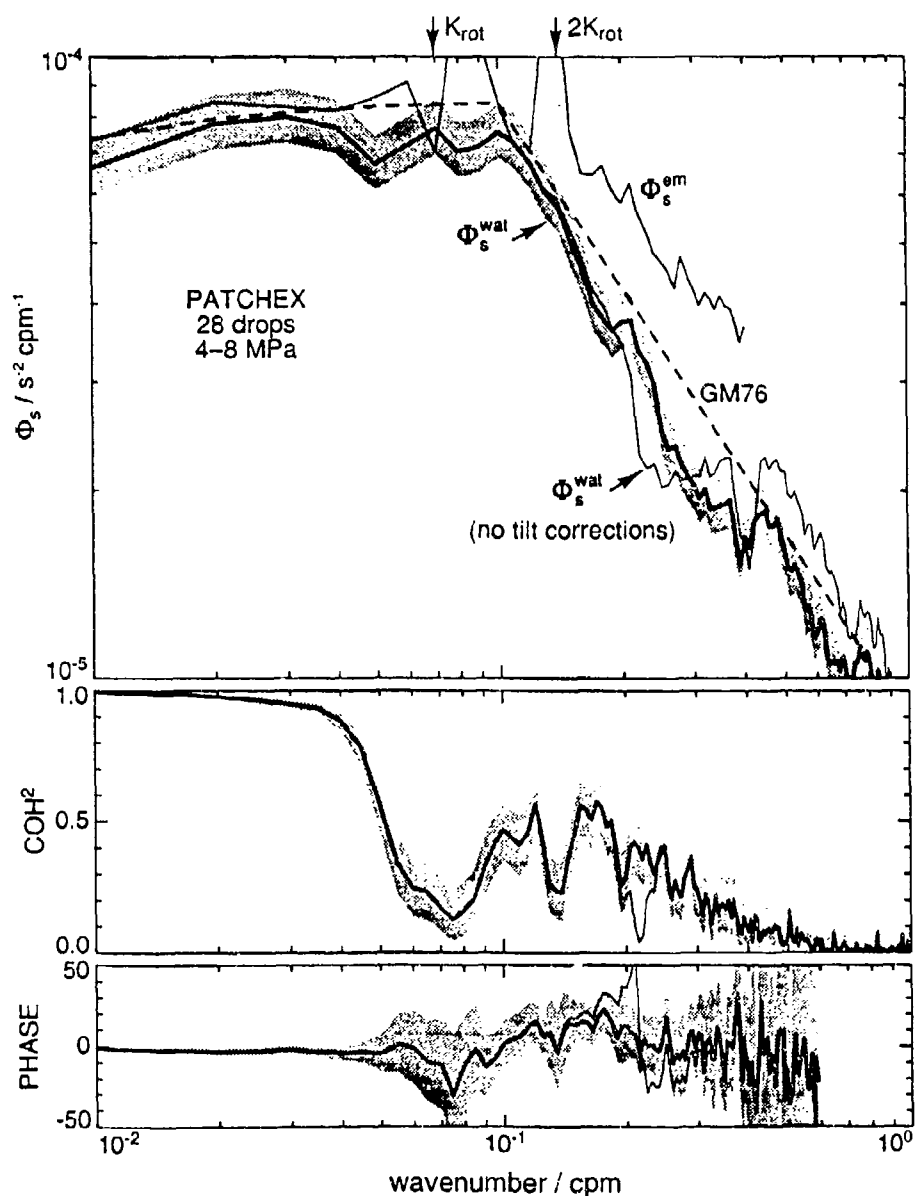
Figure 15. Total shear spectra of 28 PATCHEX drops, 4–8 MPa, computed from ocean velocity profiles. Top panel: ECM spectrum Φ_s^{em} (light line, truncated at 0.4 cpm), standard ACM spectrum Φ_s^{wat} (heavy line, with 95% confidence limits), tiltless ACM spectrum (light line) calculated using $B_f = L_v = 0$ (see text), and GM76 spectrum (dashed line). Bottom panels: Squared-coherence and phase between ACM and ECM velocities (east components), 95% confidence intervals shaded. Heavy lines are for standard ACM; light lines (near 0.2 cpm) are for ACM processing without tilt and oscillation corrections. The phase truncates at 0.6 cpm, where the coherence vanishes.
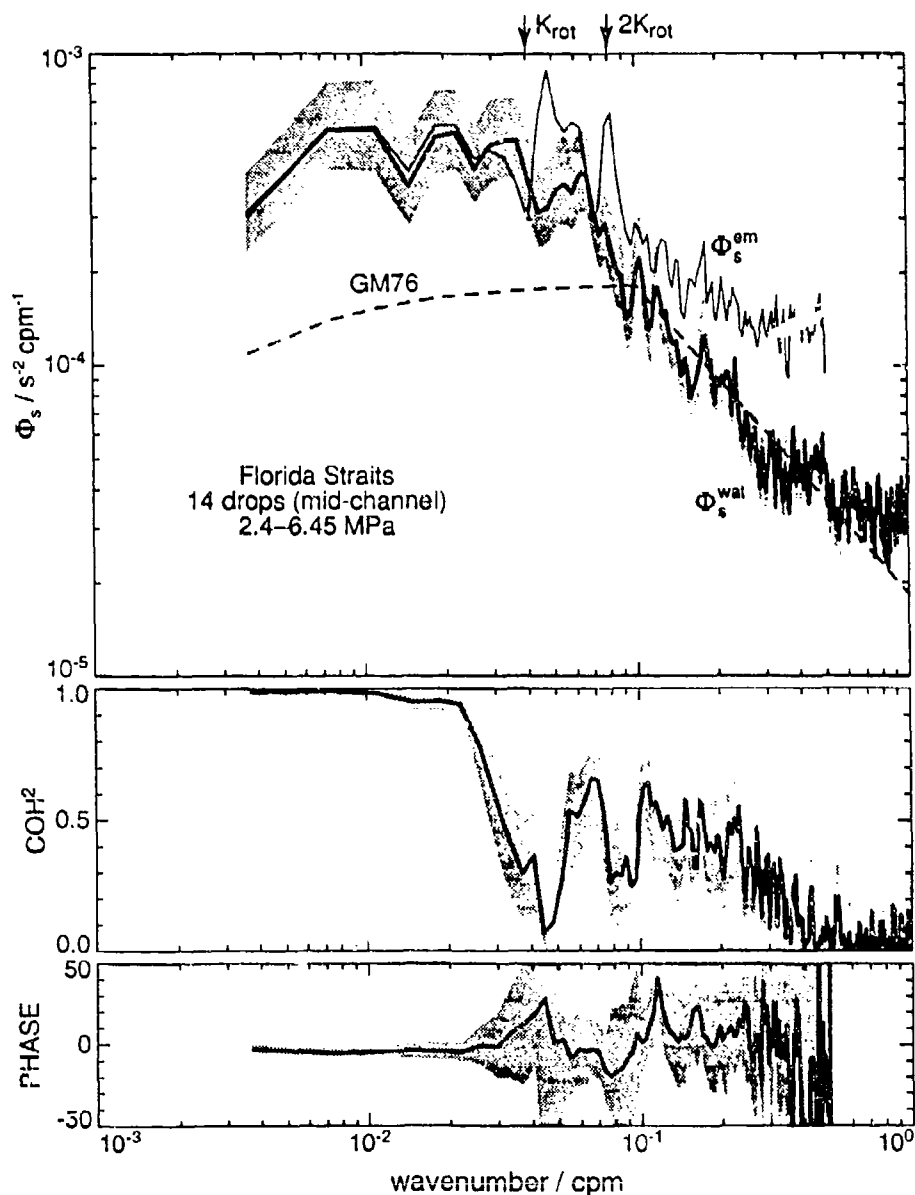
Figure 16. Total shear spectra of 14 midchannel Florida Straits drops, 2.4–6.45 MPa, computed from ocean velocity profiles. Spectral processing is similar to that for PATCH-EX, except that transforms are taken on segments of 2.7 MPa rather than 1.0 MPa. Top panel: ECM spectrum Φ_s^{em} (light line), ACM spectrum Φ_s^{wat} (heavy line), and GM76 spectrum (dashed line, $N = 0.00504$ s^{-1}). Bottom panels: Squared-coherence and phase between ACM and ECM (east components).
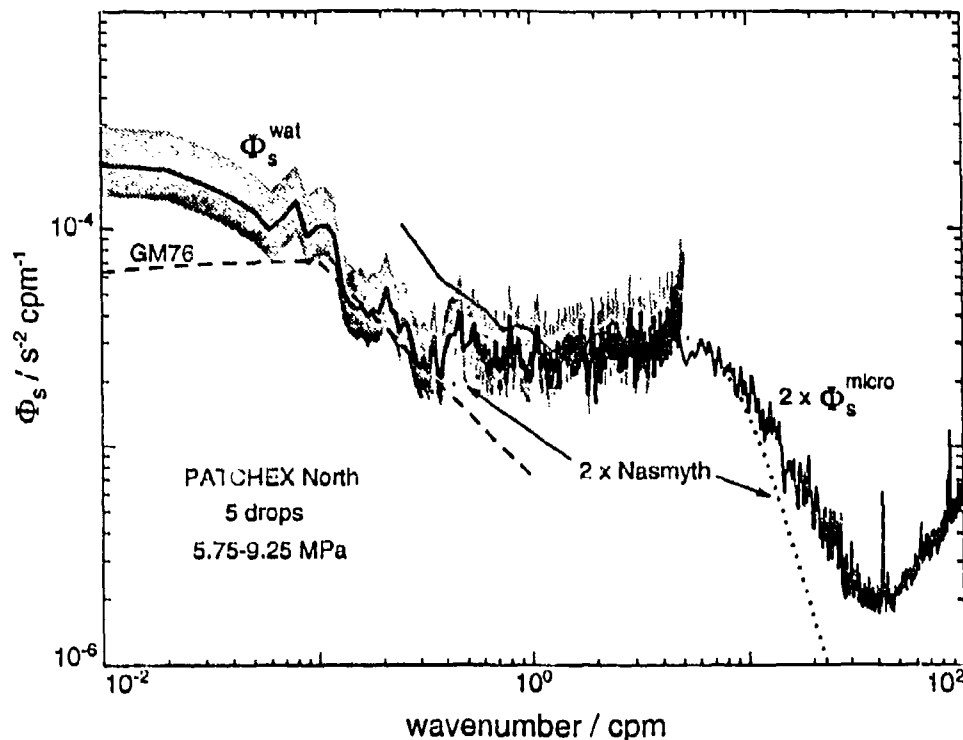
Figure 17. PATCHEX North ACM (Φ_s^{wat}) and airfoil (Φ_s^{micro}) shear spectra computed from 5.75 to 9.25 MPa. The airfoil spectrum is doubled for comparison with the ACM total shear spectrum. The GM76 internal wave model shear spectrum (dashed line, $N = 0.00315$ s^{-1}) and Nasmyth turbulent model shear spectrum (dotted line, $\epsilon = 1.94 \times 10^{-9}$ W kg^{-1}, doubled for comparison) are plotted for reference. The ACM spectrum, corrected for variance removed by the 2-kPa Bartlett window, tails up after 3.5 cpm owing to aliasing (Appendix A). The airfoil spectrum is unreliable before 1 cpm and is at noise levels past 30 cpm.

of 10%-30%, based on their deviation from a smooth spectrum. However, when such spectral features are figured into the integrated shear, their significance is diluted. Individual profiles can suffer from effects that are not obvious in spectral results. For example, the model occasionally generates 5-m oscillations by overamplifying features from the measurements. This is most apparent when shear at neighboring scales (2-10 m) is weak over some depth interval.

For high wavenumbers, we consider the ACM as the standard since it is more stable than the airfoil probes. Their spectral levels compare favorably, especially when considering raw ACM data (Appendix B). The ACM measurements are affected by

oscillation but not by point-mass motion, so the uncertainties come from L_v and from calibration and noise in the ACM and accelerometers. We are satisfied with the microscale results, since our goal is to patch together ACM and airfoil spectra toward resolving shear variance out to the viscous rolloff.

The concerns we have raised thus far are mainly model related. Now we address uncertainties introduced as the ACM measurements are transformed into geomagnetic coordinates. To gauge the potential effect on our results, we perturb zero offsets, calibrations, or alignment adjustments and reprocess the data. For tests run on PATCHEX drops, minor perturbations have little effect on Φ_s^{wat}. Excessive modification of zero offsets (by 10 mm s^{-1} in contrast to expected uncertainties below 2 mm s^{-1}) yields the strongest response, elevating the spectrum tenfold at K_{rot}. Moderately altering the sensitivity (10%) or the alignment (10°) of a single ACM axis increases variance by 5%–15% in the band from 0.17 to 0.25 cpm. These effects appear predominantly in the clockwise component of rotary spectra (computed in the downward-looking oceanographic convention; see Gonella, 1972).

C. Noise and Errors

The ACM noise level sets a lower bound on the noise in our ocean velocity profiles. Unless $N < 10^{-3}$ s^{-1}, spectra conforming to GM76 stay above the ACM noise floor (10^{-8} m^2 s^{-2} cpm^{-1}) for $k < 1$ cpm. Low-pass filtering the raw data reduces the rms noise; transforming to geomagnetic coordinates and correcting for oscillation could add some noise. The degree of uncertainty in the model results depends on the scale. For scales over 10–20 m, where velocity variance resides, the effect is equivalent to a 10%–15% calibration uncertainty. At scales exceeding the rotation length, rms differences between ECM and ACM profiles are 3–20 mm s^{-1}. For 2–10 m, the vehicle response fluctuates such that the model amplifies some scales and attenuates others. Sensitivity is greatest around the 5-m scale. We estimate uncertainties of 10% in general and up to 30% at spectral irregularities. To assess uncertainty in a specific profile, we could examine the effects as the model is run over a range of parameter values.

Our studies rely more on shear and Richardson numbers than on velocity profiles. Noise and uncertainty in shear depend on the scale over which it is computed. If larger scales are the focus, we reduce the noise by filtering the velocity data. Regarding shear spectra noise levels, the ACM and the airfoil probes are both around 4 × 10^{-7} s^{-2} cpm^{-1} at 1 cpm, with the ACM floor sloping up thereafter and that of the airfoils falling slightly out to 30 cpm. Uncertainty in shear is related to that in velocity; it is easier to quantify at large scales than at intermediate scales. Unfortunately, shear is concentrated at scales where the response model is most questionable. Again, we could make specific error estimates by running repeated simulations on the drops in question.

Gregg (1979) presents several formulae for estimating relative uncertainty and noise in computed quantities. The relative noise σ_{Ri}/Ri increases with noise of the temperature, conductivity, pressure, and velocity sensors, decreases with larger interval size, and increases with the actual value of Ri. For MSP, noise of the CTD sensors contributes much more than that of the ACM. While we can apply the relation to estimate σ_{Ri}/Ri for a given MSP profile, we must rely on repeated simulations to estimate relative uncertainty.

VI. CONCLUSIONS AND SUMMARY

High-quality measurements mark the sound performance of MSP. Success comes from the combined abilities of its sensor systems coupled with its advantageous behavior as a platform. The drag brushes slow the descent, enhancing resolution of temperature microstructure. With a fall that is quiet and low in vibration, MSP can detect a wide range of viscous dissipation rates. Rapid sampling of temperature and velocity data allows broadband comparisons between fine-scale and microscale sensors. In particular, ACM data are useful in assessing the veracity of airfoil spectral levels. The ECM provides a check on large scale ACM results without deployment of extra equipment (as would be required, for instance, with acoustic tracking). Adjustable turning blades spin the vehicle, meeting a requirement of the ECM method. Rotation also enables determination of bias and misalignment in the ACM, accelerometer, and magnetometer channels. A single set of accelerometers is sufficient for monitoring vehicle tilt, since free oscillation is suppressed by damping and off-resonant forcing at the tail. However, by strengthening lateral forcing, the tail array of brushes and blades adversely affects the ACM measurements.

We have focused this report on our treatment of the ACM data because the resulting oceanic profiles and spectra are central to MSP investigations of shear and mixing. With its stability and low noise, the ACM can resolve motions on vertical scales from 1 to 10 m and beyond. It measures the relative flow past its transducers, and thus proper interpretation of the data requires knowledge of the orientation and motion of the platform. Determining the gross vehicle motion is the most difficult task, for which we rely on a computational model based on our understanding of the horizontal dynamics affecting MSP. At large scales, forcing at the nose couples MSP to the flow, much like the profilers TOPS and HRP. The troublesome aspect of the response is the tendency of MSP, because of enhanced tail forcing, to follow motions of scales near its own length. This behavior, combined with the swaying of the ACM from tilt oscillations, complicates the ACM measurements such that their spectra are deeply notched near 0.2 cpm with lesser contortions thereafter. To be successful, our model must account for such features in the measured spectra. While ECM results guide us at scales exceeding the rotation length, no standard exists at smaller scales.

The transformation from ACM data into oceanic velocity profiles occurs in stages. First, we use magnetometer data to resolve the ACM and accelerometer data into geomagnetic coordinates. Next, we remove vehicle tilt and oscillation from the ACM measurements, inferring the corrections from tilt-dominated accelerometer data. The model simulates the gross horizontal motion of the vehicle as it is responds to forces at the nose and tail. Three parameters specify the location and strength of each force in proportion to the oncoming relative flow. We manufacture the vehicle velocity by integrating the modeled accelerations and then compute the ocean

velocity by adding on the corrected relative measurements. Rather than adhering to supposed or theoretical values for the parameters, we adjust them empirically by matching analytic transfer functions to the observed response.

Velocity profiles and shear spectra produced by the ACM processing satisfy most of our stated objectives and criteria. At large scales, the ACM results agree well with ECM profiles and spectra. The accelerometers and response model capture the effects—oscillation and tail forcing—that shape the measured spectra between 0.1 and 1 cpm. Consequently, our ocean shear spectra are fairly smooth within this difficult band, aside from minor deviations near 0.2 and 0.4–0.5 cpm. Airfoil and ACM spectra usually cross or overlap between 1 and 3 cpm. The consistency between ECM, ACM, and airfoil results confirms the ability of MSP to resolve oceanic shear spectra from 0.01 to 100 cpm.

Overall, we are satisfied with our ACM results, but we do have some comments and concerns. Considering sensitivities in the measurements and model parameters, uncertainty in spectral levels is 10% in general, but is potentially higher near 0.2 cpm and near the rotation wavenumber, K_{rot}. Some parameters differ significantly from their predicted values: a strong nose force and an upwardly displaced tail force are required for success. In the spatial domain, some portions of profiles should be viewed with suspicion. Near the surface, results are confounded by surface waves, vehicle spinup, and startup transients in the model. Neglect of lateral drag on the main tube may cause the model to underestimate acceleration through sharp or strong shear features. The model's extreme response at 0.2 cpm can generate unrealistic 5-m oscillations in velocity or shear profiles (more of a concern for the large-tail configuration than for the small-tail one). Finally, velocity profiles contain depth-independent offsets and extend to no more than 1200-m depth.

We compare MSP with TOPS and HRP in terms of vehicle behavior and treatment of ACM data. In some ways, MSP is superior in acquiring data: a slow, quiet fall improves microstructure measurements, rapid sampling allows more flexibility in data processing, and the ECM provides an onboard check on ACM results. However, the drag brushes and turning blades that control the descent also complicate the ACM measurements by causing MSP to be more responsive than the other profilers. Regarding vehicle tilt, both MSP and HRP improve upon the weakly damped resonant response of TOPS. With its greater length, HRP attains a strong righting moment and large moment of inertia, leading to rapid damping of its free oscillation. In contrast, the tilt response of MSP is more forced than free, as opposing nose and tail forces tip the vehicle. Also, the tail effectively stiffens and damps the resonant mode. A tailless MSP would oscillate badly, judging from the proximity of its centers of buoyancy and gravity. The TOPS model couples the equation for gross vehicle motion to that for vehicle tilt. The primary use of its noise-limited accelerometer

measurements is in tuning the tail force parameter. Neither MSP nor HRP processing includes tilt dynamics in modeling vehicle velocity. Both remove oscillation effects from their ACM measurements, but only the MSP corrects for the component of fall rate detected with tilt. One set of accelerometers suffices for monitoring MSP's tilt; HRP has sensors at both ends to decouple tilt from other acceleration signals. All three models employ a linear nose force and ignore lateral drag, vertical water motion, and rotation effects. Peaks near the pendulum frequency dominate spectra of TOPS accelerometer and ACM measurements; it is only in the transfer function between the two that effects of tail forcing are apparent. The HRP model omits the tail force, as oscillation correction seems competent to account for spectral irregularities. The MSP model requires a tail force to explain the 0.2-cpm notch and surrounding features in the measured ACM spectra. By eliminating dependence on fall rate and combining several physical parameters, we employ only six simple parameters in our vehicle response model. We use model transfer functions to select parameter values, to assess model sensitivities, and to plan modifications toward improving vehicle response.

Much of the design of MSP involves controlling and monitoring vehicle motion. The array of drag brushes and turning blades affects all aspects of the response—vertical, horizontal, and tilting. The large-tail configuration met our goal of a slow descent but adversely affected the ACM measurements by making MSP respond too quickly to horizontal flow. We diminished the horizontal response, at the cost of a quicker descent, by reducing the width of the tail array (there were no significant changes in vehicle tilt or vibration). Our desire for a fairly steady fall rate precludes lessening the negative buoyancy to compensate for the weaker drag. Weighing the important benefits to the ACM measurements and processing against the minor loss in resolution of temperature microstructure, we conclude that the small-tail configuration is a valuable advance in MSP's design.

REFERENCES

Allen, H. J., and E. W. Perkins, 1952: A study of effects of viscosity on flow over slender inclined bodies of revolution. National Advisory Council for Aeronautics Report No. 1048, 13 pp.

Bendat, J. S., and A. G. Piersol, 1971: *Random Data: Analysis and Measurement Procedures.* Wiley-Interscience, 407 pp.

Brown, N. L., and K. D. Lawson, 1980: A high precision acoustic current sensor. *Near Surface Ocean Experimental Technol. Workshop Proc.*, R. Swenson and R. Mesecar, Eds., Naval Ocean Research and Development Activity, Bay St. Louis, MS, 57–74.

Carson, R. M., and J. J. Simpson, 1978: Comment on 'Design considerations of wing stabilized free-fall vehicles' by A. C. Mortensen and R. E. Lange. *Deep-Sea Res.*, **25**, 577–579.

Chave, A. D., D. J. Thomson, and M. E. Ander, 1987: On the robust estimation of power spectra, coherences, and transfer functions. *J. Geophys. Res.*, **92**, 633–648.

Evans, D. L., H. T. Rossby, M. Mork, and T. Gytre, 1979: YVETTE—a free-fall shear profiler. *Deep-Sea Res.*, **26**, 703–718.

Desaubies, Y. J. F., and M. C. Gregg, 1978: Observations of internal wave vertical velocities by a free-fall vehicle. *Deep-Sea Res.*, **25**, 933–946.

Gargett, A. E., P. J. Hendricks, T. B. Sanford, T. R. Osborn, and A. J. Williams III, 1981: A composite spectrum of vertical shear in the upper ocean. *J. Phys. Oceanogr.*, **11**, 1258–1271.

Garrett, C. J. R., and W. H. Munk, 1975: Space-time scales of internal waves: A progress report. *J. Geophys. Res.*, **80**, 291–297.

Gonella, J., 1972: A rotary-component method for analyzing meteorological and oceanographic vector time series. *Deep-Sea Res.*, **19**, 833–846.

Gregg, M. C., 1979: The effects of bias error and system noise on parameters computed from C, T, P and V profiles. *J. Phys. Oceanogr.*, **9**, 199–217.

Gregg, M. C., and T. B. Meagher, 1980: The dynamic response of glass rod thermistors. *J. Geophys. Res.*, **85**, 2779–2786.

Gregg, M. C., and E. Kunze, 1991: Shear and strain in Santa Monica Basin. *J. Geophys. Res.*, **96**, 16,709–16,719.

Gregg, M. C., and T. B. Sanford, 1980: Signatures of mixing from the Bermuda Slope, the Sargasso Sea, and the Gulf Stream. *J. Phys. Oceanogr.*, **10**, 105–127.

Gregg, M. C., and T. B. Sanford, 1988: The dependence of turbulent dissipation on stratification in a diffusively stable thermocline. *J. Geophys. Res.*, **93**, 12,381–12,392.

Gregg, M. C., D. P. Winkel, and T. B. Sanford, 1991: Internal wave shear and dissipation. *Dynamics of Oceanic Internal Gravity Waves, Proc., 'Aha Huliko'a Hawaiian Winter Workshop,* SOEST Spec. Publ., P. Müller and D. Henderson, Eds., pp. 1–29.

Gregg, M. C., D. P. Winkel, and T. B. Sanford, 1993: Varieties of fully resolved spectra of vertical shear. *J. Phys. Oceanogr.*, **23**, 124–141.

Hayes, S. P., H. B. Milburn, and E. F. Ford, 1984: TOPS: A free-fall velocity and CTD profiler. *J. Atmos. Oceanic Technol.*, **1**, 220–236.

Ninnis, R., 1984: The effects of spatial averaging on airfoil probe measurements of oceanic velocity microstructure, Ph.D. dissertation, Univ. of B. C., Vancouver, Canada, 109 pp.

Oakey, N. S., 1982: Determination of the rate of dissipation of turbulent energy from simultaneous temperature and velocity shear microstructure measurements. *J. Phys. Oceanogr.*, **12**, 256–271.

Osborn, T. R., 1974: Vertical profiling of velocity microstructure. *J. Phys. Oceanogr.*, **4**, 109–115.

Osborn, T. R., and W. R. Crawford, 1980: An airfoil probe for measuring velocity fluctuations in water. *Air-Sea Interaction: Instruments and Methods,* F. Dobson, L. Haase and R. Davis, Eds., Plenum Press, 369–386.

Peters, H., M. C. Gregg, and T. B. Sanford, 1991: Equatorial and off-equatorial fine-scale and large-scale shear variability at 140°W. *J. Geophys. Res.*, **96**, 16,913–16,928.

Sanford, T. S., R. G. Drever, and J. H. Dunlap, 1978: A velocity profiler based on the principles of geomagnetic induction. *Deep-Sea Res.*, **25**, 183–210.

Schmitt, R. W., J. M. Toole, R. L. Koehler, E. C. Mellinger, and K. W. Doherty, 1988: The development of a fine- and microstructure profiler. *J. Atmos. Oceanic Technol.*, **5**, 484–500.

Singleton, R. C., 1969: An algorithm for computing the mixed radix fast Fourier transform. *IEEE Trans. Audio Electroacoust.*, **AU-17**, 93–103.

Winkel, D. P., M. C. Gregg, and T. B. Sanford, 1992: Simultaneous observations of shear and turbulence in the Florida Current. *Preprints, Tenth Symposium on Turbulence and Diffusion,* Portland, Amer. Meteor. Soc., (j5)101–104.

Wrigley, W., Hollister, W. M., and Denhard, W. G., 1969: *Gyroscopic Theory, Design, and Instrumentation.* M. I. T. Press, 432–435.

Appendix A: SENSORS AND DATA PROCESSING

1. ACM: Noise and Aliasing

The acoustic current meter detects the relative velocity of water moving between its paired transducers. At intervals of 250 μs, each pair simultaneously transmits 2.75-MHz pulses of 75-μs duration, whose phases upon arrival at opposing sides differ owing to the water motion. Received signals are heterodyned with a frequency 156 Hz greater than that of the transmission, and the output is bandpassed to retain only the 156 Hz difference component. Further signal processing yields, at about 312 Hz, voltages proportional to phase differences and, thereby, to velocities (Brown and Lawson, 1980). This ACM output is low-passed through a 10-Hz Chebyschev filter, subsampled at 62.5 Hz, and digitized with 16 bits. The static sensitivity of the ACM is kc^2/df, where $k = 0.025$ is a circuit-related calibration factor, c is the speed of sound (in meters per second), d is the transducer separation (0.2 m), and f is the carrier frequency (2.75 MHz); nominally, using $c = 1500$ m s^{-1}, the sensitivity is 0.1023 (m s^{-1})/V. We used this nominal value until the Florida Straits cruise before which we calibrated the ACM by repeatedly towing it in a salt-water tank.

When formed over short intervals, spectra from either ACM axis hit a noise floor near 10^{-8} (m s^{-1})^2 Hz^{-1} and drop sharply at 10 Hz owing to the low-pass filter (Figure A1). Narrow-banded oscillations of drifting frequency show up as spectral spikes, such as those at 1.6 and 9 Hz in Figure A1. They rise around an order of magnitude above the noise floor, although their amplitudes differ between axes and from cruise to cruise. We reproduced the behavior by cooling one of the oscillator crystals and forming spectra as it warmed to room temperature. Circuit modifications were then made that reduced the spiking and lowered the noise floor. In so doing, the carrier frequency (f) was slightly lowered, necessitating the empirical recalibration. Because of their drifting frequency, the spikes are smeared out in ensemble spectra formed over large intervals and multiple drops, effectively doubling the level of the noise floor.

The effects of digitally filtering and subsampling the ACM data are shown in Figure A2, which tracks velocity spectra through four stages of processing.

1. The initial spectrum is formed from linearly calibrated, fully sampled ACM data; then the average fall rate over the indicated drops and pressure range is used to convert from frequency to wavenumber. For each ACM axis, spectra computed for 0.08-MPa (8-m) segments spanning the pressure range are ensemble averaged to form the autospectrum. Displayed in Figure A2 is the total spectrum, the sum of the two component spectra.

TR 9414 A1
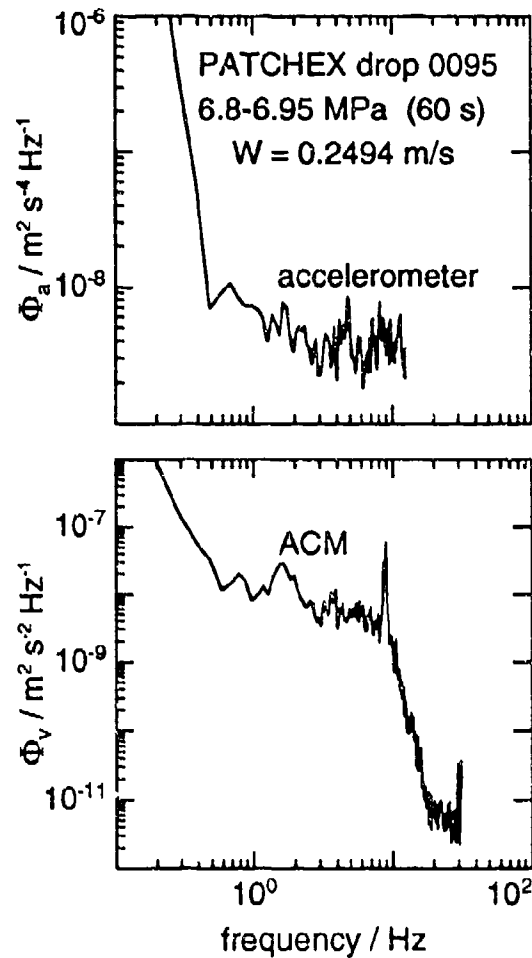
Figure A1. Drop 0095, single-axis spectra from accelerometer (top) and ACM (bottom). Each spectrum is the ensemble average of successive 10-s segments (about 2.5 m) spanning the 60-s interval from 6.8 to 6.95 MPa.

2. Smoothing the data with a 2-kPa (0.2-m) Bartlett window attenuates the spectrum past 1 cpm and halves the rms noise. The effect is equivalent to multiplying the unfiltered spectrum by

$$H_{\mathrm{BW}}^2(k) = \left(\frac{\sin(2\pi k L/4)}{2\pi k L/4} \right)^4 ,$$

where $L = 0.2$ m is the full width of the window and k is in cycles per meter.

A2   TR 9414
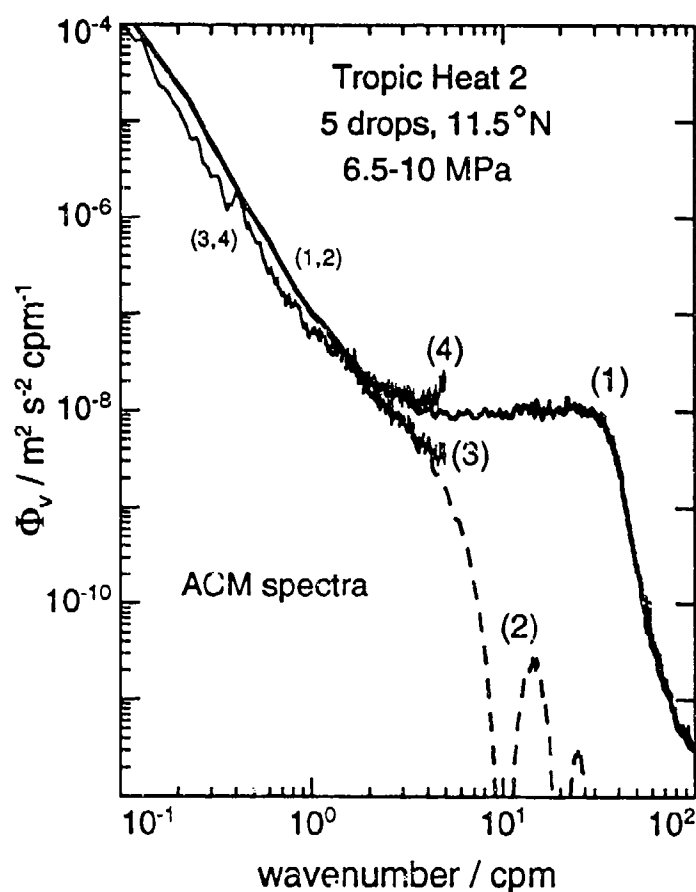
Figure A2. Example of effects of filtering and subsampling on ACM velocity spectra, five Tropic Heat 2 drops at 11.5°N. Autospectra of the two orthogonal components are summed to yield the displayed spectra of total horizontal variance. Spectra represent (1) linearly calibrated 62.5-Hz data; (2) data from (1) filtered with a 20-kPa Bartlett window; (3) ocean velocity data on a 10-kPa grid (v_{wat}); (4) spectrum from (3) compensated for the 20-kPa Bartlett filter.

3. Subsampling the filtered data onto a 1-kPa (0.1-m) grid folds variance past the Nyquist wavenumber of 5 cpm to lesser wavenumbers, leading to noticeable aliasing from 3.5 to 5 cpm. This spectrum represents the 1-kPa ocean velocities (v_{wat}) obtained by removing vehicle motion from geomagnetically resolved ACM data. The 3.5-MPa pressure range is divided into 1-MPa (100-m) segments, with successive segments overlapped by 50%. For each segment, the velocity data (1000 points) are first-differenced, demeaned, and Hann filtered. Singleton's (1969) method is used to take the Fourier transform, and the resulting autospectra are corrected for the first-differencing and for the variance lost

from the Hanning window. The total velocity spectrum is the sum of the east and north autospectra. Finally, spectra from all 1-MPa segments are ensemble averaged.

4. The last step divides the previous spectrum by $H_{BW}^2(k)$ to recover the variance filtered out by the Bartlett window.

The initial (1) and final (4) spectra coincide from 1.5 to 3.5 cpm. The upward hooking of the final spectrum at its highest wavenumbers emphasizes its contamination by aliasing. They differ at lower wavenumbers because of the conversion from relative to ocean velocity and also because of the difference in windowing and associated Hanning weights: segment sizes for raw velocity were 0.08 MPa while those for ocean velocity were 1.0 MPa.

Spectra exhibited earlier in this document were formed using the processing steps described for stages (3) and (4); shear spectra were obtained by multiplying velocity spectra by the square of the radian wavenumber, $(2\pi k)^2$.

2. Accelerometers and Quantization Noise

Prior to 1989, Sundstrand Q-flex model QA-1100 accelerometers were used in MSP with nominal calibrations. They were replaced by model QA-1400 sensors, each with its own manufacturer-supplied calibration. There is little difference in the performance of the two models. Quantization sets the noise floor at around 5×10^{-9} (m s^{-2})^2 Hz^{-1} (Figure A1). The rms noise of 2.6×10^{-4} m s^{-2} (Table 3) results from muliplying this spectral floor by the Nyquist frequency of 12.5 Hz. This quantization noise exhibited by our 16-bit A/D is thrice the level of $(q^2/12)$—where q is the resolution—predicted by Bendat and Piersol (1971). (Note that the 125-Hz temperature and conductivity channels are also quantization-limited.) To avoid contaminating ACM velocities, noise is filtered out of the small-scale ($k > 1$ cpm) accelerometer data before tilt and oscillation corrections are computed.

3. Sensor-to-Instrument Transformation

An orthogonal coordinate system is defined on the vehicle as a reference for the sensor systems. This right-handed ijk frame has the vertical k axis up the geometric centerline, the i axis radially outward toward an inked line on the main tube, and the j axis 90° anticlockwise from the i axis (looking from above). The horizontal components of each sensor system define ab coordinates, with the magnetometer also measuring along a vertical c axis. The magnetometer and accelerometer axes are closely aligned with the instrument frame, while the ACM and ECM are rotated in the ij plane. Zero offsets (bias) and uncertainties in sensitivity and alignment of the sensor axes are considered as data are mapped to ijk coordinates.

The drifting offsets in the ECM data are estimated with a low-frequency spline, as illustrated in Figure 5. For the ACM and accelerometers, zero offsets are estimated for each drop by averaging the data over a deep, thick interval encompassing an integral number of vehicle rotations. These averages ought to be zero, assuming that small-scale oceanic shear is reasonably stationary with depth (Hayes et al., 1984). Therefore, deviations from zero are attributed to sensor bias.

Treatment of magnetometer data relies on the constancy of the geomagnetic field, $\mathbf{B} = B_H\,\hat{\mathbf{y}} + B_Z\,\hat{\mathbf{z}}$, during a drop (although $\hat{\mathbf{z}}$ is downward in the discussion of the point-mass model, it is upward in this appendix, so $B_Z < 0$ at northern latitudes). Along with an angle to orthogonalize the two horizontal axes, offsets and scaling factors are found such that the adjusted data describe most closely, in the least-squares sense, a circle of radius B_H. For the vertical axis, an offset, a scaling factor, and two angular adjustments (described below) are found such that the adjusted data deviate minimally from B_Z.

The transformation of data from the measured horizontal components to the instrument frame consists of three steps. In the following, (d_a, d_b) refers to the original data for any of the sensor systems (ACM, ECM, accelerometers, or magnetometer). First, the measurements are adjusted using

$$d_{a'} = s_a(d_a - o_a) \qquad \text{and} \qquad d_{b'} = s_b(d_b - o_b)$$

to apply zero offsets (o_a, o_b) and scaling factors (s_a, s_b). Next, with the a axis as the reference so that $d_{a''} = d_{a'}$,

$$d_{b''} = (d_{a'} \sin \delta\psi_{\text{orth}} + d_{b'})/\cos \delta\psi_{\text{orth}}$$

orthogonalizes the data for an angular deviation $\delta\psi_{\text{orth}}$ of the b axis (for magnetometer and ECM, only). Finally, given the angle ψ_{inst} from the MSP i axis to the sensor a axis,

$$d_i = d_{a''} \cos \psi_{\text{inst}} - d_{b''} \sin \psi_{\text{inst}}$$
$$d_j = d_{a''} \sin \psi_{\text{inst}} + d_{b''} \cos \psi_{\text{inst}}$$

completes the conversion to instrument coordinates (accelerometers and magnetometer assume $\psi_{\text{inst}} = 0$).

The vertical magnetometer measurements are offset and scaled, and the resulting $b_{c'}$ are orthogonalized via

$$b_{c''} = [b_{c'} - (b_{a''} \cos \delta\psi_c + b_{b''} \sin \delta\psi_c) \sin \delta\theta_c] / \cos \delta\theta_c ,$$

where the c axis is at angle $\delta\theta_c$ to the k axis and its projection onto the ij plane is at angle $\delta\psi_c$ to the a axis. The last step is trivial, $b_k = b_{c''}$.

4. Instrument-to-Geomagnetic Transformation

The orientation of the instrument relative to the geomagnetic frame can be expressed in terms of rotations through three Euler angles (Wrigley et al., 1969). Given reliable magnetometer (b_i, b_j, b_k) and accelerometer (a_i, a_j, a_k) measurements, these Euler angles can be determined and used in constructing an orthonormal matrix that transforms data from the ijk frame to the xyz frame (J. H. Dunlap, APL-UW, "Coordinate Transformation for MSP Data," September 1985). The ECM processing employs this technique, one result of which is the removal of all tilt effects from the accelerometer and magnetometer data (i.e., $a_x = a_y = b_x = 0$, $a_z = g$, $b_y = B_H$, and $b_z = B_Z$).

For the ACM processing, geomagnetically resolved tilt data are needed so that corrections for platform oscillation can be made. Therefore, an alternate approach must be taken in which the rotational orientation of the vehicle is determined solely from the horizontal magnetometer data. The task is to find the angle ϕ from the eastward x axis to the instrument i axis.

Before ϕ is computed, the tilt contributions in b_i and b_j are removed. Otherwise, noise or uncertainty at the order of the tilt angles (less than 1°) is generated in the rotation angles. The tilt along the instrument axes is estimated from the accelerometer data,

$$\theta_i = a_i/g \quad \text{and} \quad \theta_j = a_j/g\,,$$

and is then used to adjust the horizontal magnetometer measurements,

$$b_{i'} = b_i - B_Z \sin\theta_i \quad \text{and} \quad b_{j'} = b_j - B_Z \sin\theta_j\,.$$

The rotation angle is such that

$$\sin\phi = \frac{b_{i'}}{(b_{i'}^2 + b_{j'}^2)^{1/2}} \quad \text{and} \quad \cos\phi = \frac{b_{j'}}{(b_{i'}^2 + b_{j'}^2)^{1/2}}\,.$$

Now, the ACM, accelerometer, and uncorrected magnetometer data are transformed to the geomagnetic frame via

$$
\begin{aligned}
d_x &= d_i \cos\phi - d_j \sin\phi \\
d_y &= d_i \sin\phi + d_j \cos\phi \\
d_z &= d_k\,,
\end{aligned}
$$

in which tilt contributions remain.

Depending on the method—the Euler technique or the use of horizontal magnetometer data with or without tilt effects—the estimated rotation angle varies slightly. Owing to the small tilts of MSP, the differences among the methods are too small to be significant in geomagnetically resolving the ECM or ACM data.

5. ECM

The conversion from the ECM measurements (e_x, e_y) in microvolts to velocity in meters per second is

$$v_x = \frac{1000}{B_Z \, d_e (1 + c_1)} \, e_y$$

$$v_y = \frac{-1000}{B_Z \, d_e (1 + c_1)} \, e_x - \frac{B_H (1 + c_2)}{B_Z (1 + c_1)} \, W ,$$

where the geomagnetic field is in nanoteslas, the electrode separation d_e is 0.42 m, constants c_2 and c_1 (0.97 and -0.03) are related to the approximation of MSP as an electrically insulating prolate spheroid (Sanford et al., 1978), and the fall rate is $W = W_{msp} > 0$.

6. Tilt Angles from Magnetometer Data

In the ACM processing, the neglect of MSP's small tilt angles places the transformed data in coordinates that are slightly tipped from the geomagnetic frame. The remnant accelerometer signals allow correction of the ACM data for tilt oscillation as well as position. Tilt-induced signals also remain in the magnetometer data. We consider these signals, (b_x, b_y, b_z), for small tilt components θ_x and θ_y. With tilt confined to the yz plane,

$$b_x = 0$$
$$b_y = B_Z \sin\theta_y + B_H \cos\theta_y$$
$$b_z = B_Z \cos\theta_y - B_H \sin\theta_y .$$

When tilt in the xz plane is added, some of b_z projects onto the x axis, with

$$b_x = B_Z \cos\theta_y \sin\theta_x - B_H \sin\theta_y \sin\theta_x$$
$$b_y = B_Z \sin\theta_y + B_H \cos\theta_y$$
$$b_z = B_Z \cos\theta_y \cos\theta_x - B_H \sin\theta_y \cos\theta_x$$

as the approximate result (the same result occurs, to first order in the small angles, when considering the tilts in reverse order or when following the exact and more lengthy analysis). Therefore, for small θ_x and θ_y and from the above expressions, we can estimate

$$\theta_x = \frac{b_x}{B_Z} \quad \text{and} \quad \theta_y = \frac{b_y - B_H}{B_Z} = \frac{B_Z - b_z}{B_H} \qquad \text{[radians]} \qquad (A1)$$

from the tilt-affected magnetometer data.

Appendix B: DATA PROCESSING FOR AIRFOIL PROBES

1. Sensitivity and Calibration of Airfoil Probes

An airfoil probe responds to velocity fluctuations that push on its sensitive tip, deflecting the piezoelectric bimorph beam contained within (Osborn and Crawford, 1980; Oakey, 1982). The induced voltage is approximately proportional to the forcing normal to the beam. As discussed in Appendix C regarding the vehicle response, potential flow theory predicts a linear pressure force across a slender, axisymmetric body for flows in which the lateral component, v, is small relative to the axial, w. The total pressure force, $F \propto vw$, is distributed evenly along the paraboloidal tip. We use Oakey's method for calibration, oscillating the probes in a laminar jet of speed w. Peak-to-peak voltages are fit against $\Delta v = w \sin \Delta\theta$, the range of lateral velocity implied by the known oscillation magnitude, to determine the calibration factor, S_v (in volts per meter); inferring w from the measured pressure head ($w^2 = 2gh$) accounts for the odd units. Now, with MSP falling at speed W, a signal of

$$E = \frac{S_v W}{2g} v \qquad \text{[V]}$$

should result from a turbulent fluctuation velocity of v. With increasing angle of attack, however, cross drag forcing also contributes significantly, and therefore the above formulation will underestimate the induced voltage (Osborn and Crawford, 1980).

Airfoil signals are conditioned before they are presented to the A/D converter. The voltage is boosted by a charge amplifier (in proportion to the probe's effective capacitance, C_s) and a gain adjusting amplifier, higher-frequency (smaller-scale) fluctuations are emphasized by a differentiating circuit, and high-frequency noise is suppressed by a 30-Hz four-pole Chebyschev filter. The probe itself has dependencies both spatial, as the tip smooths out small-scale fluctuations, and temporal, as the beam equilibrates to attenuate slow variations. Altogether, the transformation from a velocity spectrum, $\Phi_{vel}^{(Hz)}(f)$ [m^2 s^{-2} Hz^{-1}], into a raw voltage spectrum, $\Phi_{raw}^{(Hz)}(f)$ [V^2 Hz^{-1}] is given by

$$H_{EL}^2(f)\, H_{NIN}^2(f/W)\, S^2\, \Phi_{vel}^{(Hz)}(f) = \Phi_{raw}^{(Hz)}(f) \,,$$

where $S = S_v W/2g$. The combined electronic response, H_{EL}^2, and an example of a raw spectrum (computed with the robust method described below) are shown in Figure B1. For our probe response, $H_{NIN}^2(k)$, we use the formulation of Ninnis (1984), a quartic fit to measurements valid for $k < 100$ cpm; we do not consider the probe's temporal response, as it is too slow to affect microscale measurements. Conversions to wavenumber and to spectral density per wavenumber
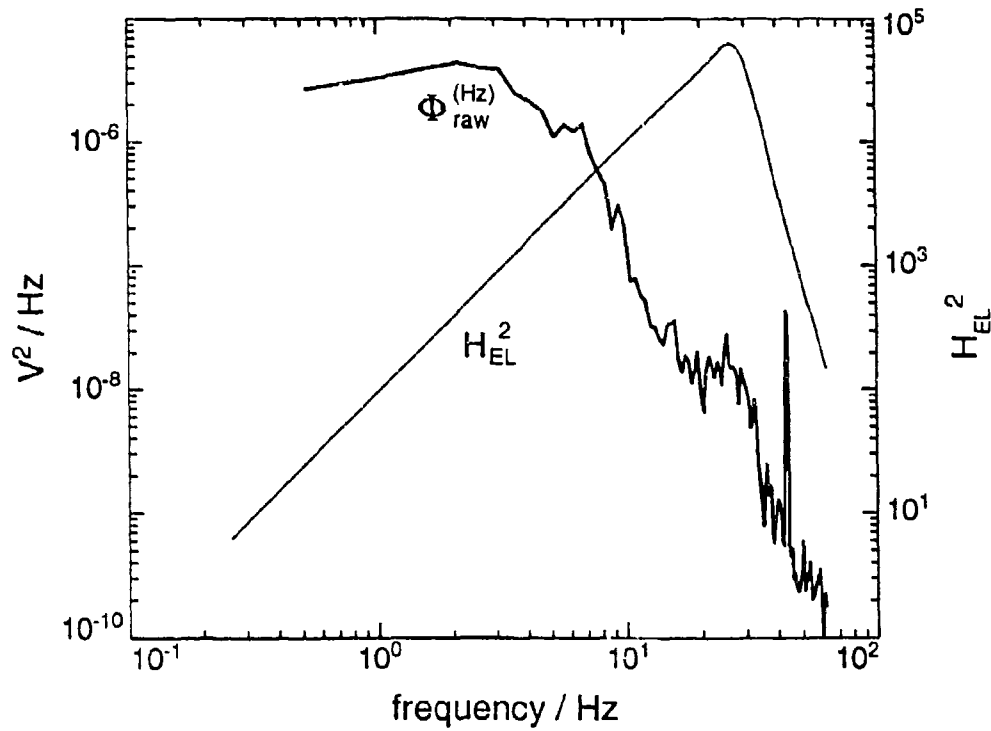
Figure B1. Drop 0267, raw voltage spectrum for airfoil probe # 1 computed with the robust method from 3.368–3.392 MPa ($W = 0.3241$ m s^{-1}). The combined transfer function of the electronics, H_{EL}^2, slopes upward to 25 Hz owing to the differentiating circuit and downward thereafter owing to the low-pass filter.

are $k = f/W$ and $\Phi_{vel}^{(cpm)}(k) = W\Phi_{vel}^{(Hz)}(f)$. The shear spectrum is computed as $\Phi_{sh}^{(cpm)}(k) = (2\pi k)^2 \Phi_{vel}^{(cpm)}(k)$. Altogether,

$$\Phi_{sh}^{(cpm)}(k) = \frac{W\ \Phi_{raw}^{(Hz)}(f)}{H_{SH}^2(k)} \qquad [\text{s}^{-2}\ \text{cpm}^{-1}]$$

where $H_{SH}^2(k) = (S/2\pi k)^2\ H_{EL}^2(f)\ H_{NIN}^2(k)$ and $f = kW$. Using this expression, the raw spectrum of Figure B1 is transformed to the shear spectrum of Figure B2. Also shown is the probe response, H_{NIN}^2, and the combined response, H_{SH}^2 (at this fall rate). The nearly constant value of H_{SH}^2 at $k < 20$ cpm indicates that the conditioned measurements represent shear rather than velocity. The approximate relationship is

$$E(t) = \frac{G_0(C_s/C_f)S_v W^2}{4\pi f_0 g}\frac{du}{dz}(t) \approx \frac{1}{|H_{SH}(f\approx f_0)|}\frac{du}{dz}(t) \qquad [\text{V}]$$
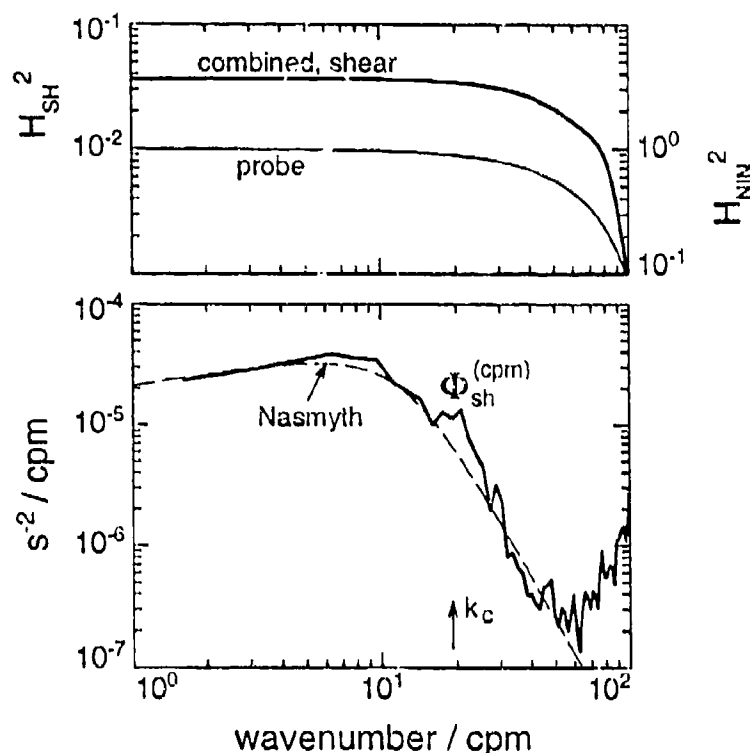
Figure B2. Drop 0267, airfoil vs Nasmyth shear spectrum. Bottom panel shows shear spectrum for airfoil probe # 1 for the robust window from 3.368–3.392 MPa. The integration cutoff wavenumber, $k_c = 19.4$ cpm, is indicated. Dashed line is the Nasmyth spectrum for $\epsilon = 4.25 \times 10^{-9}$ W kg^{-1} and $\nu = 1.22 \times 10^{-6}$ m^2 s^{-1}. Upper panel shows the Ninnis probe response, H_{NIN}^2 (light line), and the combined transfer function from shear to measured voltage, H_{SH}^2 (heavy line).

where $G_0 = 9.7$ is the circuit gain at $f_0 = 1$ Hz and $C_s/C_f \approx 1$ is the further, probe-dependent gain.

2. Spectral Processing

The periodogram processing generates dissipation rates on a 5-kPa (0.5-m) grid. Two values —one for each airfoil probe—are computed for each point. Each estimate is based on data from a window of $L = 5$ kPa centered about the grid point, yielding no overlap between windows. Since the raw data are sampled at 125 Hz, the number of points in a window varies with fall rate. After the data are demeaned, a Hanning window (full cosine taper) is applied. Zeroes are appended to the record until attaining a valid FFT size (an even integer factorable into 2, 3, and 5). The power

spectrum is formed from the transform of the data. After this raw frequency spectrum is corrected for the variance filtered out by the time-Hanning, it is converted to a wavenumber spectrum of shear.

The robust processing estimates dissipation rates on a 20-kPa (2-m) grid. It uses data windows of $L = 24.24$ kPa centered about each grid point. The slight overlapping of windows, combined with the spectral processing within them, evenly weights all airfoil data in the drop. Multiple spectra are computed within each window on segments of length $S \approx L/4 = 6.06$ kPa. The actual size, which varies with fall rate, is chosen such that the number of raw data points is a valid FFT size. The raw spectrum for each segment is formed using the same steps as in the periodogram processing (but without zero-padding). Segments are overlapped by approximately 70%, yielding 9 to 11 spectra per window (Figure B3). As spectral values at each frequency are combined to form the ensemble spectrum for the window, m-estimators are used to heavily downweight high outliers (Chave et al., 1987). This technique, implemented by W. R. Hess (personal communication, 1989), objectively and reproducibly rejects contamination from spikes caused by plankton impacts or electrical transients in MSP's circuitry. However, the algorithm fails when spiking occurs too often in a window. Also, if the amplitude of the true signal changes abruptly, the window's spectrum may be underestimated as the higher variance segments are mistakenly
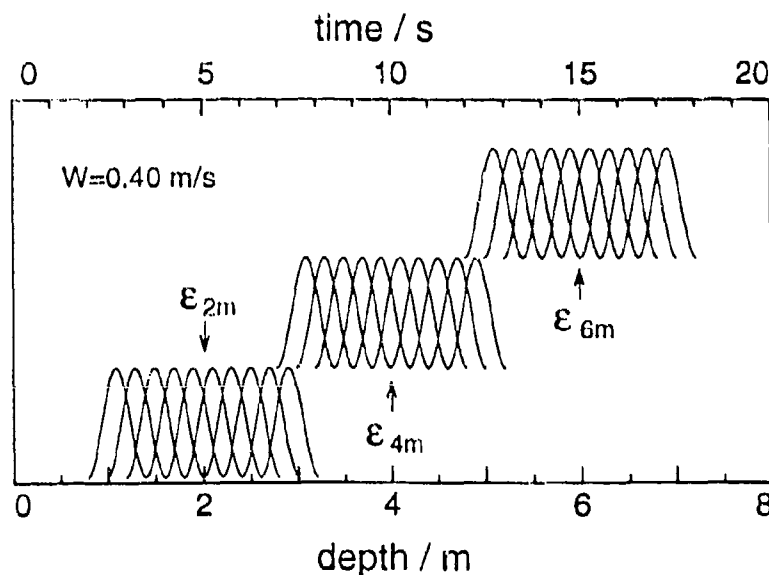
Figure B3. Windowing for robust processing of airfoil data, assuming $W = 0.40$ m s^{-1}. Windows are 2.424 m wide, centered at 2, 4, and 6 m. Each window consists of 10 segments, 0.606 m long and overlapped 70%. Shape of segments indicates weighting of Hanning windows.

downweighted. This effect is slight for the airfoil data, but it can be severe in robust processing of temperature gradient microstructure.

The two methods produce similar results for sections of clean data, judging from dissipation rates averaged over 0.1 MPa or more. We also find good agreement when comparing spectra ensemble averaged over several consecutive windows; larger windows are used in this case than in generating dissipation rates to provide a wider overlap with ACM results (such as in Figure 17). There is a tendency for robust dissipation rates or spectra to be slightly (up to 10%) lower than the periodogram results.

3. Dissipation Rates

For isotropic turbulence, $\epsilon = 7.5\nu\overline{(du_2/dz)^2}$, where ν is the kinematic viscosity and $u_2(z)$ are the horizontal cross-stream velocity fluctuations. We estimate the shear variance by integrating $\Phi_{\mathrm{sh}}^{(\mathrm{cpm})}(k)$ over an appropriate wavenumber band. The size of the segment chosen in computing the spectrum sets the lower limit, k_0 (as well as the wavenumber interval, $\Delta k = k_0$). Regarding the upper limit, k_u, it should be high enough so that most of the variance has been captured but not so high that noise significantly contaminates the integration. The spectral noise floor is probe-dependent and sometimes varies during a drop. However, the lower the dissipation (and corresponding spectral levels), the sooner the noise floor is reached, and the sooner the integration must be cut off. We use Oakey's analytic representation of the Nasmyth turbulent shear spectrum to guide our selection of k_u. This model spectrum has a constant shape, but shifts in wavenumber and amplitude with varying Kolmogorov wavenumber, $k_s = (\epsilon/\nu^3)^{1/4}$, and spectral level, $A_s = (\epsilon\nu^5)^{1/4}$.

Summing the data spectrum from k_0 up to 10 cpm generates an initial estimate, $\epsilon_{10\mathrm{cpm}}$, determined by finding the model spectrum that contains the same variance as the data over this limited band. The trial cutoff of $k_u = 0.088\,k_s$ (k_u in cycles per meter) corresponds to the wavenumber before which resides 90% of the variance in the model spectrum for $\epsilon_{10\mathrm{cpm}}$. If $k_u < 9$ cpm, it is set to 9 cpm (this occurs when $\epsilon \leq 2 \times 10^{-10}$ W kg^{-1}); if $k_u > 100$ cpm, it is set to 100 cpm, the upper limit of the probe's resolution (this occurs when $\epsilon \geq 10^{-5}$ W kg^{-1}). Summing the data spectrum from k_0 to k_u produces an improved estimate, ϵ_{est}. A new k_u is determined from ϵ_{est}, and the spectrum is again summed to yield the final value of ϵ. No attempt is made to compensate for unresolved variance (i.e., below 1 cpm or past 100 cpm), since dissipation rates encountered by MSP seldom exceed 10^{-5} W kg^{-1}. At each grid point, two estimates (one from each probe) are generated. If they are close (e.g., within a factor of 4), they are averaged together; otherwise, the lower value is chosen since noise and spiking lead to inflated estimates.

In Figure B4a we compare a range of data spectra with their corresponding Nasmyth spectra. Each data spectrum is formed by ensemble averaging 0.01-MPa periodogram spectra (50% overlapped) over intervals of 0.1 to 0.2 MPa, within which
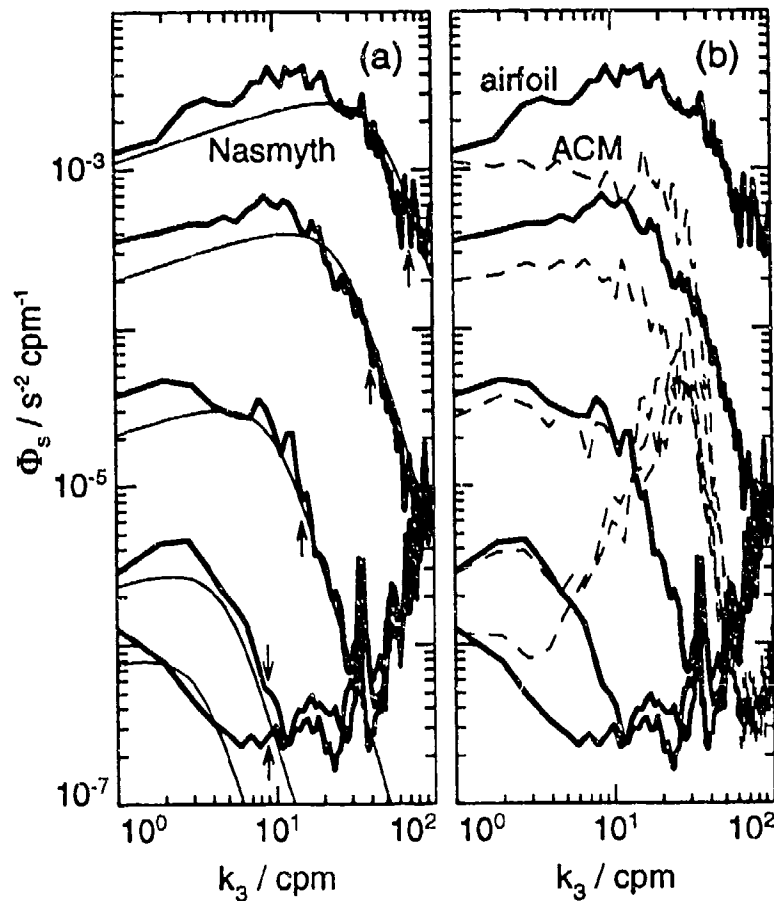
Figure B4. Comparison of ensemble-averaged airfoil spectra (heavy lines) with (a) corresponding Nasmyth spectra (light lines) and (b) corresponding single-axis ACM spectra (dashed lines). Drop numbers, pressure range, ε, and $\bar{T}$ for the spectra are, from bottom to top:

0346, 4.03–4.17 MPa, 3.2×10^{-11} W kg^{-1}, 10.3°C,

0387, 4.65–4.70 MPa, 1.6×10^{-10} W kg^{-1}, 8.8°C,

0348, 9.35–9.47 MPa, 4.2×10^{-9} W kg^{-1}, 4.7°C,

0356, 2.79–2.91 MPa, 1.2×10^{-7} W kg^{-1}, 11.9°C,

0267, 4.83–4.93 MPa, 1.6×10^{-6} W kg^{-1}, 7.8°C.

Arrows in (a) indicate average cutoff wavenumbers for ε integrations.

there is minimal variation of dissipation rates. Also, spectra from the two probes are averaged together, since they agreed well in all cases. The Nasmyth spectrum is formed using the mean of the 0.02-MPa robust dissipation estimates spanning the interval. All but the highest spectrum hit the noise floor by 100 cpm, with the lowest spectrum barely above the noise at $k < 5$ cpm. Integration of such low spectra (out to 9 cpm) establishes our dissipation noise level of 3 to 10×10^{-11} W kg^{-1}. At low dissipation rates, the variance of the inertial subrange is concentrated below 1 cpm, beyond the limit for the airfoil probes; oftentimes, there is no inertial subrange, with motions becoming anisotropic owing to buoyancy effects (e.g., for $\epsilon/\nu N^2 < 25$). As rates rise above 2×10^{-10} W kg^{-1}, turbulent shear spectra are increasingly well resolved. The measured and model spectra agree decently, with minor differences at low wavenumber and in the location of the viscous rolloff.

Combining uncertainties of fall rate, probe calibration, temperature sensitivity, and spectral processing and integration, we estimate that our measured dissipation rates are within a factor of 2 the actual values. However, comparisons with the ACM suggest additional uncertainty of an unknown nature that might overwhelm the above-mentioned sources.

4. Airfoil Probes vs ACM

A unique feature of MSP is that it measures velocity microstructure with two separate devices. The ACM averages motions across 20-cm paths, positioned 2 cm ahead of the point-like measurements of the airfoil probes. The alignment of the airfoils differs from that of one ACM axis by only 20-25°. We compare shear spectra from this axis, uncorrected for platform motion, with $\Phi_{sh}^{(\text{cpm})}$ from the airfoils. The spectra often agree well from 1 to 10 cpm (or to where the ACM becomes noisy); coherence of the data can be even more broadbanded, from 0.1 to 20 cpm (at most).

With such comparisons, we demonstrate the general success of the airfoil calibrations (when ACM and airfoil spectra coincide), diagnose contamination by elevated low-frequency noise, and note an apparent increase in airfoil sensitivity with temperature and dissipation rate. We infer contamination when the spectrum from the failing probe is well above that of the ACM at 1 cpm and steadily falls to join it at some greater wavenumber (while the other probe tracks the ACM throughout); in more turbulent sections of the drop, the spectral mismatch disappears as the real signal exceeds the low-frequency noise. In contrast, variations in sensitivity are suggested when the airfoil probes mutually agree but change from nearly matching to greatly exceeding the ACM as conditions vary during a drop. Most often, the ACM spectrum runs nearly parallel to the higher airfoil spectrum, but sometimes their separation increases with wavenumber (as if the ACM spectrum is attenuated).

In Figure B4b we plot airfoil spectra against their ACM counterparts. For the lowest pair, the ACM is barely above its noise floor. The next highest shows good

agreement from 1 to 4 cpm. Moving up, the next two are well matched in shape, but the airfoil spectra are higher by factors of 1.3 and 2, respectively. The highest spectra differ in shape, diverging toward higher wavenumbers; however, the ACM spectrum for the next deeper 10-m interval of this drop parallels, at a factor of 2.2 beneath, its airfoil spectrum (which is close in level to that displayed).

We characterize each comparison by summing both spectra from 2 to 7 cpm and then forming the airfoil-to-ACM ratio. For $\epsilon < 10^{-9}$ W kg^{-1}, we stop at 5 cpm to avoid ACM noise (and at 4 cpm for $\epsilon < 3 \times 10^{-10}$ W kg^{-1}). We summarize results from the COARE3 cruise in Figure B5, plotting ratios against temperature, T, and dissipation rate, ϵ. There is fair agreement at lower T and ϵ, with ratios varying from 0.5 to 2 and occasionally 3. Ratios are generally greater at the highest T and ϵ, often rising above 4 and to as much as 8. Correlations between ϵ, T, and N (or dT/dz) confound attempts to distinguish the source of the observed behavior. The ratio does rise with ϵ for $T \approx 29°$ and with T for $\epsilon \approx 3 \times 10^{-9}$ W kg^{-1}. Comparisons from other MSP cruises show patterns consistent with those of Figure B5.

Most of our published shear spectra are computed within the thermocline, where $T < 20°C$ and ϵ rarely exceeds 10^{-7} W kg^{-1}; thus, ensemble-averaged ACM and airfoil levels appear well matched between 1 and 3 cpm. It was not until we focused on the warm, turbulent waters atop the tropical Pacific thermocline that we noticed the spectral mismatches.

Variations in airfoil or ACM sensitivities can lead to some spectral separation. When an airfoil probe's sensitivity (or effective capacitance, C_s) is greater than supposed, use of the lower, supposed value will boost the computed shear spectrum. In contrast, if the ACM sensitivity is greater than supposed, the computed spectrum will be too low. Indeed, airfoil sensitivity can increase with temperature and turbulent velocity (Osborn and Crawford, 1980) and ACM sensitivity does go up with sound speed (and, therefore, with temperature for MSP's depth range). However, these effects account for, at most, a factor of 2 difference between airfoil and ACM spectra. Furthermore, the observed behavior lacks consistency; for instance, spectral ratios at a given temperature and dissipation rate can vary considerably from case to case (even in a single drop). Other possible contributors include temperature sensitivity in the circuits of the airfoils (probably weak) and the ACM (complex and difficult to quantify) and attenuation across the ACM path (difficult to characterize). One point in support of the contention that the airfoil is responsible: when their spectral levels are reduced to agree with those of the ACM (in Figure B4 for instance), the lowered airfoil spectra and Nasmyth spectra, recomputed using the correspondingly lower dissipation rates, tend to exhibit a better match than the originals, particularly in the high wavenumber rolloff. If the airfoils are the cause, we are still uncertain whether the behavior is confined to MSP probes and circuits, to all probes of our design and manufacture, or to all piezoelectric airfoil probes.
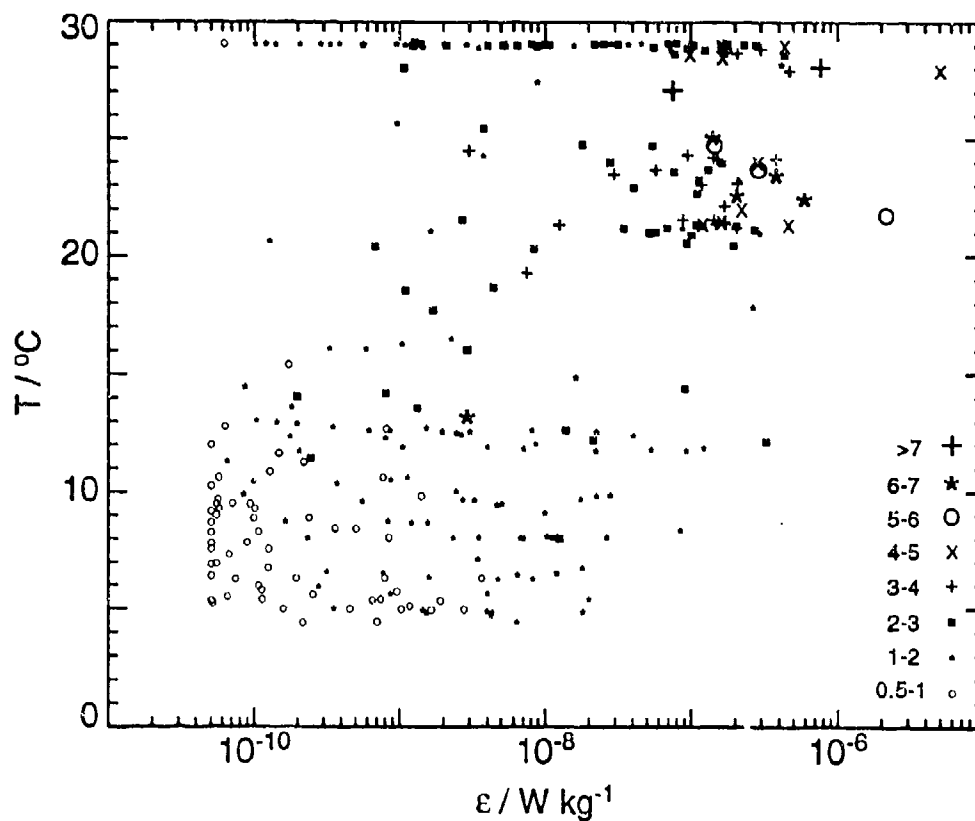
Figure B5. Ratios of airfoil-to-ACM shear variance from COARE3 drops. Shear spectra, formed for 0.1 to 0.3 MPa intervals, are integrated from 2 to 7 cpm to compare variance (to avoid ACM noise, integrations end at 4 or 5 cpm for low-level spectra). Ratios are indicated by symbols, which are plotted against the average ϵ and T for each case. The intervals chosen for comparison include most of the high dissipation occurrences ($\epsilon > 10^{-8}$ W kg^{-1}) but only a representative sampling of lower dissipation cases. The isolated high ratio at (3×10^{-9} W kg^{-1} and 13°C) is due to spiky data in both airfoil channels.

Appendix C: VEHICLE DYNAMICS

1. Horizontal Dynamics

We restrict the horizontal dynamics by assuming MSP remains upright at all times. Therefore, $\theta(t) = d\theta(t)/dt \equiv 0$, and all points on the vehicle move at $\mathbf{v}_{\text{msp}}(t)$, the velocity of P from (3). The dynamics are like those of a point mass, since the vehicle must accelerate uniformly regardless of where it is forced. The water trapped under the skin moves along with the solid structure, so we include it in the definition of M, the total vehicle mass. We examine the forces acting on MSP when the ACM is at reference depth $z = z(t)$, as defined by (6). At some distance $s > 0$ above the ACM, the water encounters MSP with a (free-stream) relative velocity $\mathbf{v}_{\text{wat}}(z - s) - \mathbf{v}_{\text{msp}}(t)$, the difference between (1) and (3). While the transverse (horizontal) component

$$v_{\text{wat}}(z - s) - v_{\text{msp}}(t)$$

can vary along the body (Figure 9), we prohibit variation of the axial (vertical) component

$$W_{\text{wat}}(z - s) - W_{\text{msp}}(t)$$

by assuming that W_{wat} is constant over MSP's length.

The horizontal pressure forces employed by the model are based on potential flow theory. We summarize this result, following Hayes et al. (1984). Consider a long, slender solid body of revolution about some s axis, fixed in place and pointed into a uniform, inviscid flow with axial and transverse components w and v, respectively (Figure C1). For a small angle of attack $\alpha = \tan^{-1}(v/w)$, the body experiences a force, $f(s)$, per unit length in the transverse direction of magnitude.

$$f(s) = q_0 \frac{dA}{ds} \sin 2\alpha = \rho v w \frac{dA}{ds} \qquad [\text{N m}^{-1}] , \qquad (\text{C1})$$

where $q_0 = \rho(v^2 + w^2)/2$ is the free-stream dynamic pressure, ρ is the fluid density, and $A(s) = \pi(r(s))^2$ is the cross-sectional area of the body (Allen and Perkins, 1952).

To apply (C1) to MSP, we fix the origin of the s-axis at $z = z(t)$ with $s > 0$ upwards (Figure 9), and sum $f(s)$ up along the instrument. Since $f(s) = 0$ where $dA/ds = dr/ds = 0$, the constant-diameter main tube should feel no linear pressure force. Integration of (C1) from the ACM ($r = 0$, $s = 0$) up onto the front of the main tube ($r = r_N$, $s \approx 1$ m, $dr/ds = 0$) yields the nose force, F_N; integration from the back of the main tube ($r = r_N$, $s \approx 3$ m) up to the maximal radius at the brushes ($r = r_T$, $s \approx 3.7$ m) yields the tail force, F_T. While we do not expect a uniform flow in either region, we do assume that the effective horizontal flow felt near the nose or tail can be represented by a single relative velocity, V_N or V_T. Specifically, V_N is some suitable average of the horizontal relative velocities $v_{\text{wat}}(z - s) - v_{\text{msp}}$ within
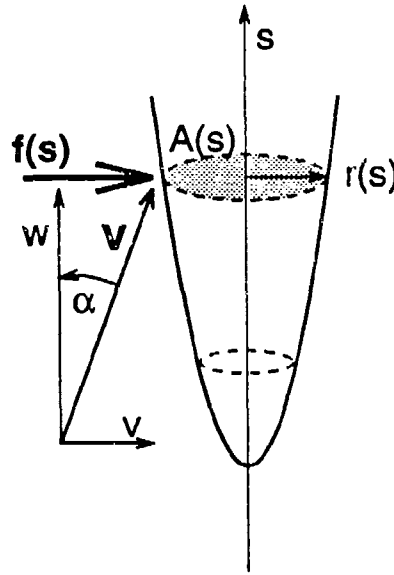
Figure C1. Pressure force per unit length on a slender body of revolution whose axis of symmetry is at angle α to an oncoming uniform flow, **v**. Cross-sectional area is $A(s) = \pi(r(s))^2$.

the integration bounds. For the oncoming axial flow, $|W_{\mathrm{rel}}| = W_{\mathrm{msp}} - W_{\mathrm{wat}} > 0$ has the proper sense. Integration of (C1), under our stated assumptions, yields the expressions in (11) for F_N and F_T. In the subsection on model formulation, we explain how V_N and V_T are evaluated.

Including the added mass effect, as described in the main text, the balance of horizontal forces is

$$M \frac{dv_{\mathrm{msp}}}{dt} = F_N + F_T - \rho \Gamma_e \frac{dv_{\mathrm{msp}}}{dt} \; ,$$

which simplifies to (12) for acceleration. Not included in this balance is the transverse quadratic drag

$$F_{Dx} = \frac{1}{2} \rho \, C_{Dx} A_x v^2 \; , \tag{C2}$$

where C_{Dx} is the drag coefficient, v is the relative horizontal velocity, and A_x is the body's area normal to v. In most instances, drag force on MSP is negligible compared to F_N and F_T, and so we exclude it from the model. However, drag on the main tube may be significant when encountering high shear.

2. Vertical Dynamics

Although computation of vertical forces is not part of the model, it is useful to express the associated dynamics. With M_s and Γ_s as the mass and volume of the solid structure,

$$M \frac{d}{dt}|W_{\mathrm{rel}}| = F_G - F_B - F_{Dz}$$

$$= g M_s - g \rho V_s - \frac{1}{2}\rho C_{Dz} A_z W_{\mathrm{rel}}^2 \qquad (C3)$$

$$\underbrace{\hphantom{g M_s}}_{\text{gravity}} \underbrace{\hphantom{g \rho V_s}}_{\text{buoyancy}} \underbrace{\hphantom{\frac{1}{2}\rho C_{Dz} A_z W_{\mathrm{rel}}^2}}_{\text{drag}}$$

where $C_{Dz} \approx 1$ is the vertical drag coefficient, and $A_z = \pi r_T^2$ is the frontal area. Even when drag balances net buoyancy, $F_G - F_B$, to keep $|W_{\mathrm{rel}}| = W_{\mathrm{msp}} - W_{\mathrm{wat}}$ constant, MSP's absolute fall rate, W_{msp}, will vary as the water motion, W_{wat}, fluctuates with depth.

3. Tilt Dynamics

We assume MSP acts like a forced, damped pendulum so that

$$I_E \frac{d^2\theta}{dt^2} + R_E \frac{d\theta}{dt} + K_E \theta = L_N F_N - L_T F_T \qquad [\text{N m}] , \qquad (C4)$$

where L_N and L_T are, respectively, the distance between F_N and P and F_T and P. Coefficients I_E, R_E, and K_E, as described and roughly estimated in Table 2, are "effective" in that they include the following contributions arising from interactions between the falling MSP and the surrounding water: I_E includes added-mass effects as well as the mass distribution of the vehicle and trapped water; R_E includes damping from oscillation-induced pressure forces at the tail; K_E includes righting from vertical drag at the tail (F_{Dz}) as well as the separation of F_G and F_B. The forcing terms are of opposite sign since $F_N > 0$ gives an anticlockwise acceleration while $F_T > 0$ gives a clockwise push.

We simplify (C4) by dividing through by I_E and by referring to (11) for F_N and F_T, yielding

$$\frac{d^2\theta}{dt^2} + \beta_1 \frac{d\theta}{dt} + \beta_0 \theta = Q_N V_N - Q_T V_T \qquad [\text{rad s}^{-2}] , \qquad (C5)$$

where $\beta_1 = R_E/I_E$, $\beta_0 = K_E/I_E$,

$$Q_N = \frac{L_N}{I_E}\pi r_N^2 \rho \,|W_{\mathrm{rel}}| \quad \text{and} \quad Q_T = \frac{L_T}{I_E}\pi(r_T^2 - r_N^2)\rho \,|W_{\mathrm{rel}}| \qquad [\text{m}^{-1}\,\text{s}^{-1}] \quad (C6)$$

and with V_N and V_T as specified in (17). We do not explicitly use (C5) in generating velocity profiles. Rather, it enters into the transfer functions, derived in Appendix E, with which we analyze effects of tilt dynamics on the ACM and accelerometer measurements. While (C5) competently models some aspects of the observed behavior, it is an inadequate substitute for the tilt as inferred in (13) from the accelerometer data.

Appendix D: MODEL NUMERICAL INTEGRATION

With $v_{\mathrm{msp}}(z)$ constant over the integral bounds in (17), we can express (15) as

$$\frac{dv_{\mathrm{msp}}}{dz} + (H_N + H_T)\,v_{\mathrm{msp}}(z) = \frac{H_N}{D_N}\int_{Z_N-0.5D_N}^{Z_N+0.5D_N} v_{\mathrm{wat}}(z-s)\,ds \qquad (D1)$$
$$+ \frac{H_T}{D_T}\int_{Z_T-0.5D_T}^{Z_T+0.5D_T} v_{\mathrm{wat}}(z-s)\,ds.$$

The desired results are profiles of v_{msp} and v_{wat} at evenly spaced depths $z_j = z_0 + j\Delta z$. We define a function U_j that satisfies

$$\frac{dU_j}{dz} + (H_N + H_T)\,U_j = B_j \qquad (D2)$$

in the interval $[z_{j-1}, z_j]$, where

$$B_j = \frac{H_N}{D_N}\,[\,I(z_{j-1/2} - (Z_N + 0.5D_N)) - I(z_{j-1/2} - (Z_N - 0.5D_N))\,]$$
$$+ \frac{H_T}{D_T}\,[\,I(z_{j-1/2} - (Z_T + 0.5D_T)) - I(z_{j-1/2} - (Z_T - 0.5D_T))\,]$$

is the right-hand side of (D1) evaluated at the interval midpoint $z = z_{j-1/2} = z_j - \frac{\Delta z}{2}$ using integrals

$$I(Z) \equiv \int_{z_0}^{Z} v_{\mathrm{wat}}(s)\,ds$$

linearly interpolated from the running sums

$$S(z_n) \equiv \sum_{i=1}^{i=n} \frac{v_{\mathrm{wat}}(z_i) + v_{\mathrm{wat}}(z_{i-1})}{2}\,\Delta z.$$

(Note that $I(Z < z_0) = 0$ and that $S(z_0) = 0$.) With the initial condition $U_j(z_{j-1}) = v_{\mathrm{msp}}(z_{j-1})$, this differential equation for U_j approximates (D1) for v_{msp} over the interval, and thus $v_{\mathrm{msp}}(z_j) \approx U_j(z_j)$. The solution of (D2),

$$U_j(z) = \left[v_{\mathrm{msp}}(z_{j-1}) - \frac{B_j}{H_N + H_T}\right]\exp[-(H_N + H_T)(z - z_{j-1})] + \frac{B_j}{H_N + H_T},$$

is evaluated for $z = z_j$ to update the vehicle velocity, $v_{\mathrm{msp}}(z_j) = U_j(z_j)$. Finally, as in (18), we set $v_{\mathrm{wat}}(z_j) = v_{\mathrm{msp}}(z_j) + v_{\mathrm{rel}}(z_j)$.

Appendix E: TRANSFER FUNCTIONS AND VEHICLE TILT

In the first section of this appendix, transfer functions are derived for the horizontal (point-mass) and tilt motion of MSP as it responds to oceanic shear. They are used in the main text to find values for the point-mass parameters and later in this appendix to find values for the tilt response parameters. While not entirely realistic, the modeled tilt adequately demonstrates the dominance of forcing on the response and the appropriateness of inferring tilt from the accelerometer data. The effects of tilt position and oscillation on the ACM measurements are evaluated, with the conclusion that uncertainties in the computed tilt or in the correction parameters B_f and L_v have little effect on the resulting ocean shear spectra.

1. Response Functions

We generated several of the parameters listed in Table 6 while discussing vehicle dynamics, interpreting the measurements, and specifying the vehicle response model. Their various effects are examined most easily through the analytic expressions of the vehicle response functions in wavenumber space.

We define the Fourier transform for water velocity as

$$\hat{v}_{\text{wat}}(k) \equiv \int_{-\infty}^{\infty} v_{\text{wat}}(z)\, e^{-ikz} dz$$

with radian wavenumber k and with z positive downward. As indicated in Table 5, transfer functions A, B, C_r, C_m, and D predict how MSP and its measurements respond to the ocean velocity field.

First we derive $A(k)$, the response function for vehicle velocity. Starting with the Fourier transform of (D1),

$$(ik + H_N + H_T)\, \hat{v}_{\text{msp}}(k) = \frac{H_N}{D_N} \int_{Z_N - 0.5D_N}^{Z_N + 0.5D_N} e^{-iks}\, \hat{v}_{\text{wat}}(k)\, ds$$
$$+ \frac{H_T}{D_T} \int_{Z_T - 0.5D_T}^{Z_T + 0.5D_T} e^{-iks}\, \hat{v}_{\text{wat}}(k)\, ds \,,$$

we divide through by $\hat{v}_{\text{wat}}(k)$, evaluate the integrals, and simplify using Euler's identity, $\sin x = (e^{ix} - e^{-ix})/2i$, to form

$$A(k) = \frac{H_N\, e^{-ikZ_N}}{H_N + H_T + ik} \operatorname{sinc}(kD_N/2) + \frac{H_T\, e^{-ikZ_T}}{H_N + H_T + ik} \operatorname{sinc}(kD_T/2) \,, \qquad (\text{E1})$$

where $\operatorname{sinc} x \equiv x^{-1} \sin x$.

We proceed in a similar fashion to derive $B(k)$, the response function for vehicle tilt. We assume a constant fall rate, W_0, so that $d\theta/dt = W_0\, d\theta/dz$, and simplify the transform of (C5) to produce

$$B(k) = \frac{Q_N\, e^{-ikZ_N}\, \text{sinc}\,(kD_N/2) - Q_T\, e^{-ikZ_T}\, \text{sinc}\,(kD_T/2) - (Q_N - Q_T)\, A(k)}{\beta_0 + ik\, W_0\beta_1 - k^2 W_0^2} . \quad \text{(E2)}$$

We generate the remaining transfer functions

$$
\begin{aligned}
C_r(k) &= 1 - A(k) \\
C_m(k) &= C_r(k) + W_0(B_f - ikL_v)\, B(k) \\
D(k) &= ikW_0\, A(k) + (y - L_a k^2 W_0^2 - ikW_0^2)\, B(k)
\end{aligned}
\quad \text{(E3)}
$$

by dividing $\hat{v}_{wat}$ into the Fourier transforms of (7), (14), and (10), for which we assume $W_0 \gg |v_{msp}\theta|$. Expansion of $A(k)$ in (E3) leads to (19), with which we tune the point-mass response model.

2. Tuning the Tilt Response

To complete our model of the tilt response, we must select values for parameters β_1, β_0, Q_N, and Q_T. We begin by assuming the optimal values, given in Table 6, for the six force parameters in $A(k)$. We could tune $B(k)$ directly by comparing (E2) with cross spectra computed from profiles of θ and v_{wat}. Instead, we prefer to work with the transfer function from v_{acm} to a_{meas}, since these directly measured data, and their cross spectrum, are independent of model computations or assumptions. We define this transfer function as

$$H_m(k) \equiv \frac{\hat{a}_{meas}(k)}{\hat{v}_{acm}(k)} = \frac{D(k)}{C_m(k)} \quad \text{(E4)}$$

and note that, in the model, it includes parameters B_f, L_v, and L_a. We will also refer to the transfer function from relative velocity to measured acceleration,

$$H_r(k) \equiv \frac{\hat{a}_{meas}(k)}{\hat{v}_{rel}(k)} = \frac{D(k)}{C_r(k)}, \quad \text{(E5)}$$

as we examine the effects of tilt and oscillation corrections.

We generate trial versions of H_m by varying β_1, β_0, Q_N, and Q_T while keeping B_f, L_v, and L_a fixed at their nominal values in Table 6. Once we attain decent agreement with the measured cross spectrum, we can adjust B_f and L_v to improve the match. This tuning process yields the optimal parameter values listed in Table 6. In Figure E1, we compare the theoretical forms of H_m and H_r with the corresponding cross
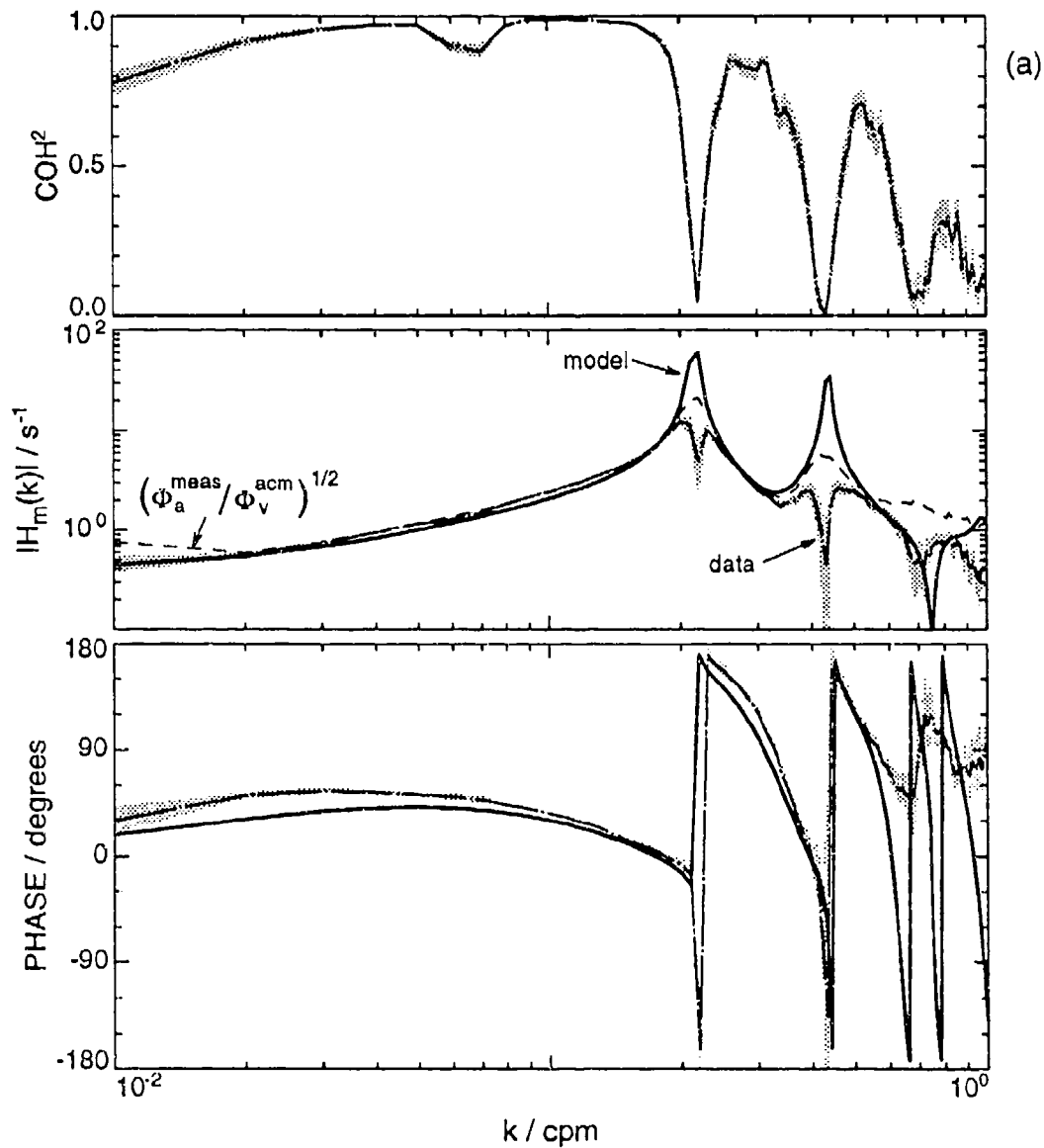
Figure E1. Comparison of model transfer functions H_m and H_r with corresponding cross spectra computed from PATCHEX data. Top panel is data coherence. Middle and bottom panels are amplitude and phase. Heavy lines denote the model and dash-dot lines denote the data (95% confidence limits are shaded). Dashed line in middle panel is the square root of the ratio of data autospectra, which differs in amplitude from the data transfer function where coherence is small. (a) H_m, ACM measured velocity to measured acceleration; (b) H_r, corrected relative velocity to measured acceleration.
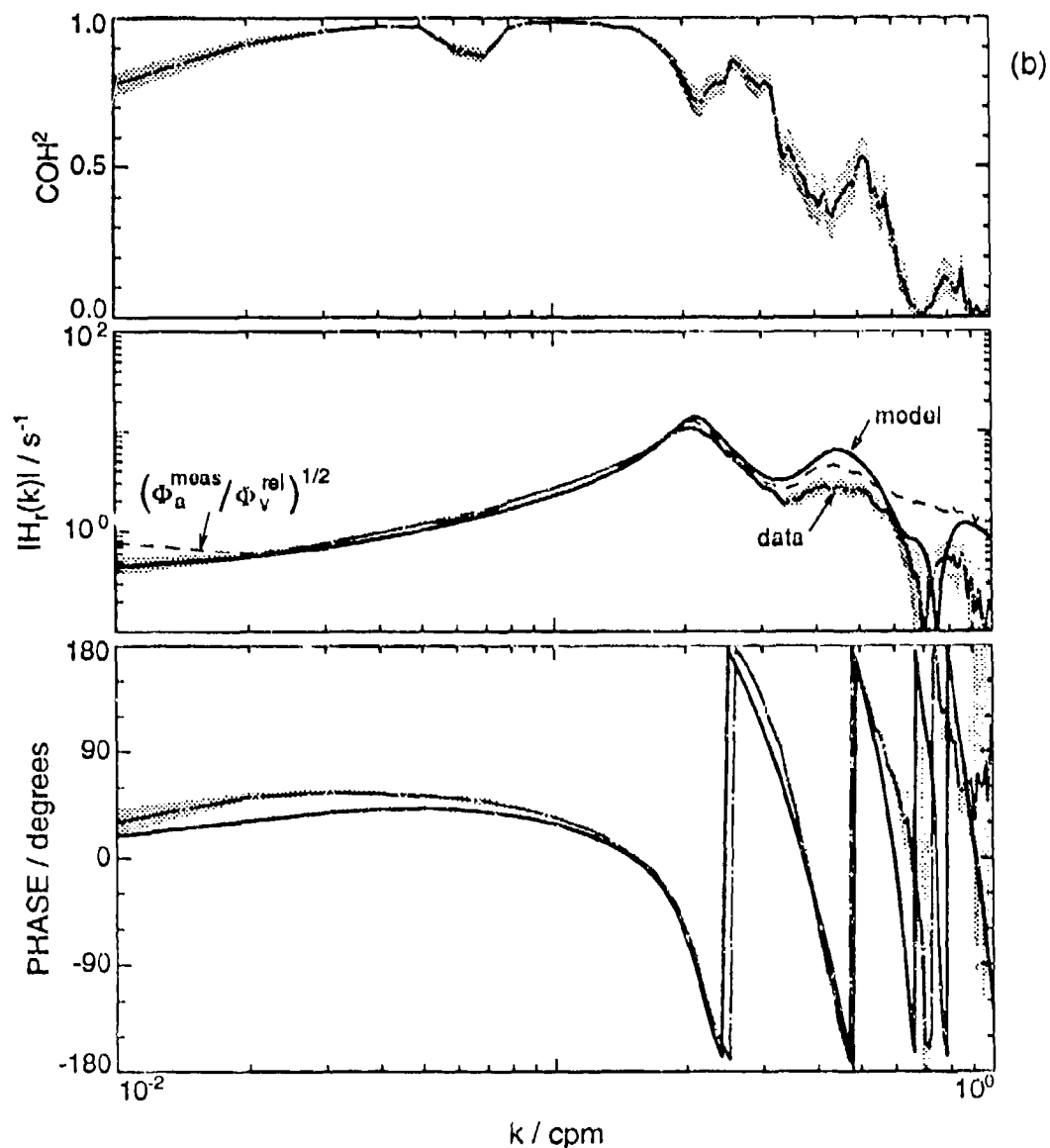
Figure E1, *cont.*

spectra derived from profiles (of the northward components) of the 28 PATCHEX drops. The top panels show the squared coherence of the data.

The match between the analytic and measured transfer functions is best for $k < 0.3$ cpm and degrades at higher wavenumbers. It is problematic to find a set of parameter values that match the data for both amplitude and phase, however. At 0.22 and 0.42 cpm, H_m exhibits large peaks in amplitude and wide swings in phase. These features correspond to the notches in Φ_a^{acm} and to bands of minimal coherence in

the data. Removal of tilt and oscillation from the measurements enhances coherence of relative velocity and acceleration (i.e., v_{rel} and a_{meas}) at the notch wavenumbers. Comparing H_m and H_r at $k > 0.5$ cpm, the phase—originally near 90°—is disrupted and coherence is diminished, consistent with removal of oscillations from v_{acm}.

3. Point-Mass vs Tilt Response

The point-mass response predicted by (E1), shown in Figure E2, and that reflected by the cross spectrum of v_{msp} and v_{wat} profiles are identical to within the accuracy of the numerical method. The amplitude $|A(k)|$, which is essentially the factor γ discussed with Figure 4, diminishes only after 0.33 cpm, reflecting MSP's tendency to respond at scales of the vehicle and larger.
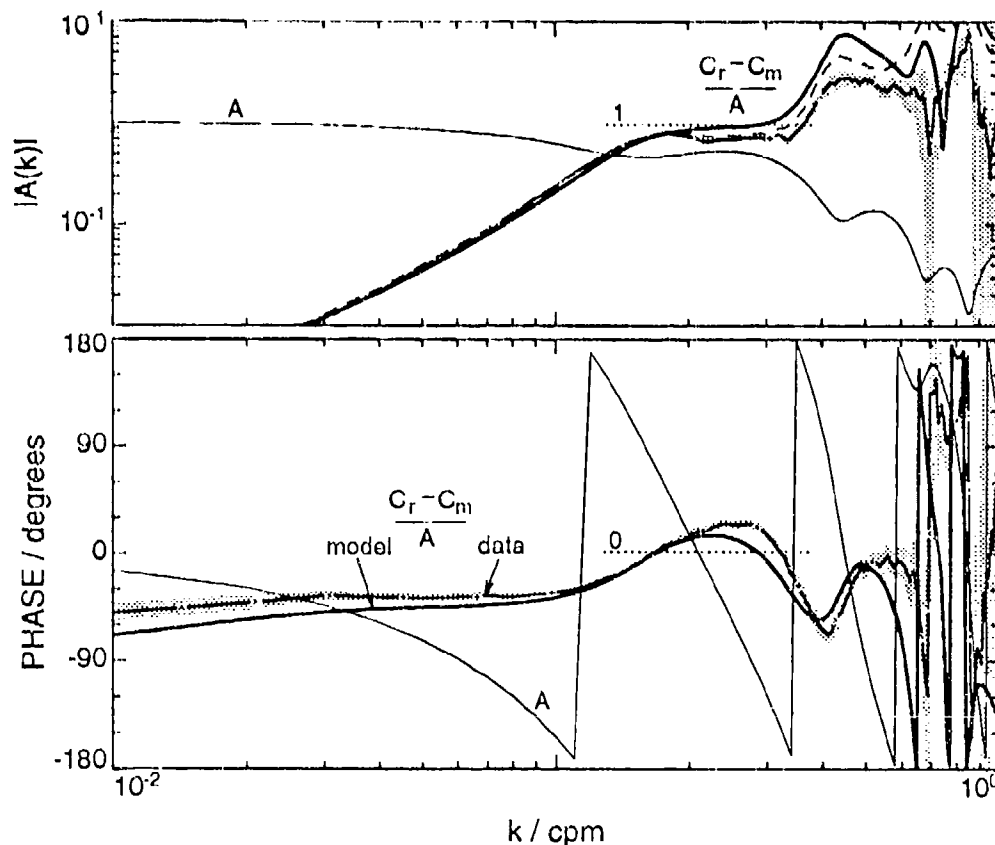
Figure E2. MSP platform response for large-tail configuration. Light line is the point-mass response, $A(k)$. The remaining curves compare the combined effects of tilt and oscillation, $-B_f W_{msp}\theta + L_v d\theta/dt$, to the point-mass motion, v_{msp}. Heavy lines denote the model, $[C_r(k) - C_m(k)]/A(k)$, and dash-dot lines denote the cross spectrum of the PATCHEX data (with 95% confidence limits); dashed line is the square root of the ratio of data autospectra; the coherence is the same as for $H_r(k)$.

The modeled tilt response, $B(k)$, matches the data fairly well at $k < 0.2$ cpm (Figure E3); the coherence is the same as for $H_r(k)$. Weakening the tail force term, Q_T, to 0.1 m^{-1} s^{-1} significantly reduces $|B(k)|$, demonstrating the dominance of forcing on the tilt response (there is no such sensitivity to any other parameter). For the free response, approximated using $Q_N = Q_T = 0.01$ m^{-1} s^{-1}, $|B(k)|$ retains the shape of the weakened $Q_T = 0.1$ m^{-1} s^{-1} version, but is at a fifth its level. Past 0.2–0.3 cpm, the model is inadequate in reproducing the observed tilt response.

The motion and orientation of the vehicle account for the difference between the ACM measurements, v_{acm}, and the ocean velocity, v_{wat}. Our model infers one portion—the combination of tilt position and oscillation—from the accelerometer measurements and manufactures the other portion—the point-mass motion—based on the modeled horizontal dynamics. Their relative contributions are compared in
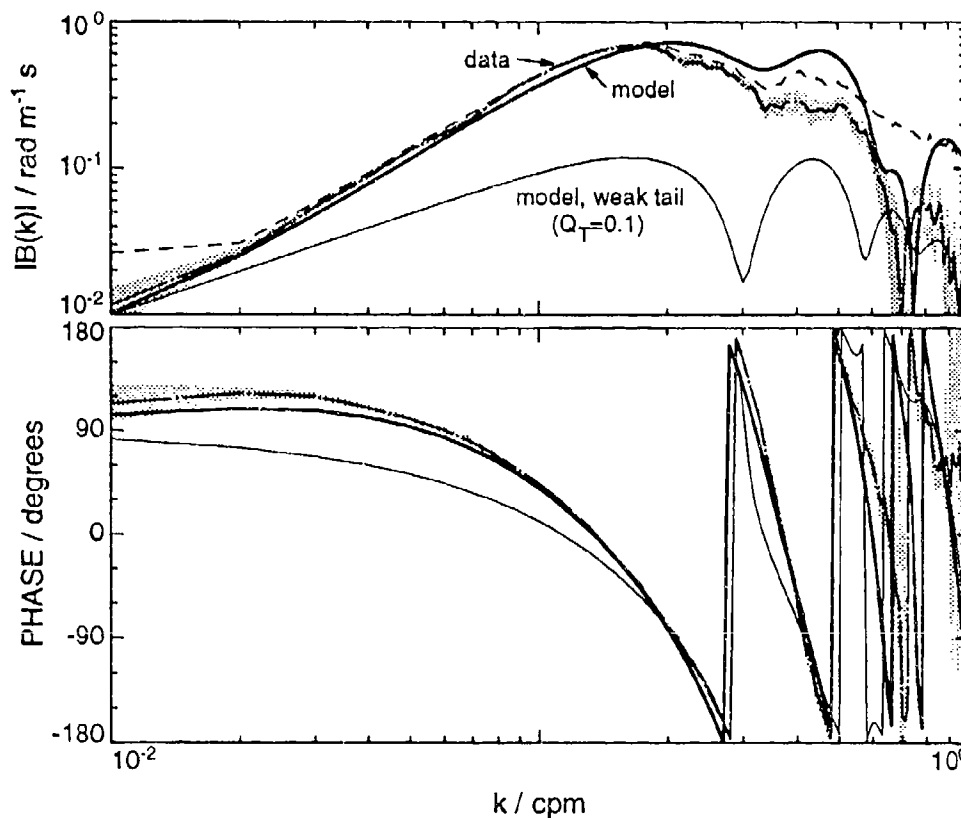

Figure E3 Comparison of model tilt response (heavy line) with that inferred from PATCHEX accelerometer measurements (dash-dot line); agreement is good out to 0.2 cpm and fair out to 0.3 cpm. Light line is $B(k)$ for weakened tail forcing, computed with $Q_T = 0.1$ m^{-1} s^{-1} and with remaining parameters at their optimal values.

Figure E2 using the transfer function $(C_r - C_m)/A$ from v_{msp} to $-B_f W_{\mathrm{msp}}\theta + L_v d\theta/dt$. Point-mass motion dominates tilt effects for $k < 0.1$ cpm. Between 0.16 and 0.33 cpm, they are closely matched both in amplitude and phase (within $\pm 30°$). Tilt oscillation rises at 0.4 cpm and becomes the dominant mode by 0.6 cpm. These observations have implications on the sensitivity of the results (v_{wat}) to the values of B_f and L_v: there is little effect from changes in B_f since they are felt mainly at $k < 0.15$ cpm; effects from L_v are fairly even at all $k > 0.1$ cpm, so the shape of the resulting ocean shear spectrum doesn't change significantly from minor alterations of this parameter.

## 4. Dominance of Tilt in Accelerometer Data

To check our assumption that we can reduce (10) to (13) by ignoring all but the tilt term in the accelerometer measurements, we form the ratio $D(k)/B(k)$ (Figure E4). For the data, our use of (13) implies a constant amplitude of 9.8 m s^{-2} and a phase of zero. The deviation of the modeled response at $k < 0.1$ cpm is due to the lateral acceleration, dv_{msp}/dt. This is of no concern because the ultimate results,
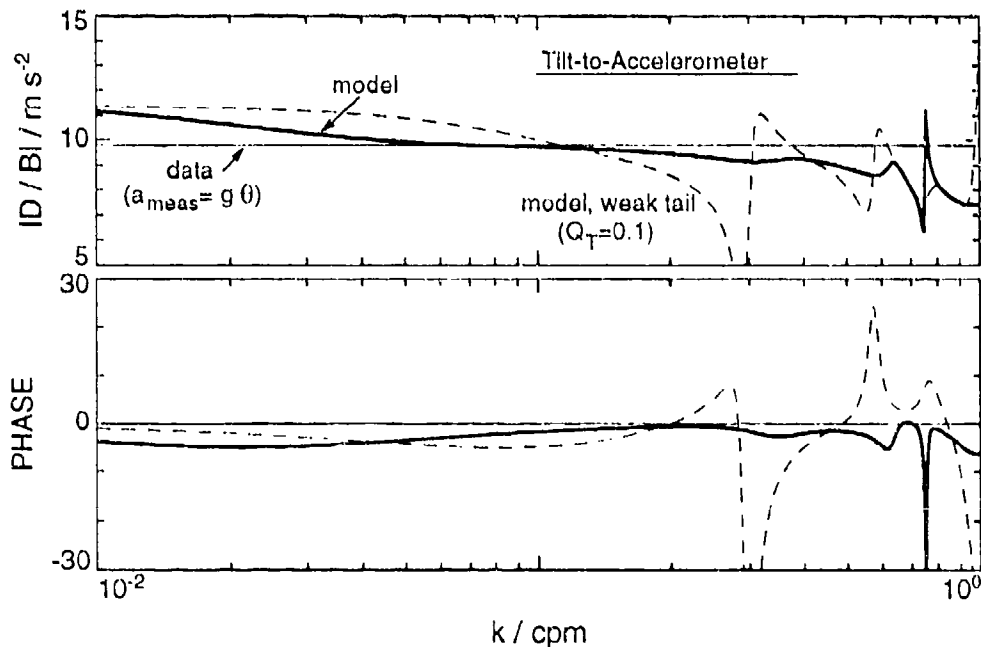
Figure E4. Transfer function from vehicle tilt to measured acceleration, i.e., $D(k)/B(k)$. Heavy line is model response for optimal large-tail parameters. Light line corresponds to the simplified $\theta = a_{\mathrm{meas}}/g$ used for the data and has a constant amplitude of 9.8 m s^{-2} and zero phase. Dashed line shows response with tail forcing weakened by setting $Q_T = 0.1$ m^{-1} s^{-1}.

oceanic velocities or shear spectra, are insensitive to tilt effects at large scales. The fluctuations past 0.6 cpm are artifacts of the modeled point-mass response (for v_{msp}), which is unreliable and dominated by tilt oscillation in this band. The downward trend at $k > 0.1$ cpm comes from the centripetal term, $L_a \, d^2\theta/dt^2$, which implies that we may be slightly underestimating θ at small scales. Without the strong tail force, the relation between tilt and measured acceleration becomes more complicated, as illustrated by the dashed line computed with $Q_T = 0.1 \ \mathrm{m^{-1} \, s^{-1}}$.

The magnetometer detects vehicle tilt but, unlike the accelerometers, is insensitive to the dynamics of vehicle motion. Tilt angles computed with (A1) from the magnetometer data are consistent with those computed with (13) from the accelerometer data. They are almost perfectly coherent and in phase up to 0.5 cpm, where the magnetometer data begin to get noisy (Figure E5). This close agreement, coupled with the results of the model analysis, supports our use of (13) for determining tilt angles.
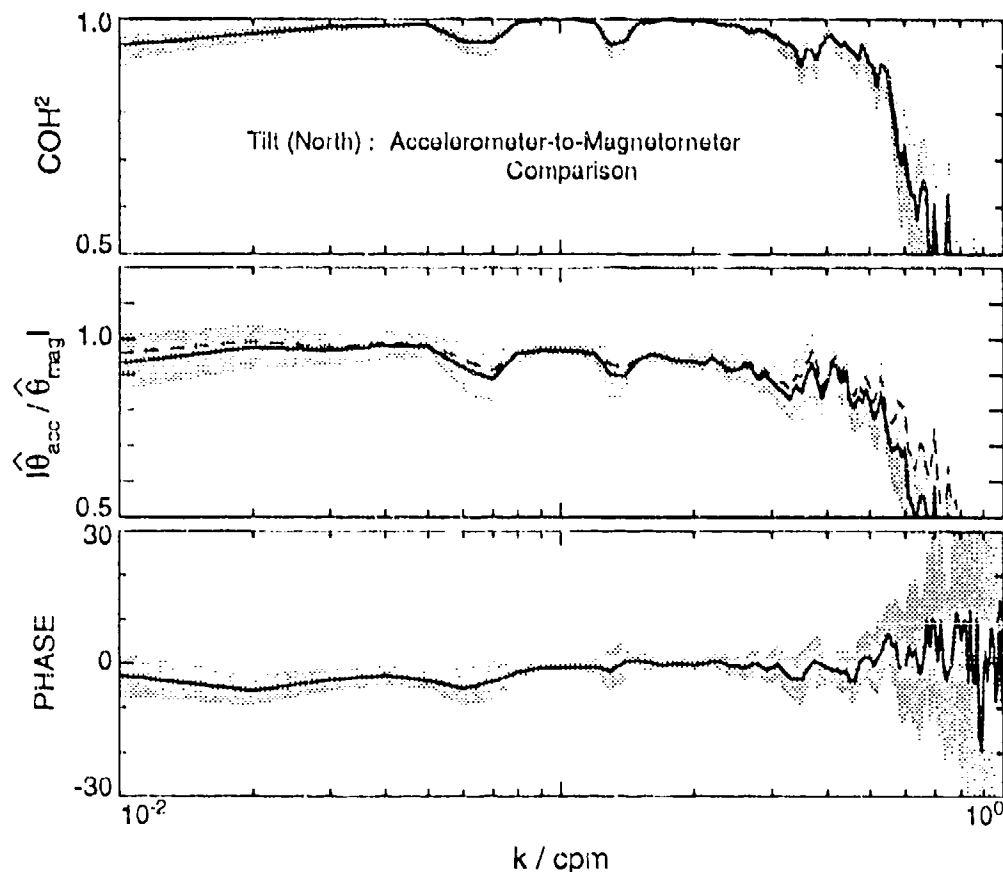
Figure E5. Comparison of northward tilt computed from accelerometer data with that computed from magnetometer data for five PATCHEX drops.

5. Summary

Expressions for model transfer functions are useful for understanding the behavior of the existing instrument or for planning modifications or new construction. We were able to find parameters to model MSP's tilt response. Although the model reproduces the observed tilt only at larger scales, it is useful for judging the sensitivity of the response at other scales as well. We fine tuned B_f and L_v with the transfer function H_m from accelerometer to ACM measurements. We showed that tilt effects are important in interpreting ACM data only at scales less than 10 m and that the final results are weakly sensitive to minor variations in B_f and L_v. We demonstrated the success of computing tilt directly from accelerometer data, especially for those scales where the ACM measurements are affected. This simplified approach is possible for MSP largely because free oscillation is damped or dominated by the forced tilt response.

REPORT DOCUMENTATION PAGE

Public reporting burden for this collection of information is estimated to average 1 hour per response, including the time for reviewing instructions, searching existing data sources, gathering and maintaining the data needed, and reviewing the collection of information. Send comments regarding this burden estimate or any other aspect of this collection of information, including suggestions for reducing this burden, to Washington Headquarters Services, Directorate for Information Operations and Reports, 1215 Jefferson Davis Highway, Suite 1204, Arlington, VA 22202-4302, and to the Office of Information and Regulatory Affairs, Office of Management and Budget, Washington, DC 20503.

1. AGENCY USE ONLY (Leave blank)	2. REPORT DATE	3. REPORT TYPE AND DATES COVERED
	October 1994	Technical

4. TITLE AND SUBTITLE

Resolving Velocity Profiles with the Multi-Scale Profiler

5. FUNDING NUMBERS

N00014-90-J-1188
N00014-90-J-1108
N00014-94-I-0079
N00014-86-K-0690

6. AUTHOR(S)

D.P. Winkel, M.C. Gregg, B.M. Bell, and T.B. Sanford

7. PERFORMING ORGANIZATION NAME(S) AND ADDRESS(ES)

Applied Physics Laboratory
University of Washington
1013 NE 40th Street
Seattle, WA 98105-6698

8. PERFORMING ORGANIZATION REPORT NUMBER

APL–UW TR 9414

9. SPONSORING / MONITORING AGENCY NAME(S) AND ADDRESS(ES)

Office of Naval Research
Department of the Navy
Ballston Center Tower #1
800 N. Quincy Street
Arlington, VA 22217-5000

10. SPONSORING / MONITORING AGENCY REPORT NUMBER

11. SUPPLEMENTARY NOTES

12a. DISTRIBUTION / AVAILABILITY STATEMENT

Distribution unlimited

12b. DISTRIBUTION CODE

13. ABSTRACT (Maximum 200 words)

The Multi-Scale Profiler (MSP), a freely falling dropsonde, has been used over the last 12 years to resolve oceanic shear variance at vertical scales from a few hundred meters down to nearly a centimeter. Because MSP yielded the first complete oceanic shear spectra, it is important to document the methods by which they were produced. Large scales are measured by an electromagnetic current meter (ECM), microscales by airfoil probes, and intermediate scales by an acoustic current meter (ACM). The ACM detects velocity relative to the instrument, so the platform motion must be known to determine the water velocity. Primarily, the ACM measurements are affected by tilt oscillations and by the gross (point-mass) motion of the vehicle; the former is inferred from accelerometer data, and the latter is constructed from a model of the vehicle's response to oceanic shear. Horizontal forcing on the array of drag brushes and turning blades at the tail complicates the response by causing MSP to react strongly to fluctuations on scales near the instrument's length of 4.3 m. We examine the effects of this response on spectra of the ACM measurements, noting particularly a deep notch near 0.2 cpm (cycles per meter). To account for such spectral features, the model of Hayes et al. for the TOPS was modified so that it correctly parameterized our large tail force. We discuss the dynamics, data processing, and model formulation relevant to production of oceanic velocity profiles from the ACM data, and present analytic transfer functions—derived from Fourier transforms of the model equations—which guide selection of optimal values for the model parameters. Velocity profiles and shear spectra resulting from the motion-corrected ACM data compare well with ECM results at large scales. Owing to MSP's high sampling frequencies, the ACM data provide a direct check on the veracity of the airfoil probe data at scales of 0.1—1 m. The overall strength of our results, as well as the weaknesses and uncertainties, is summarized.

14. SUBJECT TERMS

Free-fall profiler, velocity profiler, dropsonde, modeling platform motion, shear spectra, acoustic current meter, airfoil probes

15. NUMBER OF PAGES

80

16. PRICE CODE

17. SECURITY CLASSIFICATION OF REPORT	18. SECURITY CLASSIFICATION OF THIS PAGE	19. SECURITY CLASSIFICATION OF ABSTRACT	20. LIMITATION OF ABSTRACT
Unclassified	Unclassified	Unclassified	SAR